의학박사 학위논문

Studies on Treatment of Disease Phenotypes of Vision-Threatening Ocular Disease Mouse Models via Intraocular Drugs Delivery

안구내 약물 전달을 통한 시력을 위협하는 안질환 생쥐 모델의 질환 표현형 치료 연구

2023년 2월

서울대학교 대학원

의과학과 의과학전공

이 석 재

A thesis of the Degree of Doctor of Philosophy

안구내 약물 전달을 통한 시력을 위협하는 안질환 생쥐 모델의 질환 표현형 치료 연구

Studies on Treatment of Disease Phenotypes of Vision-Threatening Ocular Disease Mouse Models via Intraocular Drugs Delivery

February 2023

The Department of Biomedical Sciences,

Seoul National University

College of Medicine

Seok Jae Lee

Studies on Treatment of Disease Phenotypes of Vision-Threatening Ocular Disease Mouse Models via Intraocular Drugs Delivery

안구내 약물 전달을 통한
시력을 위협하는 안질환 생쥐 모델의
질환 표현형 치료 연구

지도교수 김 정 훈

이 논문을 의학박사 학위논문으로 제출함

2022 년 10 월

서울대학교 대학원
의과학과 의과학전공
이 석 재

이석재의 의학박사 학위논문을 인준함

2023 년 1 월

위 원 장	정 준 호	(인)
부위원장	김 정 훈	(인)
위 원	조 정 현	(인)
위 원	정 재 호	(인)
위 원	박 규 상	(인)

Studies on Treatment of Disease Phenotypes of Vision-Threatening Ocular Disease Mouse Models via Intraocular Drugs Delivery

by

Seok Jae Lee

A thesis submitted to the Department of Biomedical Sciences in partial fulfillment of the requirements for the Degree of Doctor of Philosophy in Medical Science at Seoul National University College of Medicine

February 2023

Approved by Thesis Committee:

Professor	Junho Chung	Chairman
Professor	Jeong Hun Kim	Vice chairman
Professor	Chung Hyun Cho	
Professor	Jae Ho Jung	
Professor	Kyu Sang Park	

ABSTRACT

Introduction: Aberrant growth of blood vessels, neovascularization is a key feature of vision-threatening eye diseases, including retinopathy of prematurity, diabetic retinopathy, neovascular age-related macular degeneration, and corneal neovascularization related diseases. Although vascular endothelial growth factor (VEGF) is the main pro-angiogenic factor to drive ocular neovascularization and anti-VEGF treatment is the standard therapy for ocular neovascularization, its application still has challenges due to ocular and systemic side effects. In this study, therapeutic effects against disease phenotypes in representative vison-threatening ocular diseases mouse models were investigated as they were administered through intraocular drugs injection.

Methods: 1) With a developed antibody-drug conjugate (ADC) targeting mouse platelet-derived growth factor receptor β (mPDGFRβ), experiments were performed including *in vitro* flow cytometry, cell viability test, and confocal microscopy using mouse brain vascular pericytes (MBVP) and *in vivo* the mouse models of oxygen-induced retinopathy and laser-induced choroidal neovascularization to assess the internalization and cytotoxic effect of ADC, and suppressive effect of retinal and choroidal neovascularization. 2) Immunocytochemistry, real-time polymerase chain reaction (RT-PCR), western blot analysis, flow cytometry, trans-epithelial permeability test, and trans-epithelial electrical resistance measurement, enzyme-linked immunosorbent assay were conducted to investigate the additional effect of structural and functional integrity of adult retinal pigment epithelial cell line-19 (ARPE-19) according to modulation of macrophage polarization under the co-culture conditions. Immunofluorescence

staining and fluorescence-labeled dextran vascular leakage test and RT-PCR were conducted to evaluate whether M2 macrophage polarization suppresses outer blood-retinal barrier disruption and vascular leakage in streptozotocin (STZ)-induced diabetic mouse model.

3) Experiments were performed including immunocytochemistry, immunofluorescence staining, western blot analysis, measurement of reactive oxygen species in the transforming growth factor-β1 (TGF-β1)-treated ARPE-19 cells and intravitreally TGF-β1-treated mouse model to evaluate preventive effect of activator of AMP-dependent protein kinase, 5-aminoimidazole-4carboxamide ribonucleotide (AICAR) or nicotinamide adenine dinucleotide phosphate oxidase (NOX) 4 inhibitor, GKT137831 against TGF-β1-induced morphometric change and epithelial mesenchymal transition (EMT) of retinal pigment epithelium (RPE).

4) Immunocytochemistry, angiogenesis assay, and western blot analysis of human dermal lymphatic endothelial cells (HDLECs) were conducted to assess the involvement of substance P (SP)/neurokinin-1 receptor (NK1R) system in lymphangiogenesis. Immunohistochemistry, corneal fluorescein staining, and phenol red thread test, and RT-PCR were used to evaluate the effect of SP signaling blockade in the corneal lymphangiogenesis.

Results: 1) ADC targeting mPDGFRβ is effectively internalized into MBVPs and showed cytotoxicity. Specific removal of PDGFRβ-overexpressing pericytes using ADC significantly inhibits pathologic retinal and choroidal neovascularization in mouse models of oxygen-induced retinopathy and laser-induced choroidal neovascularization.

2) Alteration of macrophage polarity additionally influenced the structural and functional integrity of APRE-19 cells under high glucose conditions. Intravitreal

IL-10 injection induced M2 microglia/macrophage polarization and effectively suppresses outer blood retinal barrier disruption and vascular leakage in the early-stage of STZ-induced diabetic mouse model.

3) Inhibition of the mammalian target of rapamycin complex 1 or NOX4 signaling pathway by treatment with AICAR or GKT137831 attenuated EMT of RPE and improved morphological stability of RPE the in vitro and in vivo.

4) Blockade of SP signaling with L733,060, an antagonist of NK1R, or NK1R-targeted siRNA significantly inhibited lymphangiogenesis and expression of vascular endothelial growth factor (VEGF) receptor 3 stimulated by SP in HDLECs. NK1R antagonist also suppressed pathological corneal lymphangiogenesis and ameliorated the clinical signs of dry eye *in vivo*. NK1R antagonist effectively suppressed the lymphangiogenic factors, including VEGF-C, VEGF-D, and VEGF receptor 3 in the corneal and conjunctival tissues of dry eye disease.

Conclusions: Intraocular injection of therapeutic modalities such as ADC, small molecules, and protein effectively suppressed pathologic neovascularization and vascular abnormalities in the retina, choroid, and cornea. Meticulous toxicity studies to minimize the potential ocular toxicity on these drugs and further studies to rull out confounding factors might facilitate biomedical application of therapeutics against vison-threatening ocular diseases.

* A part of this work is based on published articles in Communications medicine (1), FASEB J (2), Ocular surface (3).

Keywords: Choroidal neovascularization, Corneal neovascularization, Retinal neovascularization, Epithelial-mesenchymal transition, Intraocular injection, Outer blood-retinal barrier

Student number: 2018-38536

CONTENTS

LIST OF FIGURES

Chapter 1

Chapter 2

Chapter 3

LIST OF ABBREVIATIONS

AMD, age-related macular degeneration

ARPE-19, adult retinal pigment epithelial cell line-19

BRB, blood-retinal barrier

CEC, controlled environment chamber

CNV, choroidal neovascularization

DED, dry eye disease

DME, diabetic macular edema

DR, diabetic retinopathy

EMT, Epithelial-mesenchymal transition

HDLEC, human dermal lymphatic endothelial cell

MBVP, mouse brain vascular pericyte

mPDGF, mouse platelet-derived growth factor

NK1R, neurokinin-1 receptor

OIR, oxygen-induced retinopathy

ROP, retinopathy of prematurity

RPE, retinal pigment epithelium

RP-HPLC, reverse phase-high performance liquid chromatography

siRNA, small interfering RNA

STZ, streptozotocin

SP, substance P

TEER, trans-epithelial electrical resistance

TGF-β, transforming growth factor beta

VEGF, vascular endothelial growth factor

GENERAL INTRODUCTION

1.1. Study Background

Angiogenesis is the formation of new blood vessels from preexisting vasculature. It has fundamental importance in the diseases of various organs and health (4). The ocular angiogenesis can occur in anterior segment including cornea, conjunctiva, iris as well as posterior segment including retina, choroid. The pathologic ocular angiogenesis and vascular abnormalities are related to a broad spectrum of vison-threatening disorders such as retinopathy of prematurity (ROP), diabetic retinopathy (DR), age-related macular degeneration (AMD), corneal neovascularization related diseases secondary to hypoxia, ischemia, infection or inflammatory processes or genetic variations (5).

Angiogenesis is the process regulated by a dynamic balance between endogenous pro-angiogenic and anti-angiogenic factors. When this balance is disturbed by various stimuli, the angiogenic switch turn on for ocular neovascularization progression. These newly formed blood vessels are exudative, resulting in the accumulation of extracellular fluid to the intraretinal or subretinal space subsequent to impairment of retinal function (6) and interfering with normal corneal tissue structure, leading to recurrent corneal erosion, corneal opacity, and corneal edema (7, 8).

The representative pro-angiogenic growth factors in ocular angiogenesis related diseases are vascular endothelial growth factor (VEGF), platelet-derived endothelial growth factor (PDGF), angiopoietin, fibroblast growth factor, and matrix metalloproteinases, whereas anti-angiogenic factors are pigment epithelium-derived factor, endostatin, and angiostatin (5). Modulating the pro- and anti-angiogenic factors has been examined to control the pathologic ocular neovascularization using various therapeutic modalities such as small molecule, peptide, protein, polymer, nanoparticle, gene therapy (9-12).

Among the various factors, VEGF is the most effective angiogenic factors that drives neovascularization common to corneal, retinal, and choroidal vascular beds and regulates vascular endothelial cellular proliferation, migration, tube formation and permeability (9, 13, 14). Clinical studies have confirmed that high VEGF levels in ocular fluid and tissues are found in several ocular diseases, including ROP (15-17), DR (18-20), AMD (21-23), corneal

neovascular diseases (24, 25). Intravitreal injection of anti-VEGF agents for suppressing retinal or choroidal neovascularization in ROP (26-28), diabetic macular edema (DME) (29-31), AMD (32-34) and subconjunctival/intrastromal/topical treatment of anti-VEGF agents for suppressing corneal neovascularization (35-37) significantly improves anatomical outcomes and visual development in patients.

Although anti-VEGF treatment is the mainstream therapy for ocular neovascularization, its application still has challenges. First, some patients still show ocular side effects including recurrence or progression of neovascular lesion (38-41), geographic atrophy (42), ocular hypertension (43), retinal vascular occlusion (44), hemorrhagic macular infarction (45), and tractional retinal detachment (46) despite anti-VEGF treatment. Second, systemic side effects from repeated use of anti-VEGF agents associated with cardio-/cerebrovascular accidents, hypertension, proteinuria and non-ocular hemorrhage (47-49) can still occur even though anti-VEGF therapy is locally administered into the eye and the dosage is more than 100-fold lower than that used in oncology (50). Finally, as VEGF plays an important role in maintaining healthy cardiovascular, renal, and ocular system including retinal and choroidal vasculature, retinal neurons, glial cells, and corneal nerves, chronic suppression of VEGF may lead to inhibitory VEGF's trophic effects (51-55). Given these challenges, there are still unmet needs to develop novel molecular targets and therapeutics.

1.2. Purpose of Research

In this study, we tried to investigate potential therapeutic targets to suppress pathological neovascularization and vascular abnormalities of the retina, choroid, and cornea utilizing pathologic vision-threatening ocular disease mouse models.

Retinopathy of prematurity (ROP)

ROP is a leading cause of childhood vision loss worldwide. The development of ROP progression is characterized by incomplete vascularization and abnormal neovascularization, leading to vitreous hemorrhage, intraocular fibrosis, and retinal detachment.

Oxygen-induced retinopathy (OIR) mouse model is a well-established model to study

not only ischemia-induced pathological retinal neovascularization but also physiologic retinal revascularization of the previous ischemic area (56, 57). This model is based on the exposure of mouse pups to hyperoxia during a phase when their retinal vasculature is still developing. This leads to vascular obliteration, and upon return to room air, results in retinal ischemia and proliferative vascular formation.

We have interested in the role of pericytes in developing pathologic retinal neovascularization and physiologic revascularization of previous ischemic area in OIR mouse mouse model. Pericytes are contractile cells that interact with endothelial cells stabilizing the newly formed pathologic neovessels. Especially, the ligand/receptor pair of platelet-derived growth factor BB (PDGF-BB) and PDGF receptor β (PDGFRβ), primarily expressed by vascular endothelial cells and pericytes in the ocular system, respectively induces the recruitment of pericytes to neovessels and secretion of VEGF and other cell survival factors from pericytes. Subsequently, these protective functions of pericytes are considered to enable endothelial cell survival independent of VEGF, rendering anti-VEGF therapy less efficient.

In this study, we investigated a pericyte-targeting antibody-drug conjugate (ADC) in which a protein that can target a specific antigen on the cell surface is chemically linked to a cytotoxic drug that kills target cells for its ability to suppress retinal neovascularization formation.

Diabetic retinopathy (DR)

DR is a highly specific neurovascular complication of both type 1 and type 2 diabetes (31). Vision loss due to diabetic retinopathy is generally induced by macular edema because of the increased permeability of retinal and choroidal vessels. These microvascular lesions have been regarded as central to the pathogenesis of DR and diabetic macular edema (DME) (6).

However, in recent years, studies reported that retinal neurovascular units composed of retinal neurons, glial cells, and vascular cells have undergone pathological changes such as retinal ganglion cells death, pericyte loss, astrocyte loss, and microglia/macrophage activation implicated in inner or outer blood-retinal barrier (BRB) breakdown preceding retinal vascular injury (58). Thus, neuroinflammation as well as microvascular injury has been involved in the pathogenesis of DME.

Especially, retinal microglia/macrophage activation and phenotypic change have been observed in diabetic animal models (59-62) and DR patients (63), indicating that the activation of microglia/macrophages is a specific feature of DR. Although studies regarding the role of microglia/macrophages in inner and outer BRB breakdown resulting in vascular leakage and macular edema are rarely addressed, there are some reports that microglia/macrophages release pro- and anti-inflammatory cytokines in response to the progression of diabetes and the cytokine balance is disrupted in favor of a pro-inflammatory milieu.

In this study, we aimed to investigate whether the microglia/macrophage polarity change by intravitreal interleukin 10 (IL-10), M2 inducer injection could suppress outer BRB disruption in the early stage of streptozotocin (STZ)-induced diabetic mouse model.

Age-related macular degeneration (AMD)

AMD is the leading cause of vision loss in individuals >55 years of age in developed countries, affecting the complex of photoreceptors, retinal pigment epithelium (RPE), Bruch's membrane, and choroid. AMD is classified as non-neovascular (dry type AMD) or neovascular (wet type AMD) forms (64). AMD is a multifactorial disease comprising a complex interplay between aging, genetic susceptibility such as complement factor H (CFH), age-related maculopathy susceptibility 2/high-temperature requirement protein A1, ARMS2/HTRA1, and environmental risk factors (12, 65).

Although the pathogenesis of diseases is not fully understood, RPE dysfunction is one of the important pathologic triggers to progress AMD. RPE cells perform various essential functions in retinal homeostasis, including phagocytosis of photoreceptor outer segments, formation of outer BRB, transport of nutrients, ions, water, and lipid homeostasis. In the aging process with affected by genetics and environmental factors, physiologic actions of RPE gradually decline. Dysfunction of lipid homeostasis, proteostasis and mitochondrial failure are the primary inducers of RPE dysfunction, leading to accumulation of drusen, morphometric change such as change of cell size and cell density, dysregulation of extracellular matrix, epithelial-mesenchymal transition (EMT), RPE and outer retinal cell atrophy (geographic atrophy), and pathologic choroidal neovascularization in dry and wet type AMD (65, 66).

In this study, we investigated whether the intravitreal injection of TGF-β1 triggers morphometric changes and EMT of RPE observed in the process of normal aging and AMD patients for establishing a screening model for AMD therapeutics and examined if these processes can be prevented by suppressing mammalian target of rapamycin complex 1 (mTORC1) or NADPH oxidase (NOX) signaling. In another study, we examined whether removing PDGFRβ-overexpressing pericytes by an ADC targeting PDGFRβ could suppress choroidal neovascularization in laser-induced choroidal neovascularization (LI-CNV) mouse model simulating the neovascular (wet type) AMD in humans.

Dry eye disease (DED)

DED is a multifactorial disorder of the ocular surface initiated by desiccating stress, ocular surface inflammation, tear film instability, hyperosmolarity, and neurosensory abnormalities causing a visual disturbance and ocular discomfort (67). Corneal neovascularization is a common endpoint in different ocular surface diseases such as chemical burns, trauma, autoimmune disease, infectious corneal diseases, and DED (68). Notably, DED involves a unique form of selective corneal lymphangiogenesis without associated hemangiogenesis in experimental and clinical settings (69, 70). These newly formed lymphatic vessels in the cornea provide potential pathway by which inflammatory cells including antigen-presenting cells migrate from the ocular surface to draining lymph nodes ultimately leading to ocular surface inflammation and visual disturbance (71).

The abundant supply of sensory and autonomic nerve fibers on the ocular surface plays an imperative role in maintaining healthy corneal layers and serves as the main source of neurogenic inflammation (72). The neuropeptides released from ocular surface epithelial cells, lacrimal gland tissues, and nerve endings at the inflammatory sites involve in ocular surface inflammation by pro-inflammatory cytokines and chemokines secreted by immune cells, corneal neovascularization, and wound healing, causing reflex tearing and ocular discomfort (73-75).

Substance P (SP) is an 11-amino acid neuropeptide produced by neuronal cells and inflammatory cells, exerting its inflammatory and immunological activity via a high-affinity neurokinin-1 receptor (NK1R) (76, 77). There has been reported that the relationship between

SP/NK1R system and corneal lymphangiogenesis in diverse corneal inflammatory conditions (78, 79).

In this study, we evaluate the role of the SP/NK1R system in the regulation of pathologic corneal lymphangiogenesis in DED utilizing a controlled environment chamber-induced dry eye mouse model.

CHAPTER 1-1

Regulation of Retinal Neovascularization in Retinopathy of Prematurity via Intravitreal Antibody-Drug Conjugate Injection

INTRODUCTION

Retinopathy of prematurity (ROP) is defined as immature retinal abnormalities characterized by an arrest of physiologic retinal vascularization (NV) and an increase in pathologic retinal neovascularization in premature infants, which typically occurs in two postnatal phases (80-83). In the first phase, immediately after birth up to 32 weeks' postmenstrual age (PMA), suppression of vascular endothelial growth factor (VEGF) and insulin growth factor-1 (IGF-1) due to relative hyperoxia and loss of the maternal-fetal interaction after preterm birth result in cessation of retinal vascularization, which leads to capillary obliteration and partial regression of existing vessels (83-85). In the second phase which generally begins between 32 and 34 weeks' PMA, incomplete vascularization and an increase in metabolic burden cause the retina to become hypoxic, stimulating an increase in hypoxia-inducible factor-1 (HIF-1) that triggers the release of various angiogenic factors including VEGF, IGF-1, and erythropoietin (86). Subsequently, this causes an increase in pathologic retinal vaso-proliferation, leading to retinal hemorrhage, fibrovascular proliferation, and retinal detachment, which can result in blindness (87).

Over the past several decades, peripheral retinal ablation by cryotherapy (88, 89) or laser (90, 91) has been the standard treatment for inhibiting aberrant pathologic retinal NV to prevent fibrovascular retinal detachment. Although these retinal ablations showed an improvement in anatomical outcomes and visual development, the side effects of ablation of the avascular retina such as refractive errors, early emmetropization, astigmatism, and visual field constriction have remained (92-96).

The intravitreal anti-VEGF therapy is a recent development in the treatment of ROP (97) based on the experimental evidence that downregulation of intraocular VEGF concentration to physiologic level locally could both inhibit retinal neovascularization and facilitate physiologic retinal vascular development of the previous avascular retina by reorienting proliferating vascular endothelial cells (98-100). Despite promising outcomes of anti-VEGF treatment in various clinical studies (26, 28, 97, 101, 102), there are concerns about anti-VEGF therapy, including reports that reactivation, ROP recurrence is seen more frequently than spontaneous regression, and completed laser photocoagulation (27, 38, 40, 103).

Furthermore, the impact on physiologic angiogenesis in other organs, and potential adverse effects on the neural retina in developing preterm infants cannot be ignored after anti-VEGF therapy.

In addition to VEGF, several molecules participate in the development of retinal NV, including platelet-derived growth factor (PDGF), placental growth factor, erythropoietin, IGF-1, and erythropoietin. Among them, PDGF is a multifunctional peptide with a biologically active form composed of A, B, C, and D chain dimers and a heterodimer composed of A and B. PDGF-BB is the predominant isoform in the ocular system, which is mainly expressed by vascular endothelial cells and is involved in sprouting angiogenesis and vasculogenesis during embryonic development (104, 105). PDGF receptors (PDGFRs) are receptor tyrosine kinase homo- or heterodimeric proteins composed of α and β subunits that activates downstream pathways through binding with PDGF (106), which are mainly expressed on the pericytes, smooth muscle cells in the ocular system. The crosstalk between PDGF-BB/PDGFRβ facilitates vessel maturation under pathologic conditions by promoting pericyte recruitment to NV in the retina and supporting pericyte-endothelial interaction (107). Based on these previous studies, we hypothesized that the strong pericytes-endothelial cells interaction enables for endothelial cells to survive despite intravitreal anti-VEGF treatment, resulting non-responder for anti-VEGF drugs in ROP patients. We wondered whether specific delivery of cytotoxic reagents to PDGFRβ-overexpressing cells such as pericytes are effective in suppressing pathologic retinal NV.

Antibody-drug conjugates (ADCs) are monoclonal antibodies covalently linked to a potent cytotoxic agent that induce cell death upon binding and internalization of the antibody by the target cell (108). In a series of studies, we have developed a unique ADC by combining bispecific anti-mouse PDGFRβ (mPDGFRβ) × cotinine single-chain variable fragment (scFv)-human kappa constant (C_κ)-scFv fusion protein and cotinine-conjugated duocarmycin and demonstrated it could specifically induce cytotoxicity toward PDGFRβ-expressing pericytes (109). In the current study, we tested whether this ADC could ablate pericytes and suppress retinal NV in an oxygen-induced retinopathy (OIR) mouse model.

MATERIALS AND METHODS

1. Cell culture

Mouse brain vascular pericytes (MBVPs) were obtained from iXCells Biotechnologies (San Diego, CA, USA) and maintained in mouse pericyte growth medium (MD-0092; iXCells Biotechnologies) supplemented with 1% penicillin/streptomycin (Gibco, Grand Island, NY, USA).

2. Preparation of bispecific scFv-Cκ-scFv fusion protein and ADC targeting mPDGFRβ

Anti-mPDGFRβ × cotinine was expressed and purified as described previously (109). Clone PRb-CN01 developed in our previous study was used for anti-mPDGFRβ scFv. As a control, we also prepared anti-HER2 × cotinine bispecific scFv-Cκ-scFv fusion protein (anti-HER2 × cotinine), where anti-HER scFv was derived from trastuzumab (109). The expression vectors encoding these bispecific scFv-Cκ-scFv fusion proteins were transfected into Expi293F cells (Thermo Fisher Scientific Inc., Waltham, MA, USA), and the scFv-Cκ-scFv fusion proteins were purified using KappaSelect resin (GE Healthcare, Buckinghamshire, UK) following the manufacturer's instructions. ADC targeting mPDGFRβ was prepared by mixing antimPDGFRβ × cotinine (1 μM) with cotinine-duocarmycin (1 μM) at a 1:1 molar ratio as described previously (109). The complex was then incubated for 30 minutes at room temperature (RT) to allow complex formation before being used. Control ADC was prepared in the same way. The schematic diagrams of a bispecific antibody, cotinine-duocarmycin, and the conjugation process are represented in Fig. 1.2A and B. The RP-HPLC analysis that empirically determine the drug-to-antibody ratio were performed by Levena Biopharma (San Diego, CA, USA) and the data are shown in in Fig. 1.2C.

3. Flow cytometry

MBVPs were incubated with either anti-mPDGFRβ × cotinine (100 nM) or control scFv-Cκ-scFv fusion protein in flow cytometry buffer (1% [w/v] BSA in Phosphate buffered saline (PBS) containing 0.05% [w/v] sodium azide) at 4 °C for 1 h. After washing four times with the

flow cytometry buffer, the cells were probed with APC-conjugated anti-human Cκ antibody (1:100 dilution, clone TB28-2; BD Biosciences, San Jose, CA, USA). For each sample, the data were acquired from 10,000 cells, and the results were analyzed using FlowJo (Tree Star, Ashland, OR, USA).

4. Immunocytochemistry

MBVPs were incubated with mouse pericyte growth medium containing anti-mPDGFRβ × cotinine (10 μg/mL) with or without mPDGF-BB (50 ng/mL; 315-18; Peprotech, Rocky Hill, NJ, USA) for 30 minutes at 37 °C as described previously51–53. Next, the cells were blocked by incubation with 0.1% Triton X-100 and 5% horse serum (GIBCO) in PBS for 30 minutes. Subsequently, the cells were incubated with FITC-conjugated anti-human Cκ antibody (2 μg/mL; TB28-2; BD Biosciences) for 30 minutes at room temperature. Early endosomes were imaged by incubating the cells with 1:200 diluted anti-Rab5 antibody (#C8B1; Cell Signaling Technology, Danvers, MA, USA) and Alexa Fluor 546-conjugated goat anti-rabbit IgG (#A-11035; Invitrogen, Carlsbad, CA, USA). To detect cellular DNA, 4′,6- diamidino-2-phenylindole (DAPI, 0.2 μg/mL) was used. Confocal images were acquired using a Zeiss LSM 880 microscope at Ewha Fluorescence Core Imaging Center, and the images were processed with Zen software (Carl Zeiss, Thornwood, NY, USA).

5. Cytotoxicity assay

MBVPs ($4x10^3$ cells) in 50 μL mouse pericyte growth medium were seeded in 96-well plates (#CLS3595; Corning Inc., Corning, NY, USA) and incubated overnight at 37°C in a humidified atmosphere with 5% CO2. ADCs (2 μM) were diluted by 5 folds (0.024 nM to 2 μM) and mixed 1:1 with medium with or without mPDGF-BB (8 nM). ADCs [0.012 nM to 1 μM] with or without mPDGF-BB (4 nM), at a total volume of 50 μL, were added to the pre-seeded cells in 50 μL of medium, yielding a total volume of 100 μL. ADCs [0.006–500 nM] with or without mPDGF-BB (2 nM) were then incubated with the cells for 72 hours at 37°C in a humidified atmosphere with 5% CO2.

6. Mice

C57BL/6J mice were maintained in a specific pathogen-free facility at Seoul National University. The mice (aging-matched: 6- week-old, weight range: 20–24 g) were allocated into experimental groups. The total number of mice used in each experiment was determined based on the preliminary result of the OIR mouse study using ADC. No statistical methods were used to predetermine sample size. All animal procedures were approved by the Seoul National University Animal Care and Use Committee (Permit Number: SNU-171203-1-2) and were conducted following the guidelines of the Association for Research in Vision and Ophthalmology Statement for the use of Animals in Ophthalmic and Vision Research.

7. Immunofluorescence staining

The eyes from 6-week-old wild-type C57BL/6J male mice were enucleated and fixed with 4% paraformaldehyde (#P2031; Biosesang, Seongnam, Gyeonggi-do, Korea) for 15 minutes at room temperature. After washing with PBS, the eyes were gently dissected to remove all components except the retina. The retinas were whole mounted and incubated in Perm/Block solution (0.2% Triton X-100 and 0.3% BSA in PBS) at room temperature for 1 hour. Next, the samples were incubated overnight at 4°C with rabbit anti-PDGFRβ antibody (1:100; #3169, Cell Signaling Technology, Danvers, MA, USA). After washing with PBS, the samples were incubated at room temperature for 2 hours with Alexa Fluor 647- labeled donkey anti-rabbit IgG antibody (1:400; #A31573; Invitrogen, Carlsbad, CA, USA). After washing with PBS, the samples were stained with Alexa Fluor 568-conjugated anti-IB4 antibody (1:400; #I21412; Invitrogen, Carlsbad, CA, USA) and Alexa Fluor 488-conjugated anti-NG2 antibody (1:400; #AB5320A4; Sigma- Aldrich, St. Louis, MO, USA) at room temperature for 2 hours. After washing with PBS, the samples were counterstained with 10 mg/ml of DAPI (1:1000; #D9542; Sigma-Aldrich, St. Louis, MO, USA) at room temperature for 15 minutes. After washing with PBS, the retina and RCS complexes were mounted with Fluoromount™ Aqueous Mounting Medium (#F4680, Sigma-Aldrich, St. Quentin, France) and observed under a confocal microscope (Leica TCS STED; Leica Microsystems Ltd., Wetzlar, Germany)

8. Induction of oxygen-induced retinopathy

OIR was induced in C57BL/6J wild-type mice. Briefly, newborn pups (male and female) and their nursing dam were placed in 75 ± 0.5% oxygen in an O2-regulated chamber with an oxygen controller (Pro-Ox 110 Chamber Controller; Biospherix, Redfield, NY, USA) from P7 to P12 and then returned to room air. On P14, each group received an intravitreal injection of PBS as a vehicle control, control ADC (66.77 pg), ADC targeting mPDGFRβ (66.77 pg) or bevacizumab (1 μg/eye, bevacizumab, Avastin®; Genentech Inc., San Francisco, CA). To administer the indicated reagents intravitreally, a microliter syringe with a 33G blunt needle (Hamilton Bonaduz AG, Bonaduz, Switzerland) was inserted into the vitreous cavity through the 6 o'clock position of the limbus with a 45° injection angle for the right eye, followed by gently loading the solutions under the surgical microscope (Leica Microsystems, Ltd., Wetzlar, Germany). Intravitreal injection was only conducted in the right eye. After euthanization of the mice on P17, the retina was isolated, fixed, and mounted. After immunofluorescence staining with Alexa Fluor 568-conjugated anti-IB4 antibody (1:200; #I21412; Invitrogen, Carlsbad, CA, USA) and Alexa Fluor 488 conjugated anti-NG2 antibody (1:200; #AB5320A4; Sigma-Aldrich, St. Louis, MO, USA) as described previously, manifestations of oxygen-induced vascular pathology (avascular area and neovascular tufts) were visualized and imaged using a confocal microscope. Area quantification was performed using ImageJ 1.42 software (National Institutes of Health, Bethesda, MD, USA). For analyzing NG2 or PDGFRβ coverage to neovascular tufts and peripheral retinal vasculature, we randomly choose a sampling box of four sites per eye at the mid-periphery region (neovascular tufts area) and peripheral region (peripheral vascularized area), respectively in the whole-mounted retinas and converted to 3D immunofluorescence image format using a built-in measuring tool of the LAS X system (Leica Microsystems Ltd., Wetzlar, Germany).

9. Histologic evaluation of retinas from mice treated with ADC targeting mPDGFRβ

ADC targeting mPDGFRβ (667.7 pg), control ADC (667.7 pg), or PBS was injected intravitreally into 6- week-old wild-type C57BL/6J male mice (n = 6 per group, n = 18 in total). One week after the injection, the eyes were enucleated, fixed in 4% paraformaldehyde, and

embedded in paraffin. After 4-μm-thick paraffin sections were prepared, the sections were deparaffinized and hydrated by sequential immersion in xylene substitutes and graded ethyl alcohol solutions. Next, the sections were processed by either hematoxylin and eosin (H&E) or terminal deoxynucleotidyl transferase dUTP nick end labeling (TUNEL) staining. To evaluate changes in the retinal layers, the retinal layer thickness ratio was calculated as follows: retinal thickness from the internal limiting membrane to the inner nuclear layer/retinal thickness from the internal limiting membrane to the outer nuclear layer. This was compared with the ratio in control mice. TUNEL staining was performed using an in-situ cell death detection kit (#1164795910; Sigma-Aldrich, St Louis, MO, USA). The nuclei were counterstained with DAPI, and TUNEL-positive cells were counted in five randomly selected fields in each slide (×200) under a fluorescence microscope.

10. Electroretinography

To assess the retinal function by electroretinography (ERG), the mice were dark-adapted for over 16 hours before electroretinogram monitoring. After deep anesthesia and dilatation of the pupils with an eye drop containing phenylephrine hydrochloride (5 mg/ml) and tropicamide (5 mg/ml), the mice were placed on a heating pad in a Ganzfeld dome to maintain their body temperature. The contact lens electrode was placed in the center of the cornea after instilling artificial tears. The reference electrode was located at the forehead, and the ground electrode was located at the tail. Full-field ERG was recorded using the universal testing and electrophysiologic system (UTAS E-3000; LKC Technologies Inc., Gaithersburg, MD, USA). In the dark-adapted condition, the scotopic responses were recorded using a series of white flashes of increasing intensities ranging from −5.0 to 0.0 log (cd·s/m2) using a notch filter at 60 Hz and a digital bandpass filter ranging from 0.3 to 500 Hz. After the completion of the dark-adapted stimulus series, the mice were projected with a steady field of light (20 cd·s/m2) for 15 minutes to desensitize rods. In the light-adapted condition with 1.3 log (cd·s/m2) background, the photopic responses were recorded ranging from 0.39 to 1.39 log (cd·s/m2) with the filter ranging from 2 to 200 Hz. After averaging the signals, the amplitudes were measured by the built-in software (UTAS visual electrodiagnostic system with EMWin, LKC Technologies Inc.,

Gaithersburg, MD, USA) and used for analysis.

11. OptoMotry test

A virtual optomotor system (OptoMotry apparatus; CerebralMechanics Inc., Lethbridge, Alberta, Canada) was used to assess visual function. Briefly, the mice were placed on an elevated platform positioned in the middle of an arena created by four inward-facing display monitors. Spatial frequency thresholds were assessed using a video camera to monitor the elicitation of the optokinetic reflex through virtual stimuli projected with sine-wave gratings (100% contrast) on the computer monitors. Experimenters were blinded to the treatment and each animal's previously recorded thresholds.

12. Statistics and reproducibility

Statistical analyses were performed using SPSS software version 22.0 (SPSS Inc., Chicago, IL, USA) and GraphPad Prism v.8.0.1. The experimental data were presented as mean ± standard error of the mean. *P* values were determined using one-way ANOVA and Tukey post-hoc tests for multiple groups. All the data in our manuscript were repeated at least three times independently with similar results. The experiments were not randomized, and the investigators were not blinded to allocation during experiments and outcome assessment.

RESULTS

PDGFRβ is highly expressed on pericytes in pathologic neovessels of oxygen-induced retinopathy mouse model.

Immunofluorescence staining of the whole mounted retina in wild-type mice and OIR mice on postnatal day 17, was performed to determine the expression patterns of PDGFRβ in the retina of OIR mice. The whole mounted retina was stained with anti-PDGFRβ, anti-isolectin B4 (IB4), or anti-neural/glial antigen 2 (NG2) antibodies. We found that PDGFRβ was present mainly in the retinal perivascular area from the superficial vascular plexus to the deep vascular plexus and co-localization of the vascular endothelial cell marker IB4 and PDGFRβ was negligible in wild-type mice (Fig. 1.1A). In OIR mice, PDGFRβ was significantly overexpressed around the pathologic neovessels and the pericyte marker NG2 was remarkably co-localized with PDGFRβ in neovascular tufts (Fig. 1.1B), confirming that PDGFRβ was mainly expressed by pericytes.

Preparation and characterization of ADC targeting mPDGFRβ in vitro.

In a series of studies, we have developed a unique ADC composed of hapten-conjugated drugs and bispecific single-chain variable fragment (scFv)-human kappa constant (Ck)-scFv fusion protein that can bind simultaneously to hapten and antigen of interest. Cotinine, a major metabolite of nicotine, was used as a hapten due to its non-toxicity, physiological inertness, and exogeneity. This ADC, bispecific anti-mouse platelet-derived growth factor receptor β x cotinine scFv-Ck-scFv fusion protein (anti-mPDGFRβ x cotinine) and cotinine-conjugated duocarmycin, can be formed by simply mixing cotinine-conjugated drug and bispecific antibody with drug-to-antibody ratio (DAR) 4 determined by Reverse phase-high performance liquid chromatography (RP-HPLC) (Fig.1.2).

Then, we first confirmed that mouse brain vascular pericytes (MBVPs) express a high level of PDGFRβ by western blotting (Fig. 1.3). Next, we incubated the MBVPs with bispecific anti-mPDGFRβ x cotinine and probed with allophycocyanin (APC)-conjugated anti-human Ck antibody to evaluate internalization of the bispecific fusion protein into target cells. In parallel, the MBVPs were stained with anti-Rab5 reactive endosome-specific antibody. We found that

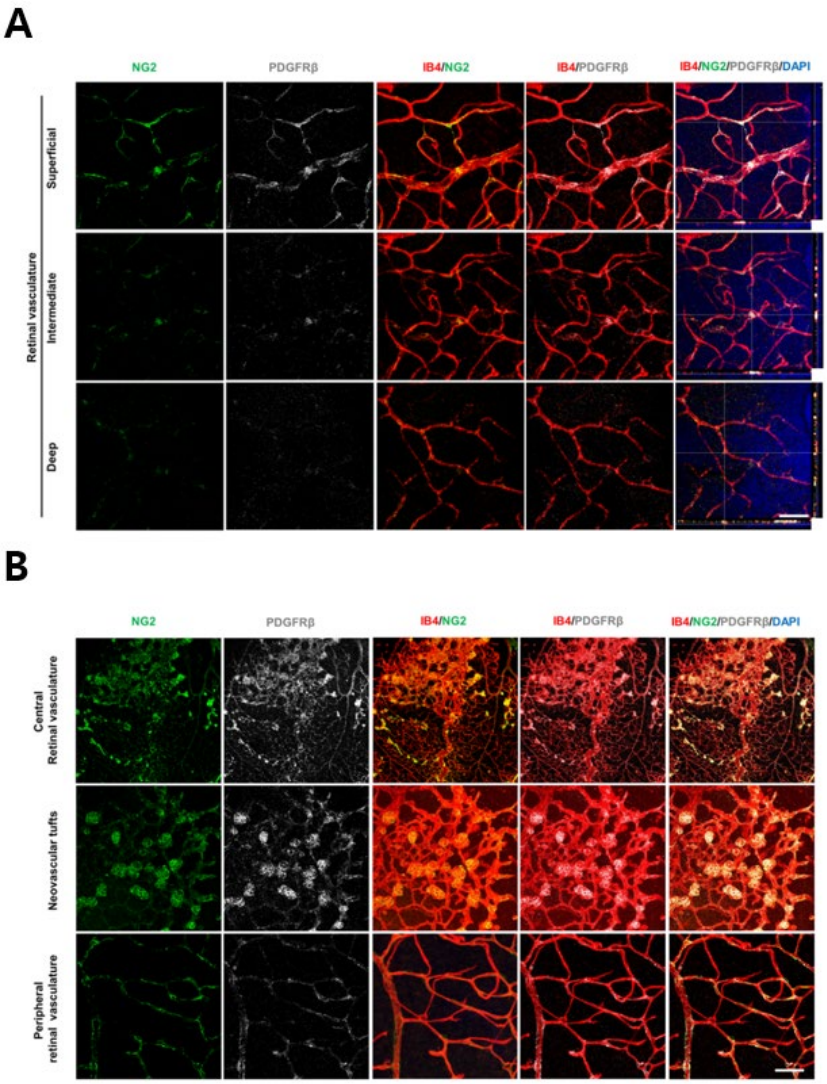

Figure 1.1. PDGFRβ is highly expressed on pericytes in pathologic neovessels of OIR mouse model.

(A) Representative immunofluorescence images of the retinal vasculature in wild-type (control) mice. Immunofluorescence images of anti-isolectin B4 (IB4, red), anti-neural/glial antigen 2 (NG2, green), platelet-derived growth factor receptor β (PDGFRβ, gray), and 4'6'-diamidino-2-phenylindole (DAPI, blue) showing that PDGFRβ expression is mainly localized in the retinal vessels and surrounding tissue.

(B) Representative immunofluorescence images of the retinal vasculature in an oxygen-induced retinopathy (OIR) mouse. PDGFRβ is highly overexpressed in the neovascular tufts.

bispecific antibody with drug-to-antibody ratio (DAR) 4 determined by Reverse phase-high performance liquid chromatography (RP-HPLC) (Fig.1.2).

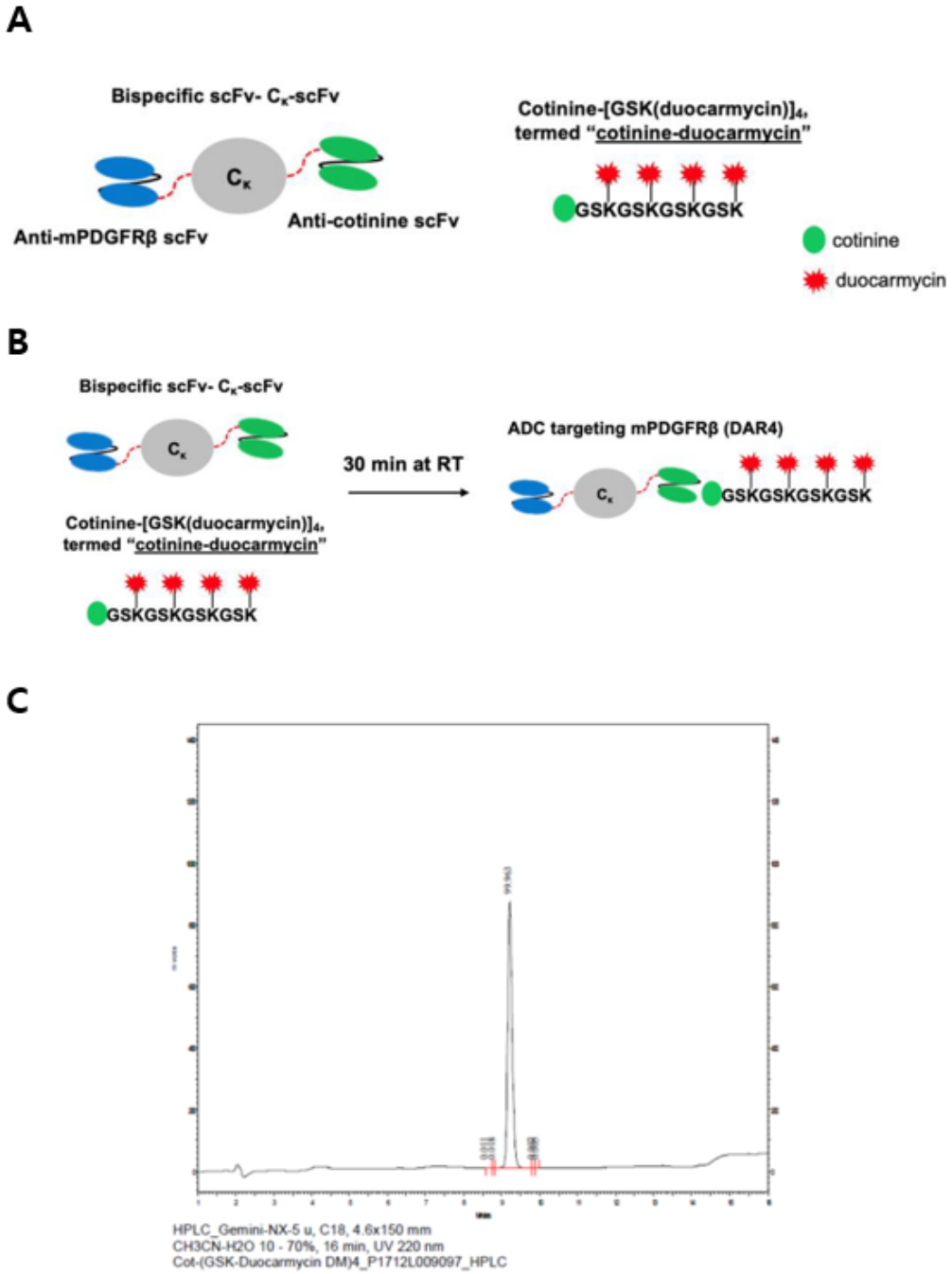

Figure 1.2. Schematic diagrams depicting the structure of a bispecific scFv-Ck-scFv antibody and its conjugation process with cotinine-duocarmycin to generate ADCs.

(A) The structures of a bispecific single-chain variable fragment (scFv)-human kappa constant (Ck)-scFv antibody (left) and the drug, cotinine-duocarmycin (right).

(B) The schematic representation of the conjugation process of a bispecific scFv-Cκ-scFv antibody and cotinine-duocarmycin. Incubation of the two molecules at room temperature for 30 minutes yields a drug-to-antibody ratio (DAR) 4 ADC.

(C) Reverse phase-high performance liquid chromatography (RP-HPLC) analysis. The RP-

HPLC analysis shows a single peak at >99% purity according to peak area integration at 220 nm absorbance. No other peaks indicating DAR < 4 or DAR >4 is detected by RP-HPLC.

* Figure 1.2 data was prepared by Soohyun Kim and Professor Junho Chung.

* The RP-HPLC analysis that empirically determine the drug-to-antibody ratio were performed by Levena Biopharma (San Diego, CA, USA).

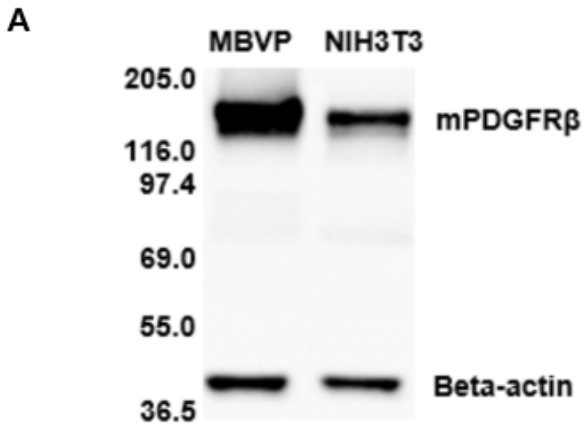

Figure 1.3. Comparison of the expression level of PDGFRβ in MBVP and NIH3T3.

(A) Western blot analysis of mouse platelet-derived growth factor receptor β (mPDGFRβ) from mouse brain vascular pericyte (MBVP) cells and NIH3T3 cells. The expression level of mPDGFRβ in MBVP cells was higher than that in NIH3T3 cells.

* Figure 1.3 data was prepared by Soohyun Kim and Professor Junho Chung.

anti-mPDGFRβ x cotinine was co-localized with an endosome-specific antibody, confirming that bispecific fusion protein was internalized via the classical endocytosis pathway (Fig. 1.4A). Thereafter, we demonstrated that internalized ADC targeting mPDGFRβ could effectively exert cytotoxicity against PDGFRβ expressing mouse pericytes compared with the control ADC in the absence or presence of mPDGFRβ-BB, showing a half maximal inhibitory concentration value of 0.19 nM (*P*-value < 0.001, Fig. 1.4B).

ADC targeting mPDGFRβ significantly suppresses retinal neovascularization and promotes retinal revascularization.

To investigate whether the ADC targeting mPDGFRβ could effectively ameliorate retinal neovascularization in the oxygen-induced retinopathy mouse model, newborn C57BL/6J wild-type mice were exposed to hyperoxia (75% O_2) for five days from postnatal day 7 (P7) to P12 to suppress physiologic vascular development. When the mice were returned to room air (normoxia), the relative hypoxia led to retinal NV, which began between P12 and P17. ADC targeting mPDGFRβ was administered into vitreous cavity on P14 and the retina was retrieved from the mice on P17 (Fig 1.5A) when the retinal NV was the most prominent (110, 111).

ADC targeting mPDGFRβ reduced areas of retinal NV and avascular zone, compared with the retina of mice injected with vehicle control or control ADC (*P*-value < 0.01, Fig 1.5B and C). The expression level of NG2 at retinal neovascular tufts was also significantly decreased in mice treated with ADC targeting mPDGFRβ, confirming that a reduction in the number of pericytes (*P*-value < 0.01, Fig 1.5B and D), whereas no significant differences were found in NG2 expression at peripheral vascularized retina among the ADC group and two control groups (*P*-value = 0.482, Fig 1.5B and D). These results suggest that pericytes in the neovascular tuft are more vulnerable than pericytes in the peripheral retinal vasculature against ADC targeting mPDGFRβ. We reconfirmed this tendency in the additional experiments comparing against ADC targeting mPDGFRβ with conventional anti-angiogenic agent (1 μg/eye, bevacizumab, Avastin®) (*P*-value = 0.482, Fig 1.6 and 1.7). This result is likely due to overexpression of PDGFRβ of the pericytes in the neovascular tufts than pericytes in the peripheral retinal vasculature, increasing efficiency of ADC targeting mPDGFRβ.

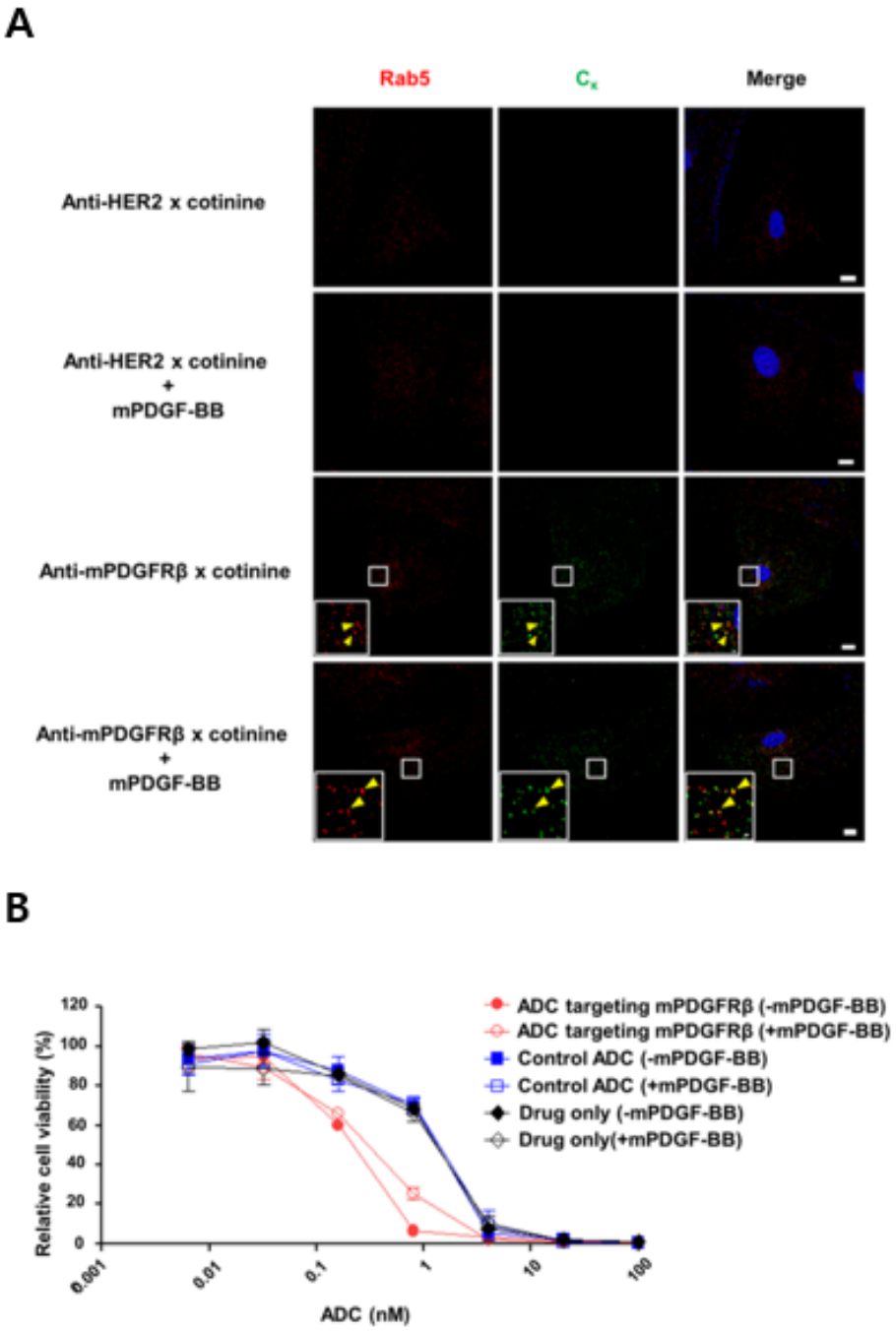

Figure 1.4. Preparation and characterization of ADC targeting mPDGFRβ.

(A) Confocal microscopy of the internalization of anti-mouse platelet-derived growth factor receptor β x cotinine scFv-Ck-scFv fusion protein (anti-mPDGFRβ x cotinine). Bispecific anti-human epidermal growth factor receptor 2 (HER2) × cotinine was used as a control fusion protein. Mouse brain vascuclar pericyte (MBVP) cells were incubated with bispecific scFv-Ck-scFv fusion proteins and probed APC-conjugated anti-human Ck antibody with or without mouse platelet-derived growth factor BB (mPDGF-BB). Scale bars in the image correspond to 10 μm.

(B) Cytotoxicity of ADC targeting mPDGFRβ. MBVP cells were incubated with ADC in the absence (-) or presence (+) of mPDGF-BB. The relative cell viability was measured by the cellular ATP level. Anti-HER2 × cotinine complexed with cotinine-duocarmycin was used as a control ADC and drug only refers to cotinine-duocarmycin in fresh media. The results are shown as means ± standard deviation (SD).

* Figure 1.4 data was prepared by Su Ree Kim, Soohyun Kim and Professor Dongmin Kang, and Junho Chung.

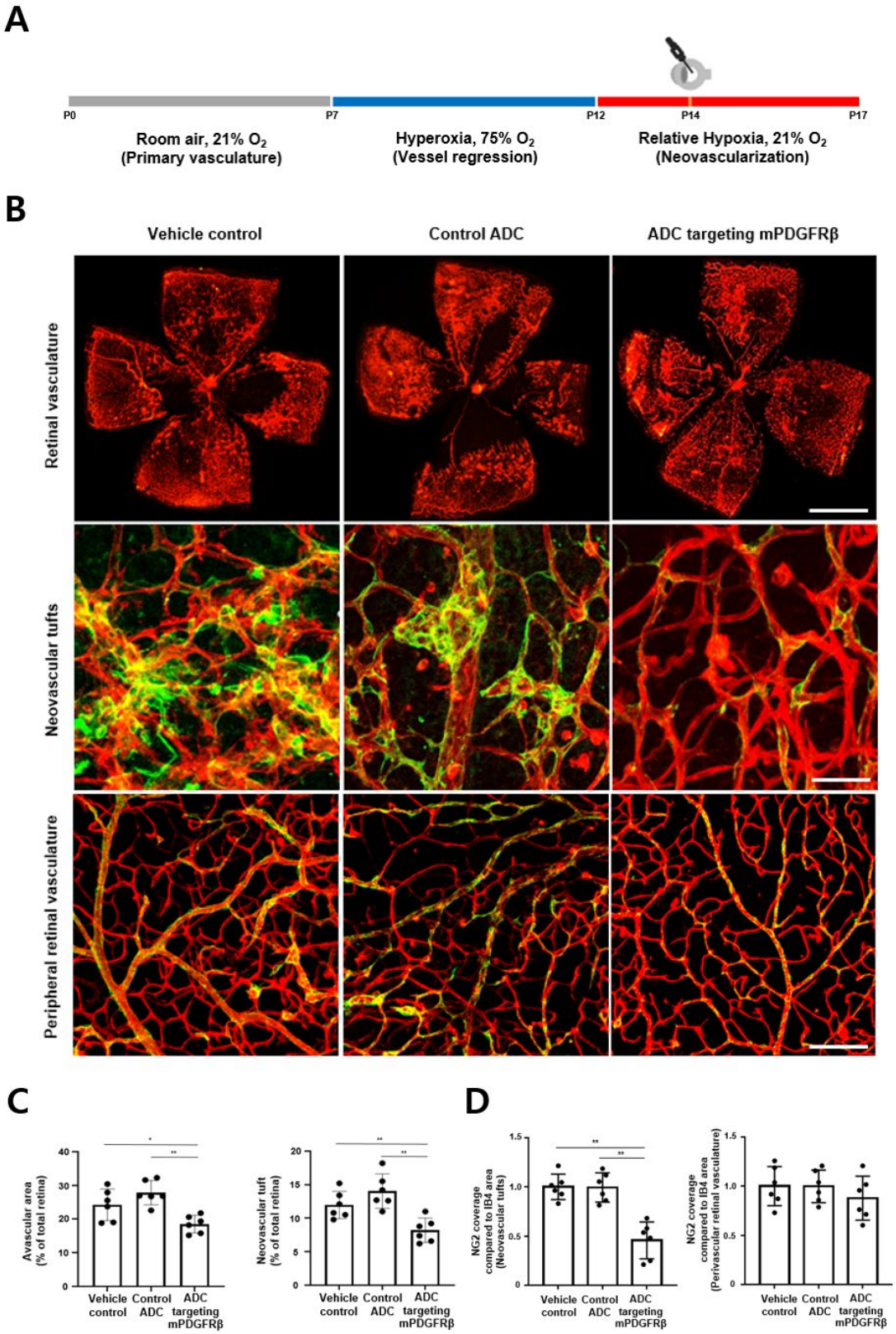

Figure 1.5. ADC targeting mPDGFRβ ameliorates retinal neovascularization in the OIR mouse model.

(A) Schematic experimental timeline of the oxygen-induced retinopathy (OIR) mouse model. Phosphate-buffered saline was used as the vehicle control. Anti-human epidermal growth factor

receptor 2 (HER2) x cotinine complexed with cotinine-duocarmycin was used as a control antibody-drug conjugate (ADC); anti-HER2 scFv was derived from trastuzumab.

(B) Representative immunofluorescence images of whole-mounted retina stained with isolectin B4 (IB4, red) and neural/glial antigen 2 (NG2, green) to visualize the retinal vessels and pericytes. Scale bars on the top, middle, and bottom correspond to 500 μm, 100 μm, and 150 μm, respectively.

(C) Quantification of the avascular area and neovascular tuft area. All data were analyzed using NIH ImageJ software, and values are presented as percentages of the mean ± standard error of the mean (SEM) (n = 6 mice for each data set). $*P < 0.01$, $**P < 0.001$, obtained using one-way analysis of variance (ANOVA) and Tukey's post-hoc tests.

(D) Quantification of NG2 coverage of IB4 + vessels at the mid-peripheral region (pathological neovascular tuft area, left) and peripheral region (peripheral vascularized area, right), respectively in the whole-mounted retinas. Error bars represent SEM (n =6 mice for each data set). $**P < 0.001$, obtained using one-way ANOVA and Tukey's post-hoc tests.

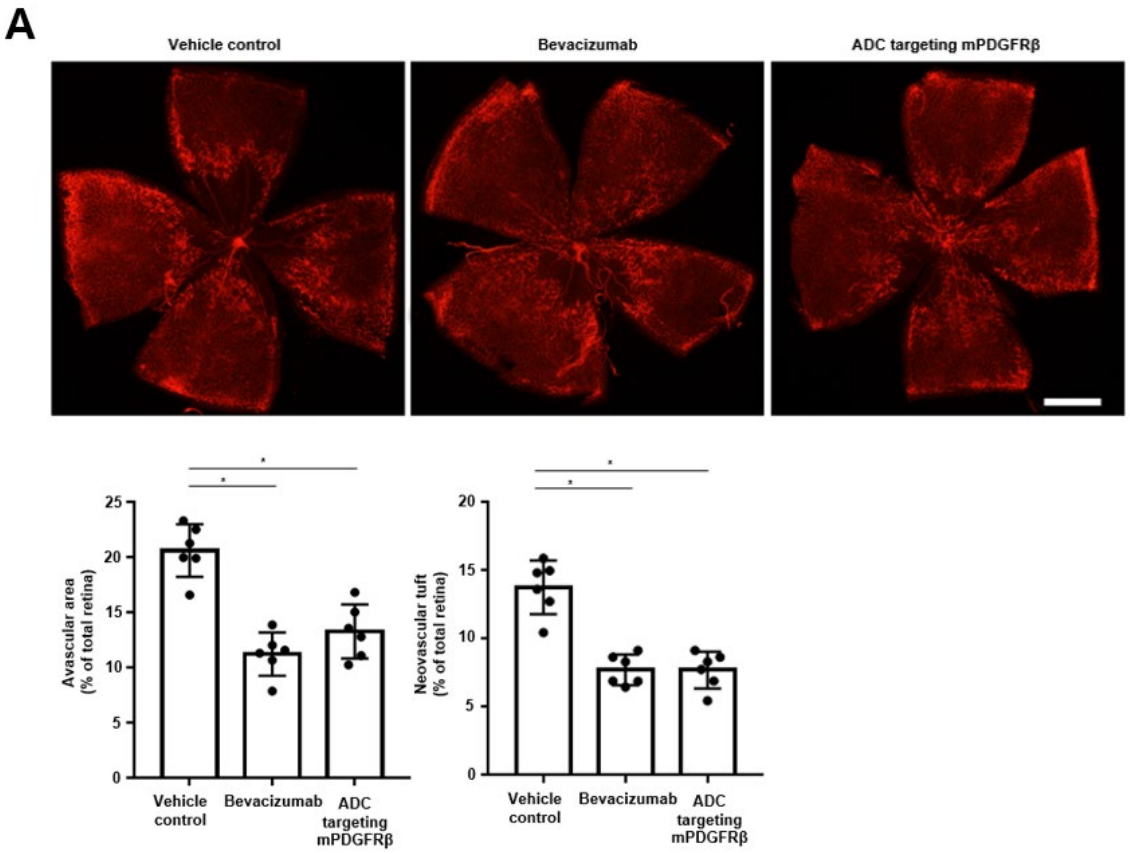

Figure 1.6. ADC targeting mPDGFRβ and bevacizumab treatment effectively reduce retinal neovascularization in OIR mouse model.

(A) Representative immunofluorescence images of whole-mounted retinas stained with isolectin B4 (IB4, red) to detect the retinal vessels. Scale bar, 500 μm. The avascular area and neovascular tuft area were quantified and presented as percentages of the total area of the retina. All data were analyzed using NIH ImageJ software, and values are presented as percentages of the mean ± standard error mean (SEM, n=6 mice for each group set). *P<0.01, obtained using one-way ANOVA and Tukey's post-hoc tests.

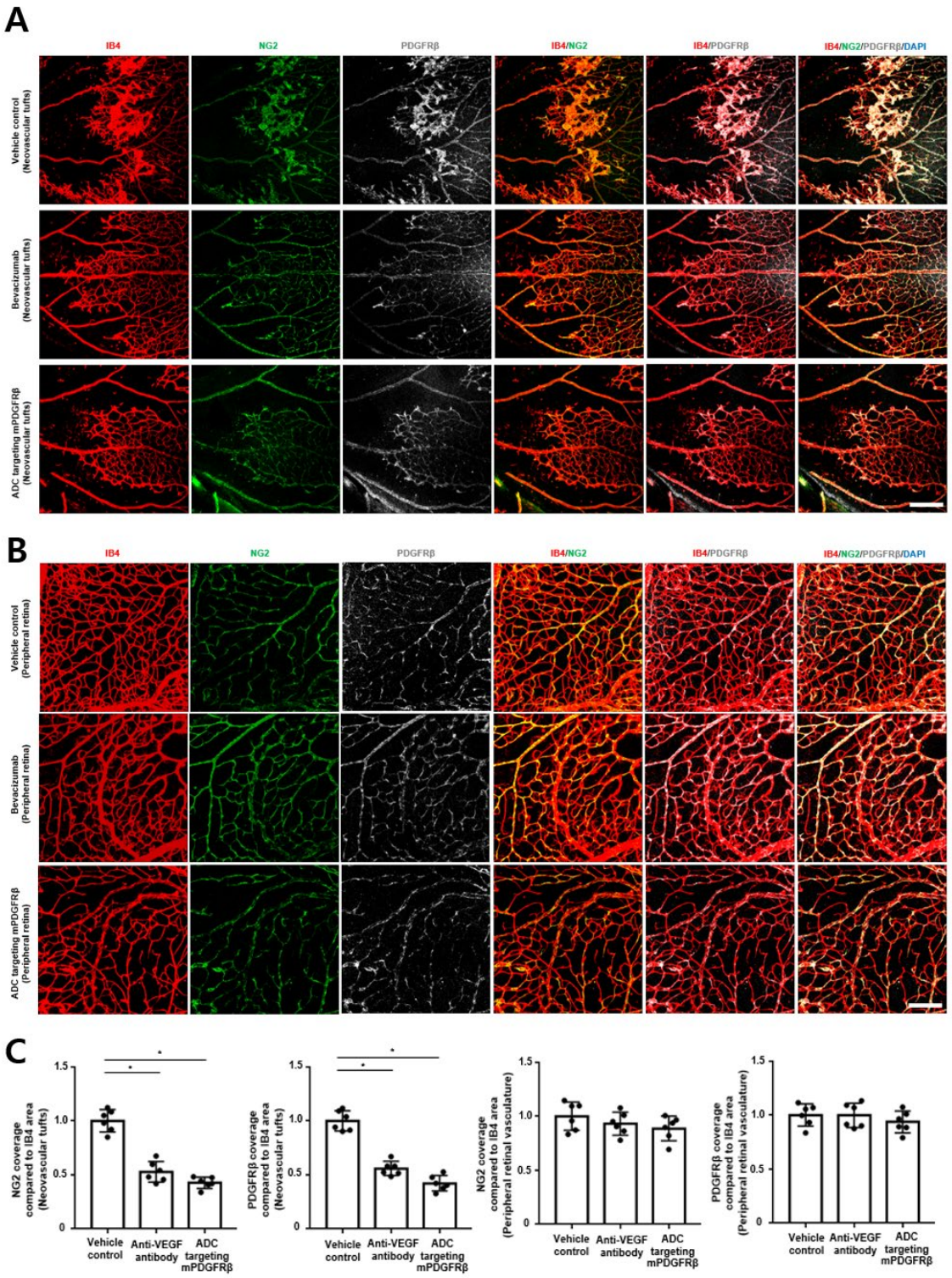

Figure 1.7. ADC targeting mPDGFRβ and bevacizumab treatment effectively reduce NG2^{+}PDGFR^{+} pericytes around retinal NV in OIR mouse model.

(A) Representative immunofluorescence images of the mid-peripheral region (pathological neovascular tuft area) stained with isolectin B4 (IB4, red), neural/glial antigen 2 (NG2, green), platelet-derived growth factor receptor β (PDGFRβ, gray). Scale bar, 200 μm.

(B) Representative immunofluorescence images of peripheral region (peripheral vascularized

area) stained with IB4, NG2, and PDGFRβ. Scale bar, 200 μm.

(C) Quantification of NG2 and PDGFRβ coverage of IB4+ vessels. Error bars represent SEM (n=6 mice for each group set).

ADC targeting mPDGFRβ does not induce anatomic or functional toxicity in the retina.

To figure out whether ADC targeting mPDGFRβ induces retinal anatomic toxicity, ADC (667.7 pg) was intravitreally injected into 6-week-old male wild-type C57BL6/J mice. PBS or control ADC was injected on the same day as the control groups. Seven days after injection, the eyeballs were enucleated and embedded in paraffin. Next, tissue sections were prepared and hematoxylin and eosin (H&E) stain and Terminal deoxynucleotidyl transferase dUTP nick end labeling (TUNEL) assay were performed. No significant differences were found in retinal thickness or number of apoptotic cells between the ADC group and the two control groups (Fig 1.8A).

To evaluate functional toxicity in the retina, we performed electroretinography (ERG) and OptoMotry test. No significant differences were detected in the not only amplitudes of scotopic and photopic ERG (Fig 1.8B and C) but also the spatial frequency of the sing-wave gratings in OptoMotry test (Fig 1.8D) between the ADC group and two control groups. These results suggest that ADC targeting mPDGFRβ does not induce anatomic or functional retinal toxicity. To further examine retinal vessel toxicity that could be induced by using ADC targeting mPDGFRβ, different doses of ADC targeting mPDGFRβ (dose range:667.7 pg ~ 333.85 ng per eye) were intravitreally injected into 6-week-old wild-type C57BL/6J male mice. ADC targeting mPDGFRβ treatment up to 1000 times higher dose of than therapeutic dose (66.77 pg/eye) in the OIR mouse model did not affect retinal integrity although ADC targeting mPDGFRβ treatment of 5000 times higher dose induced a significant reduction in the number of pericytes and inner blood-retinal barrier leakage (Figure 1.9 and 1.10).

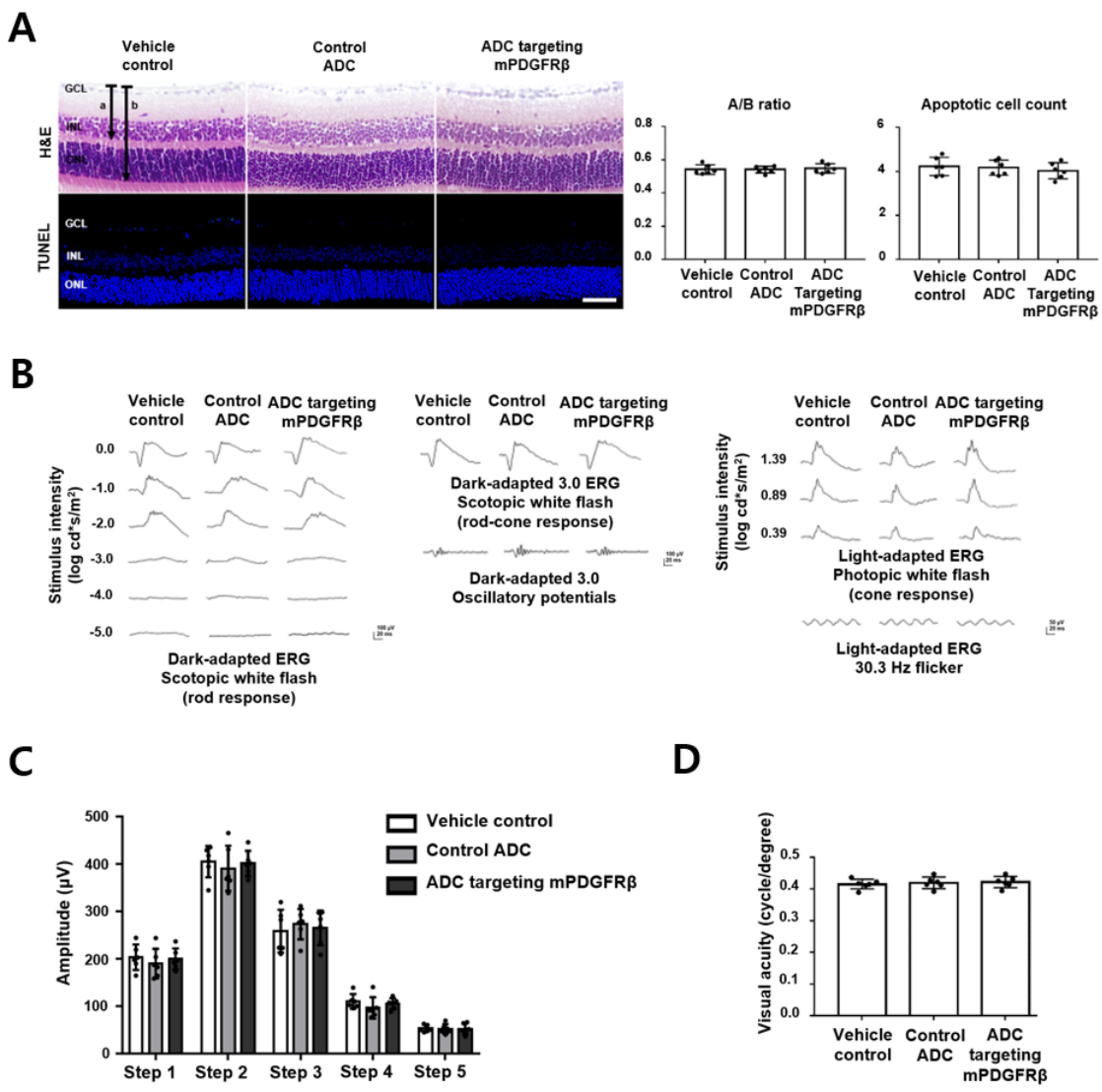

Figure 1.8. Retinal safety evaluation in mice receiving ADC targeting PDGFRβ.

(A) Representative hematoxylin and eosin (H&E) staining images and Terminal deoxynucleotidyl transferase dUTP nick end labeling (TUNEL) assay images of retinal tissues at seven days after injection of vehicle control, control antibody-drug conjugate (ADC), or ADC targeting mouse platelet-derived growth factor receptorβ (PDGFRβ). Scale bar, 500 μm. A/B ratio, the ratio of the thickness from internal limiting membrane to inner nuclear layer ("A") to that from internal limiting membrane to outer nuclear layer ("B"). Apoptotic cell count was determined at X200 magnification sectional images under a fluorescence microscope in five randomly selected fields in each slide. Each value represents the mean ± standard error mean (SEM, n = 6 mice per data set).

(B) The overall stimulus parameters used in this study of averaged dark-adapted and light-

adapted electroretinography (ERG) waveforms were as follows: step 1: scotopic white flash; step 2: scotopic white flash 3.0 cd·s/m2; and step 3: oscillatory potential, 3.0 cd·s/m2; step 4: photopic white flash; and step 5: 30.3 Hz flicker.

(C) Quantitative analyses of amplitudes of the b-wave by steps at seven days after injection of vehicle control, control ADC, or ADC targeting PDGFRβ in ERG test. Each value represents the mean ± SEM (n = 6 mice per data set).

(D) Quantitative analyses of visual acuity (spatial frequency thresholds, in cycle per degree) in OptoMotry test. Each value represents the mean ± SEM (n = 6 mice per data set).

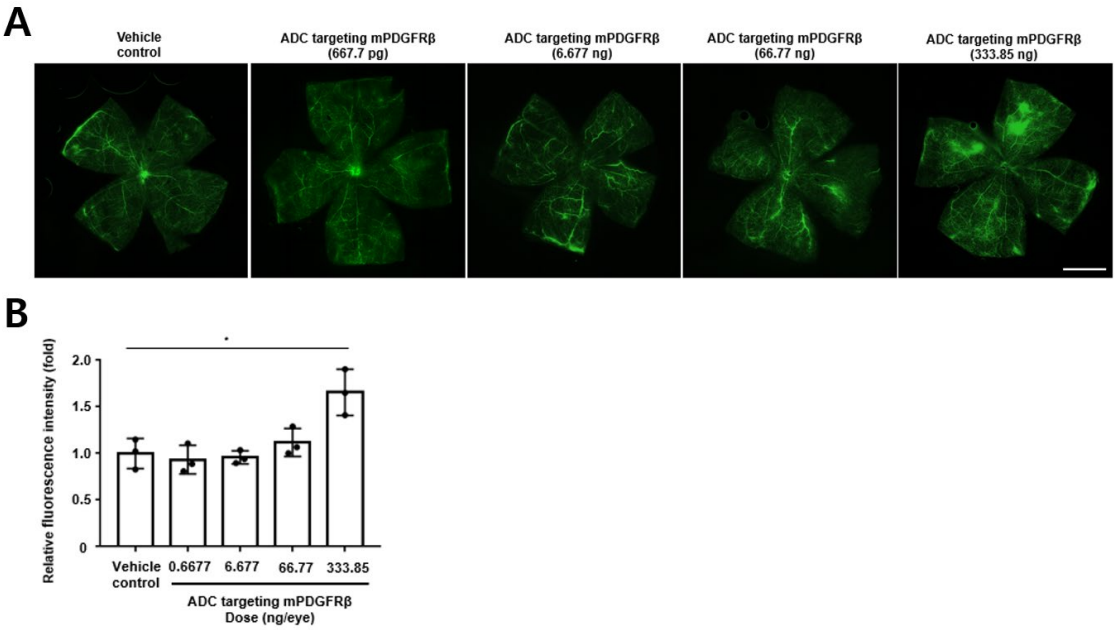

Figure 1.9. Evaluation of blood-retinal barrier leakage in mice receiving ADC targeting mPDGFRβ.

(A) Representative fluorescence images of retinas comparing fluorescein isothiocyanate (FITC)-dextran staining pattern as measurement of inner blood-retinal barrier leakage at seven days after injection of vehicle control, antibody-drug conjugate (ADC) targeting mouse platelet-derived growth factor receptorβ (PDGFRβ). Dose range: 667.7 pg ~ 333.85 ng per eye. Scale bar, 500 μm.

(B) Quantitative analyses of retinal vessel permeability by measuring the fluorescence intensities of FITC-dextran in retina samples. Each value represents the mean ± standard error mean (SEM, n=3 mice for each group set). *P<0.01, obtained using one-way ANOVA and Tukey's post-hoc tests.

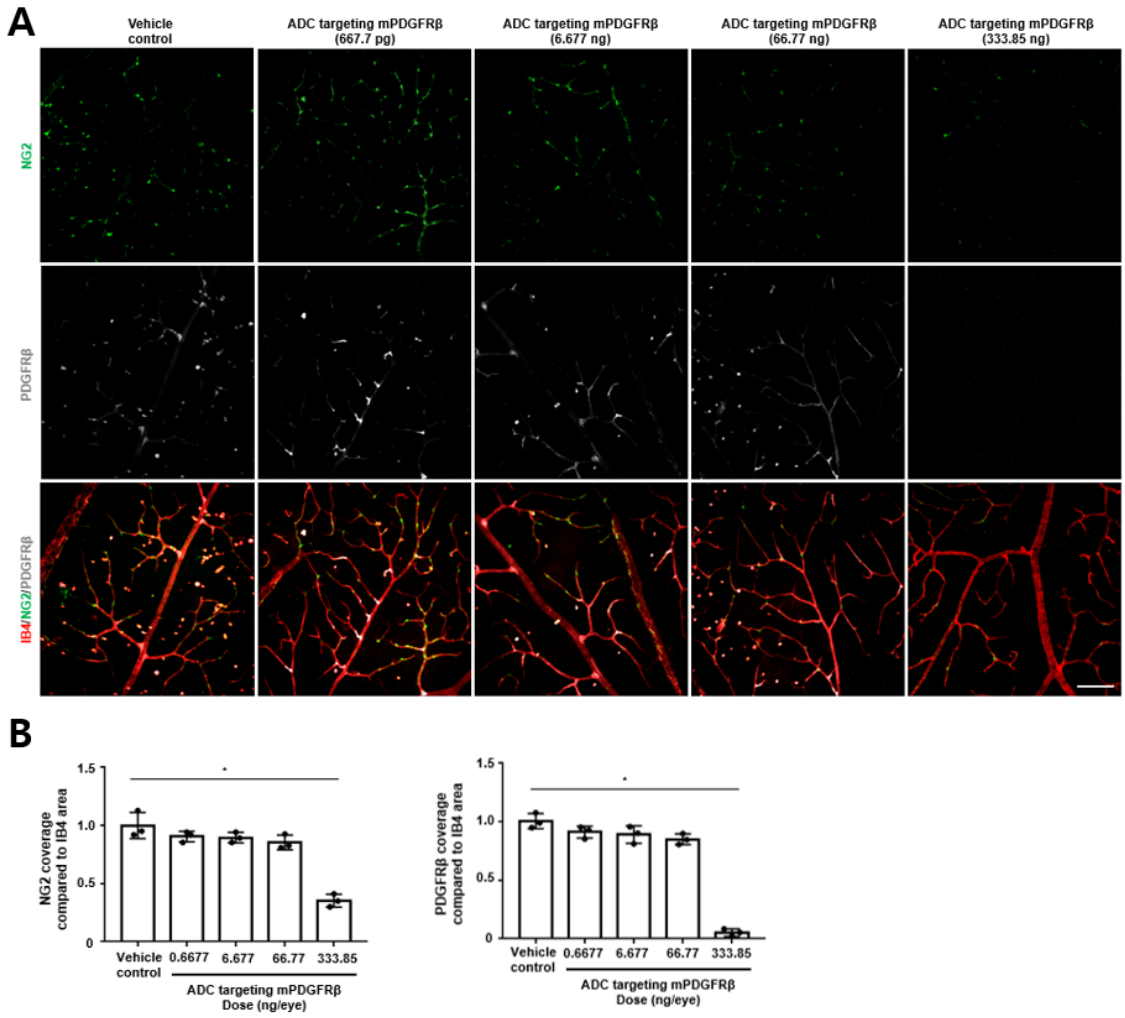

Figure 1.10. Evaluation of pericyte ablation in mice receiving ADC targeting mPDGFRβ.

(A) Representative immunofluorescence images of retina samples stained with anti-isolectin B4 (IB4, red), anti-neural/glial antigen 2 (NG2, green), PDGFRβ (gray) to visualize the retinal vessels and pericytes. Dose range: 667.7 pg ~ 333.85 ng per eye. Scale bar, 100 μm.

(B) Quantitative analyses of NG2 (top) and PDGFRβ (bottom) coverage of IB4+ vessels and values are presented as percentages of the mean ± standard error mean (SEM, n=3 mice for each group set). *P<0.01, obtained using one-way ANOVA and Tukey's post-hoc tests.

DISCUSSION

VEGF is critical for pathological angiogenesis and physiological retinal vascular development. VEGF is a major mediator of intraocular retinal NV and microvascular complications in retinal ischemia-related diseases, such as ROP, diabetic retinopathy, and retinal vascular occlusion (18, 112, 113). Anti-VEGF agents are standard therapeutics for targeting NV in ischemic retinopathy (114). Although the current standard treatment option for ROP is laser ablation of the peripheral avascular retina (91, 115), intravitreal anti-VEGF treatment has drawn attention in recent years and has shown an effect on the inhibition of retinal NV and extension of physiologic retinal vascularization of the previous avascular retina (115, 116). Despite the promising outcomes of anti-VEGF treatment in ROP, there are still concerns about anti-VEGF therapy, including a lack of information about the effect on physiologic vascular angiogenesis of other organs in developing preterm infants and increased reactivation rate of ROP compared with other treatment options (27, 38, 40, 103). Therefore, there is still an unmet need for the development of novel therapeutics to suppress ocular NV in ROP. In this study, we demonstrated that an ADC targeting PDGFRβ selectively ablates PDGFRβ-expressing pericytes and inhibits pathologic retinal NV in an OIR mouse model, the most widely used animal model of ROP.

During vascular development, endothelial cells release PDGF-BB, most of which binds to PDGFRβ in perivascular cells (106). PDGF-BB facilitates vessel maturation by promoting pericyte recruitment and supporting pericyte-endothelial interactions. Pericyte recruitment is dependent on PDGF-BB/PDGFRβ signaling. In the absence of PDGF-BB or PDGFRβ, near-complete loss of pericytes is observed in organs, such as those in the central nervous system (117). Pericytes directly contact the vascular endothelial cells and share a common basement membrane (118). This biological trait provides extra stability to the vascular endothelial cells and prevents vascular leakage. It has been known that the period of VEGF dependence corresponds to the period followed new vessels acquire a pericyte coating (119, 120). Pericytes also secrete VEGF and other cell survival factors to protect the vascular endothelial cells (121). These protective functions of pericytes on endothelial cells could also render the reactivation of retinal NV resistant to anti-VEGF therapy in ROP.

Physiological retinal vascularization after preterm birth probably depends on the timing and availability of pro- and anti-angiogenic factors. This idea is supported by findings in neonates (122) with and without ROP and in rats (123) with different ratios of pro-angiogenic VEGF and anti-angiogenic pigment epithelial-derived factor. It has been reported that intraocular levels of PDGF-BB are upregulated in the OIR mouse model and there is excessive coverage of PDGFRβ-positive cells in the NV region in OIR mice (124).

Preclinical studies have been conducted to suppress intraocular pathologic NV by inhibiting intraocular PDGF or PDGFRβ, targeting pro-angiogenic activity of pericytes (125, 126). However, none of these agents are currently available in clinical settings, demonstrating no visual or anatomic advantages (127). Therefore, we considered the use of ADC that directly target PDGFRβ-expressing pericytes and selectively induce cell death as an alternative therapeutic strategy. As sufficient target molecules should be preferentially present on the target cell surface, compared with the non-target cell surface, ADC should be effective and non-toxic (128, 129). In our experiment, PDGFRβ was significantly overexpressed in retinal NV compared to the control retina in the OIR model (Fig. 1.1).

Based on this observation, we hypothesized that ADC targeting PDGFRβ might induce cytotoxicity specifically toward pericytes of neovessels and inhibit retinal NV. We found that the cotinine-duocarmycin conjugate was the most potent and that drug-to-antibody ratio (DAR) 4 cotinine-cytotoxic drugs were more potent than DAR 1 cotinine-cytotoxic drugs (Fig. 1.2). Furthermore, duocarmycin is hydrophilic, minimizes the bystander effect and hence has fewer nonspecific off-target effects (130). For these reasons, we used only cotinine-duocarmycin for detailed studies. In the current study, we first confirmed that ADC targeting mPDGFRβ efficiently killed MBVP cells, and verified that its internalization and cytotoxicity were not affected by the presence of PDGF-BB in an in vitro setting (Fig. 1.4). We then established an OIR mouse model and showed that ADC targeting mPDGFRβ remarkably promoted retinal revascularization in the previous avascular area and inhibited retinal NV (Fig. 1.5-1.6).

Under the ischemic retinal conditions of OIR, neovascular tufts covered by pericytes grow toward the vitreous body (124, 131, 132). In our study, both bevacizumab and ADC targeting mPDGFRβ treatment significantly reduced NG2- and PDGFRβ positive area

compared to vehicle control at the boundary between the vascular and avascular areas of the retina, whereas there were no differences of NG2 and PDGFRβ positive area at the peripheral vascularized retina. We considered that pericytes in the neovascular tufts are more vulnerable than pericytes in the peripheral retinal vasculature from these data (Fig. 1.7). This result is likely due to overexpression of PDGFRβ of the pericytes in the neovascular tufts than pericytes in the peripheral retinal vasculature, increasing efficiency of ADC targeting mPDGFRβ. In another study, pericyte-specific deletion of CCN1, an extracellular matrix protein, during angiogenesis under ischemic conditions results in reduced neovascular tufts and increased revascularization (131). Another group reported that NCK1/2 signaling downstream of PDGFRβ in pericytes was related to OIR progression, and its inhibition suppressed pericyte recruitment to the tip cells, preventing neovascular tuft formation and promoting revascularization (124). These findings suggest an important role of pericytes in the progression of normal angiogenesis, as well as in the regression of neovascularization in OIR.

Immunohistochemical experiments showed a marked difference in expression levels of PDGFRβ between normal retinal vessels and neovessels (Fig. 1.1), which would limit the toxicity of ADC targeting mPDGFRβ toward normal retinal vessels. This lack of toxicity by ADC targeting mPDGFRβ was confirmed in both anatomic and functional aspects. The retinal layer thickness ratio was not changed, and TUNEL assays were negative (Fig. 1.8A). The results of ERG and the OptoMotry test were also normal (Fig. 1.8B-D). To further evaluate retinal vessel toxicity, intravitreal injection of different doses of ADC targeting mPDGFRβ (dose range: 667.7 pg ~ 333.85 ng per eye) was administered to 6-week-old wild-type C57BL/6J male mice. Although treatment of ADC targeting mPDGFRβ up to 1000 times higher dose than the therapeutic dose in the OIR model did not affect retinal integrity, treatment of ADC targeting mPDGFRβ of 5000 times higher dose induced a significant reduction in the number of pericytes and inner blood-retinal barrier leakage (Fig. 1.9). There has been reported that a sudden reduction of pericytes from stabilized vessels is not sufficient to disrupt the integrity of retinal vessels (133); limited toxicity toward pericytes in normal vessels could be endured without causing pathologic changes in the retina. According to our toxicity test by different doses of ADC, we require meticulous evaluation to minimize the potential retinal

vessel toxicity when determining the optimal dose of ADC targeting mPDGFRβ for clinical trials. Since the ADC was not purified after the conjugation, an unpurified payload could have contributed to the non-specific killing. However, considering systemic toxicity, the risk would be very minimal because the amount of ADC administered is quite limited, and the ADC is injected locally via the intravitreal route. In our experiments, mice injected with ADC targeting mPDGFRβ showed no behavioral change or weight loss.

In conclusion, the removal of PDGFRβ-overexpressing pericytes in neovessels with ADC effectively suppressed pathologic ocular NV in an OIR mouse model. At therapeutic doses, ADC targeting PDGFRβ did not induce morphological or functional abnormalities in the retina or cause systemic toxicity. We believe that ADC targeting PDGFRβ could be a therapeutic option for ocular NV.

CHAPTER 1-2

Regulation of Retinal Vascular Abnormalities in Diabetic Retinopathy via Intravitreal IL-10 Injection

INTRODUCTION

Diabetic macular edema (DME), a complication of diabetic retinopathy (DR), can occur at any stage of DR and is caused by uncontrolled leakage of vascular fluid, proteins, and lipids, leading to structural and functional damage to the retina, further resulting in visual impairment (134).

The inner and outer blood-retinal barrier (BRB), formed by tight junction complexes of vascular endothelial cells and retinal pigment epithelium (RPE), respectively, contributes to the control of fluid entry and exit to the retina from retinal and choroidal vessels and maintains ocular immune privilege by preventing immune cells from entering the retinal tissue under physiological conditions (134, 135). Therefore, inner and outer BRB disruption is considered an important phenomenon in the pathogenesis of DME, resulting in fluid accumulation and recruitment of inflammatory cells to the retina. For several decades, most studies on DME pathogenesis have focused on microvascular leakage induced by inner BRB disruption through damage to neurovascular unit composed of vascular endothelial cells, pericytes, astrocytes, and Müller cells (136-141). Although outer BRB disruption has received less attention than inner BRB disruption, the contribution of the outer BRB to DME cannot be overlooked, considering that the accumulated retinal fluid in DME is a mixture of leakages from both inner and outer BRB disruptions (142, 143). Furthermore, there is evidence of tight junctional barrier breakdown of the RPE as well as fluid leakage through the paracellular space to the retina both diabetic animal models (144-147) and patients (6, 148, 149).

Among the possible mechanisms regarding hyperglycemia-induced outer BRB breakdown, we and others have revealed that microglia/macrophages could be an early driver for neuroinflammation, considering its pivotal role in the repair of damaged tissue through secretion of various cytokines, chemokines, and growth factors that can affect junctional complexes of RPE (62, 150-152). Furthermore, activated microglia in the retina and recruited macrophages from retinal and choroidal vessels have migrated and accumulated in the RPE (62, 153) and shown an imbalance in the pro-inflammatory (M1-like microglia/macrophage) and anti-inflammatory phenotypes (M2-like microglia/macrophages) during DR progression (154), suggesting that microglia/macrophage activation and alteration of its dynamics of polarization could affect junctional complexes of the RPE. However, it is still unknown whether

modulation of the polarization phenotype of microglia/macrophages during DR has a protective effect against BRB disruption and vascular leakage associated with DR progression.

In the current study, we investigated whether the interaction between the RPE and macrophages affects outer BRB disruption under high glucose conditions and whether modulation of macrophage polarization switching from M1 to M2 suppresses outer BRB breakdown. High glucose treatment directly induces tight junction disruption in RPE cells and the pro-inflammatory state of macrophages. Alteration of macrophage polarity significantly influenced tight junction expression in RPE cells under high glucose conditions *in vitro*. Furthermore, we found that recruited microlgia/macrophages to the retina under hyperglycemia changed their polarity to a pro-inflammatory state along with outer BRB disruption in the early period of the streptozotocin (STZ)-induced diabetic mouse model. Using this mouse model, we confirmed that modulation of macrophage polarization by treatment with IL-10, a representative M2 inducer, effectively reduced the M1/M2 macrophage polarization ratio in the RPE, inhibited outer BRB disruption and fluid leakage and ameliorated the downregulation of junctional complexes of RPE. These results suggest that the regulation of microglia/macrophage polarization could be a potential therapeutic strategy to control outer BRB disruption and fluid leakage to the retina in DME.

MATERIALS AND METHODS

1. Cell culture

The adult retinal pigment epithelial cell line-19 (ARPE-19) cells were obtained from American Type Cell Culture (ATCC; CRL2302). Cells in the control group were maintained in DMEM/F-12 medium (a mixture of Dulbecco's Modified Eagle Medium [#11966025, Gibco, Thermo Fisher Scientific] and Ham's F-12 Nutrient Mix [#11765047, Gibco, Thermo Fisher Scientific]) with a normal glucose concentration (NG, 5 mM D-glucose) that was supplemented with 10% of fetal bovine serum (FBS, #16000044, Gibco, Thermo Fisher Scientific), 1% penicillin-streptomycin (#15140122, Gibco, Thermo Fisher Scientific) in a humidified 5% CO2 incubator at 37°C. Cultured APRE-19 cells in experimental group were treated with a high glucose medium (HG, 25 mM D-glucose). The human monocytic leukemia cells, THP-1, were purchased from Korean Cell Line Bank and maintained in RPMI 1640 medium (#11879020, Gibco, Thermo Fisher Scientific) with a NG concentration containing 10% FBS, 1% penicillin-streptomycin (#15140122, Gibco, Thermo Fisher Scientific) in a humidified 5% CO2 incubator at 37°C. Differentiation of THP-1 cells into M0 macrophages was performed by incubating the cells with 10 ng/mL phobol 12-myristate 13-acetate (PMA, #P8139, Sigma-Aldrich) for 24 hours and then resting for 5 days incubated with the PMA-free medium. Macrophages were polarized into M1 macrophages by incubating the cells with 10 ng/mL PMA containing media for 24 hours and then resting for 72 hours incubated with the PMA-free medium before exposing the primed cells to 20 ng/ml of IFN-γ (#285-IF, R&D systems) and 20 ng/ml of lipopolysaccharides (LPS, #L2630, Sigma-Aldrich) containing media for 48 hr. Macrophages were polarized into M2 macrophages by incubating the cells with 10 ng/mL PMA containing media for 24 hours and then resting for 72 hours incubated with the PMA-free medium before exposing the primed cells to 20 ng/ml of IL-4 (#204-IL, R&D systems) and 20 ng/ml of IL-10 (#217-IL, R&D systems) containing media for 48 hours. The condition for macrophage differentiation and polarization was mainly referenced by the papers (155, 156). The differentiated M0/M1/M2 macrophages were cultured in NG or or HG medium.

2. Immunocytochemistry

The APRE-19 cells monolayers were fixed with 4% paraformaldehyde (PFA, #P2031; Biosesang, Seongnam, Gyeonggi-do, Korea) for 10 min and permeabilized in 0.1% Triton X-100. The cells were incubated with anti-ZO-1 antibody (1:200, #61-7300, Invitrogen), anti-occludin antibody (1:200, #33-1500, Abcam) followed by incubation with Alexa Fluor 488- and 594-labeled secondary antibodies (1:400, #A-21202, #A-21207, Invitrogen). The nuclei were stained using 0.1 μg/mL 4'6-diamidino-2-phenylindole (DAPI; #D9542, Invitrogen).

3. Quantitative real-time polymerase chain reaction (qRT-PCR)

Total RNA was extracted using the TRIzol™ reagent (#15596018, Invitrogen). Isolated RNA (1 μg) was reverse transcribed using the High-Capacity RNA-to-cDNA kit (#4387406, Applied Biosystems). qRT-PCR assays were performed in qPCR Master Mix for Power SYBR® Green PCR Master Mix (#4367659, Applied Biosystems) using real-time PCR (Step one plus, Applied Biosystems) and the following primer pairs: human *IFN-γ*, 5'-GAGTGTGGAGACC A TCAAGGAAG-3' (forward) and 5'-TGCTTTGCGTTGGACATTCAAGT C-3' (reverse); human *NFκB*, 5'-GCAGCACTACTTCTTGACCACC-3' (forward) and 5'-TCTGCTCC TGAGCATTGACGTC-3' (reverse); mouse *NFκB,* 5'-GCTGCCAAAGAAGGACACGACA-3' (forward) and 5'-GGCAGGCTATTGCTCATCACAG-3' (reverse); human *IL-10*, 5'-TCTCC GAGATGCCTTCAGCAGA-3' (forward) and 5'-TCAGACAAGGCTTGGCAACCCA-3' (reverse); mouse *IL-10*, 5'-CGGGAAGA CAATAACTGCACCC-3' (forward) and 5'-CGGTTAGCAGTATGTTGTCCAGC-3' (reverse); human *IL-13*, 5'-ACGGTCATTGCTC TCACTTGCC-3' (forward) and 5'-CTGTCAGGTTGATGCTCCATACC-3' (reverse); human *TNF-α*, 5'-CTCTTCTGCCTGCTGCACTTTG-3' (forward) and 5'-ATGGGCTACAGG CTTGTCACTC-3' (reverse); mouse *TNF-α,* 5'-GGTGCCTATGTCTCAGCCTC TT-3' (forward) and 5'-GCCATAGAACTGATGAGAGGGAG-3' (reverse); human *IL-6*, 5'-AGACAGCCACTCACCTCTTCAG-3' (forward) and 5'-ATGGGCTA CAGGCTTGTCACT C-3' (reverse); human *IL-1β*, 5'-ACCTGCTGGTGTGTGA C GTT-3' (forward) and 5'-TCGTTGCTTGGTTCTCCTTG-3' (reverse); human *iNOS*, 5'-GCTCTACACCTCCAATGT GACC-3' (forward) and 5'-CTGCCGAGA TTTGAGCCTCATG-3' (reverse); human *Arg-1*,

5’-TAACCTTGGCTTGCTTC GG-3’ (forward) and 5’-GTGGCGCATTCACAGTCAC-3’ (reverse); *GAPDH*, 5’-GTCTCCTCTGACTTCAACAGCG-3’ (forward) and 5’-ACCACCCTGTTGCTG TAGCCAA-3’ (reverse). The target mRNA expression levels were analyzed using the ΔΔCt method and normalized to expression levels of GAPDH, used as an internal control.

4. Western blot analysis

The ARPE-19 cells and THP-1 cells were lysed in a lysis buffer containing 20 mM Tris (pH 7.5), 150 mM NaCl, 1% Triton X-100, and phosphatase inhibitor and protease inhibitor cocktail. For mouse RPE preparation, RPE tissues isolated from enucleated eyes were put into microcentrifuge tubes and homogenized in the lysis buffer. The RPE lysates were centrifuged to clear debris, and the supernatant was used for the experiment. The lysates of the cells and RPEs were separated on 6-10% SDS-PAGE gels for 2 hours and were transferred to nitrocellulose membranes for 1 hour. After blocking in 5% of BSA in TBST for 30 minutes, the membranes were incubated overnight at 4°C with primary antibodies for anti-ZO-1 antibody (1:1000, #8193, Cell Signaling Technology), anti-occludin antibody (1:1000, #91131, Cell Signaling Technology), anti-β-actin antibody (1:2000, #93668, Cell Signaling Technology). Anti-rabbit IgG-HRP conjugate (1:5000, #7074, Cell Signaling Technology), and anti-mouse IgG-HRP conjugate (1:5000, #7076, Cell Signaling Technology) were used as secondary antibodies for 2 hours at room temperature (RT). The membranes were incubated with Enhanced Chemiluminescent Detection substrate (#34578, Thermo Fisher Scientific) and exposed to film in ImageQuant LAS 4000 (GE Healthcare Life Sciences). The band density was analyzed with Multi-Gauge software v.2.3 (Olympus), and the densities were quantified as the ratio of the corresponding control densities.

5. Trans-epithelial permeability assay and trans-epithelial electrical resistance measurement

The APRE-19 cells were seeded on transwell filters (6.5-mm diameter, 0.4-μm pore, #3470, Cornig Inc.) coated with laminin. After confluency was achieved, the monolayer was

maintained in DMEM/F12 with a normal glucose concentration (NG, 5 mM D-glucose) containing 1% FBS to induce polarization. Monolayers incubated more than 2 weeks were utilized for the analysis for barrier function. ARPE-19 cells were cultured in NG (5 mM glucose) or HG (25 mM glucose) and/or co-incubated with differently polarized M0/M1/M2 THP-1 cells for 2 days Then, trans-epithelial permeability assay and trans-epithelial electrical resistance measurement were conducted. To evaluate trans-epithelial permeabilization, transwell inserts containing ARPE-19 cells were transferred to a new multi-well plate and add 500 μL phenol red-free MEM to basolateral compartment. The media of apical compartment was aspirated and replaced with 100 μL (1 mg/ml) Evans blue dye suspension with protection from light for 1 hour at room temperature. Evans blue suspension at basolateral media was collected in 1.5 mL Eppendorf tubes and vortexed. After that, 100 μL alliquots from each Eppendorf tube containing Evans blue basolateral media or phenol-red free MEM serve as the blank control were transferred to 96-well clear bottom black polystyrene microplates (#3603, Cornig Inc.) in triplicate. The fluorescence intensity was measured 620 nm using a microplate reader (BioTek, Epoch2). The trans-epithelial electrical resistance (TEER) was measured with an epithelial voltohmmeter, EVOM3, (World Precision Instruments). The value of each individual transwell was calculated by subtracting the value of a blank (laminin-coated transwell without cells) from the experimental value. Resistance values for each transwell were normalized as the ratio of measured resistance at each time point to baseline resistance.

6. Flow Cytometry

The THP-1 cells were stained with PE anti-CD11b (#555388, BD Biosciences), FITC anti-CD64 (#560970, BD Biosciences), Alexa Fluor 647 anti-CD163 (#562669, BD Biosciences), PE-anti-CD14 (#562691, BD Biosciences), PE-Cy7 anti-CD68 (#565595, BD Biosciences) antibodies at 4°C for 1 hour. The stained cells were assayed for fluorescence using a BD Accuri^{TM} C6 cytometer (Becton, Dickinson and Company). The data were analyzed using the FlowJo program (Tree Star).

7. Enzyme-linked immunosorbent assay (ELISA)

The cell-free medium was collected from the co-culture of APRE-19 cells and differentiated M0/M1/M2 macrophages after centrifugation. Cytokine secretion in the co-culture medium was assayed using an ELISA kit according to the procedure recommended by the supplier (TNF-α [#DTA00D, R&D systems], IL-10 [#D1000B , R&D systems]). The minimum protein levels of detection calculated from the standard curves were as follows: 15.6 pg/mL for TNF-α and 31.2 pg/mL for IL-10.

8. Mice

All animal procedures were approved by the Seoul National University Animal Care and Use Committee (Permit Number: SNU-200527-1-2) and were conducted following the guidelines of the Association for Research in Vision and Ophthalmology Statement for the use of Animals in Ophthalmic and Vision Research. Seven-week-old, pathogen-free male C57BL/6J mice were allocated into experimental groups. After an 8-h fast, diabetes was induced by single intraperitoneal injection of freshly prepared streptozotocin (STZ, #S-0130, Sigma-Aldrich) at a concentration of 180 mg/kg body weight in 10 mmol/L citrate buffer (pH 4.5). Age-matched controls received citrate buffer only. Mice with blood glucose levels > 300 mg/dL 4 days after STZ injection were deemed diabetic. Glucose levels and body weight were monitored consecutively before mice were sacrificed. The total number of mice used in each experiment was determined based on the preliminary result of the streptozotocin-induced diabetic mouse model. No statistical methods were used to predetermine sample size.

9. Intravitreal injection

The mice were fully anesthetized by intraperitoneal injection using the mixture (3:1 ratio, 1 mL/kg) of the zolazepam and tiletamine (Zoletil 50, Virbac) and xylazine (Rompun, Bayer Korea) and pupils were dilated with tropicamide 1% (Tropherin, Hanmi. Pharm Co. Ltd.). Then, microliter syringe with 33-gauge blunt needle (Hamilton Bonaduz AG) was inserted into the vitreous cavity with a 60° injection angle for the eye followed by gently loading IL-6 (20 ng/eye) and IL-10 (50 ng/eye) under the surgical microscope (Leica Microsystems, Ltd.). Age-matched controls were injected with citrate buffer only.

10. Immunofluorescence

The eyes were enucleated and fixed with 4% PFA for 15 min at room temperature. After washing with PBS, the eyes were dissected to remove all components except the retina and RPE-choroid-scleral (RCS) complexes. The retina and RCS complexes were whole mounted and incubated in Perm/Block solution (0.2% Triton X-100 and 0.3% BSA in PBS) at room temperature for 1 hour. Next, the samples were incubated overnight at 4 °C with anti Iba-1 antibody (1:200, #MA5-27726, Invitrogen), anti-iNOS antibody (1:200, #PA3-030A, Invitrogen), anti-Arg-1 antibody (1:200, #NB-100-59740, Novus Biologicals). After washing with PBS, the samples were incubated at room temperature for 2 hours with Alexa Fluor 350-labeled donkey anti-rabbit IgG antibody (1:400; #A10039; Invitrogen), Alexa Fluor 488-labeled donkey anti-mouse IgG antibody (1:400; #A21202; Invitrogen), Alexa Fluor 594-labeled donkey anti-rabbit IgG antibody (1:400; #A21207; Invitrogen), Alexa Fluor 647-labeled donkey anti-goat IgG antibody (1:400; #A21447; Invitrogen), and Alexa Fluor 594-conjugated anti-ZO-1 antibody (1:250; #339194, Invitrogen).. After washing with PBS, the samples were counterstained with 10 mg/ ml of DAPI (1:1000; #D9542; Sigma-Aldrich) at room temperature for 15 minutes. After washing with PBS, the retina and RCS complexes were mounted with Fluoromount™ Aqueous Mounting Medium (#F4680, Sigma-Aldrich) and observed under a confocal microscope (Leica TCS STED; Leica Microsystems Ltd.).

11. Immunohistochemistry on cryostat ocular sections

Immunohistochemistry analysis was performed using frozen retinal sections. Briefly, sections were fixed in 4% PFA at 4°C for 10 minutes. To permeabilize the tissue, the sections were incubated in 0.1% Triton-X100 for 15 minutes at room temperature and blocked with 2% FBS for 15 minutes at room temperature. Next, the samples were incubated overnight at 4°C with anti F4/80 antibody (1:400, #MF-48000, Invitrogen), anti-Iba-1 antibody (1:200, #MA5-27726, Invitrogen), anti-iNOS antibody (1:400, #PA3-030A, Invitrogen), anti-Arg-1 antibody (1:400, #NB-100-59740, Novus Biologicals), After washing with PBS, the samples were incubated at room temperature for 2 hours with Alexa Fluor 488-labeled donkey anti-mouse IgG antibody (1:400; #A21202; Invitrogen), Alexa Fluor 594-labeled donkey anti-rabbit IgG antibody (1:400;

#A21207; Invitrogen), Alexa Fluor 647-labeled donkey anti-goat IgG antibody (1:500; #A21447; Invitrogen). After washing with PBS, the samples were counterstained with 10 mg/ml of DAPI (1:1000; #D9542; Sigma-Aldrich) at room temperature for 15 minutes. After washing with PBS, slides were mounted with Fluoromount™ Aqueous Mounting Medium (#F4680, Sigma-Aldrich) and observed under a confocal microscope (Leica TCS STED; Leica Microsystems Ltd.).

12. Analysis of outer blood-retinal barrier leakage with FITC-Dextran

To investigate the inner and outer blood-retinal barrier leakage, fluorescence-labeled dextran (60 kDa, 100 mg/kg, #FD70S; Sigma-Aldrich) was injected into the left ventricle of each mouse while anesthetized, 1 hour before the sacrifice and the enucleated eyes were immediately frozen and embedded in optimal cutting temperature (OCT) compound (Tissue-Tek) for cryosection. Serial sections (5 μm) of whole eyes were cut sagittally. The area for outer BRB-specific leakage was defined as the total pixels between the external limiting membrane and the outer board of the leakage (retinal pigment epithelium) and observed under a fluorescence microscope. Area quantification was performed using ImageJ 1.42 software (National Institutes of Health, Bethesda, MD, USA)

13. Statistics and reproducibility

Statistical analyses were performed using SPSS software version 22.0 (SPSS Inc., Chicago, IL, USA) and GraphPad Prism v.8.0.1. The experimental data were presented as mean ± standard error of the mean. *P* values were determined using one-way ANOVA and Tukey post-hoc tests for multiple groups. All the data in our manuscript were repeated at least three times independently with similar results. Differences were considered statistically significant at $P < 0.05$.

RESULTS

High glucose induces tight junction disruption and secretomal change of APRE-19 cells.

High glucose treatment has been well known to induce structural and functional changes in cells constituting the inner blood retinal barrier (BRB) such as vascular endothelial cells, pericytes, and glial cells (139-141, 157, 158). Thus, we investigated whether the high glucose treatment also affects structural change of retinal pigment epithelium (RPE) constituting the outer BRB. We set out to determine the expression and localization of the tight junction proteins in the adult retinal pigment epithelial cell line-19 (ARPE-19) cells by immunofluorescence staining and western blotting under normal glucose (5 mM) and high glucose (25 mM) conditions. The high glucose treatment induces downregulation of the tight junction complexes of APRE-19 cells, demonstrated by immunopositivity and protein level of ZO-1 and occludin, which are the major components of tight junction complexes constituting the outer BRB (Figure 1.11A). High glucose treatment significantly reduced the protein levels of ZO-1 and occludin from 48 hours after treatment (Figure 1.11B). To address whether high glucose influences the functional integrity of outer BRB, we additionally examined the ARPE-19 cell monolayer integrity using trans-epithelial permeability assay and trans-epithelial electrical resistance (TEER) measurement. High glucose treatment significantly increased trans-epithelial permeability and decreased TEER from 2 days after treatment (Figure 1.12).

Considering the RPE secretes various cytokines and growth factors both in the physiological and pathological environment (159, 160), we examined the secretomal change of APRE-19 cells which can affect structural and functional integrity of RPE. We incubated ARPE-19 cells under normal and high glucose medium for 24, 48, and 72 hours and evaluated the mRNA levels of *IFN-γ*, *NFκB*, *IL-10*, *IL-13*, *TNF-α*, *IL-6*, *IL-1β* which are previously reported as representative cytokines related to outer BRB breakdown and microglia (retina-resident macrophages)/macrophage polarization (6, 161). High glucose treatment significantly upregulated *IFN-γ*, *NFκB*, *IL-10*, *IL-13*, *TNF-α*, *IL-6*, and *IL-1β* mRNAs compared to normal glucose (Fig. 1.13), which means seretomoal change of RPE in response to high glucose could affect tight junction integrity of RPE and microglia/macrophages polarization under hyperglycemia-induced inflammatory environment. Taken together, these results suggest that

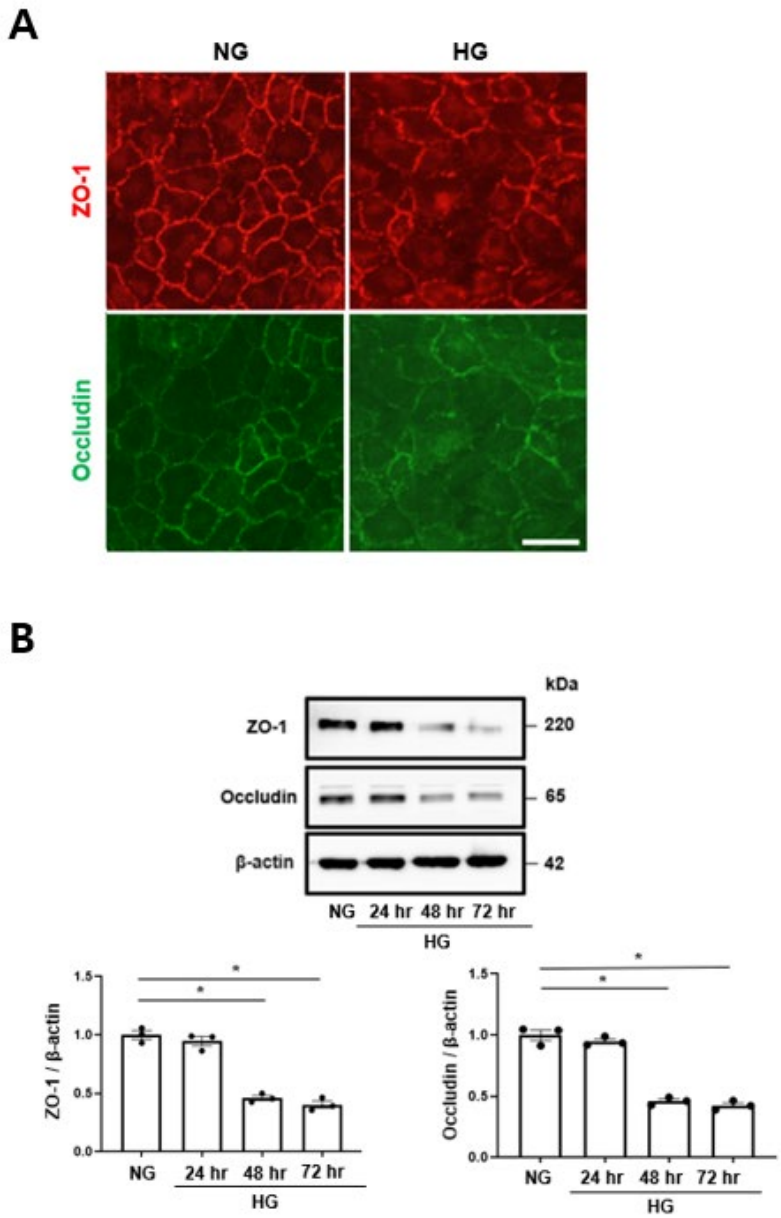

Figure 1.11. High glucose induces tight junction disruption of ARPE-19 cells.

(A) Representative immunofluorescence images stained with anti-zonula occludens-1 (ZO-1, red), anti-occludin (green) in adult retinal pigment epithelial cell line-19 (ARPE-19) cells after 48 hours of normal glucose (5 mM) and high glucose (25 mM) treatment. Scale bar = 20 μm.

(B) Representative western blot data showing the expression of ZO-1, occludin and beta-actin (β-actin) after treating normal glucose (5 mM) and high glucose (25 mM) for 24, 48, 72 hours. Quantitative analysis using densitometry was performed by measuring protein expression relative to the loading control (β-actin). Each value represents the mean ± standard error of the mean (SEM). *$P < 0.01$ by one-way ANOVA and Tukey's post hoc tests.

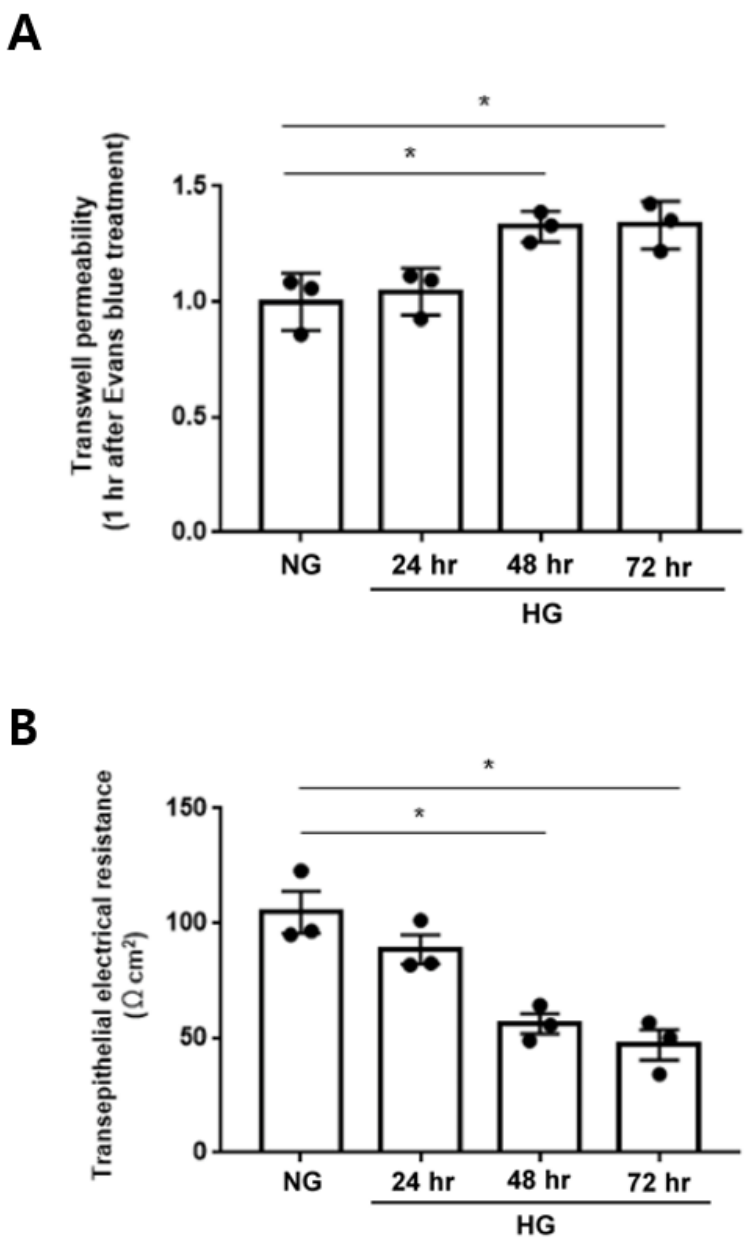

Figure 1.12. High glucose decreases functional integrity of ARPE-19 cells.

(A) Adult retinal pigment epithelial cell line-19 (ARPE-19) cells were treated with normal glucose (5 mM) and high glucose (25 mM) for 24, 48, 72 hours. The ARPE-19 cells monolayer integrity was evaluated by the trans-epithelial permeability test with Evans blue dye. The results are fold changes versus control (normal glucose treatment) and plotted as the mean ± standard error of the mean (SEM) (n=3). *$P < 0.01$ by one-way ANOVA and Tukey's post hoc tests.

(B) Transepithelial electrical resistance was measured using EVOM3 voltohmmeter at 24, 48, 72 hours after the treatment of normal glucose (5 mM) and high glucose (25 mM). Each value represents the mean ± SEM (n=3). *$P < 0.01$ by one-way ANOVA and Tukey's post hoc tests.

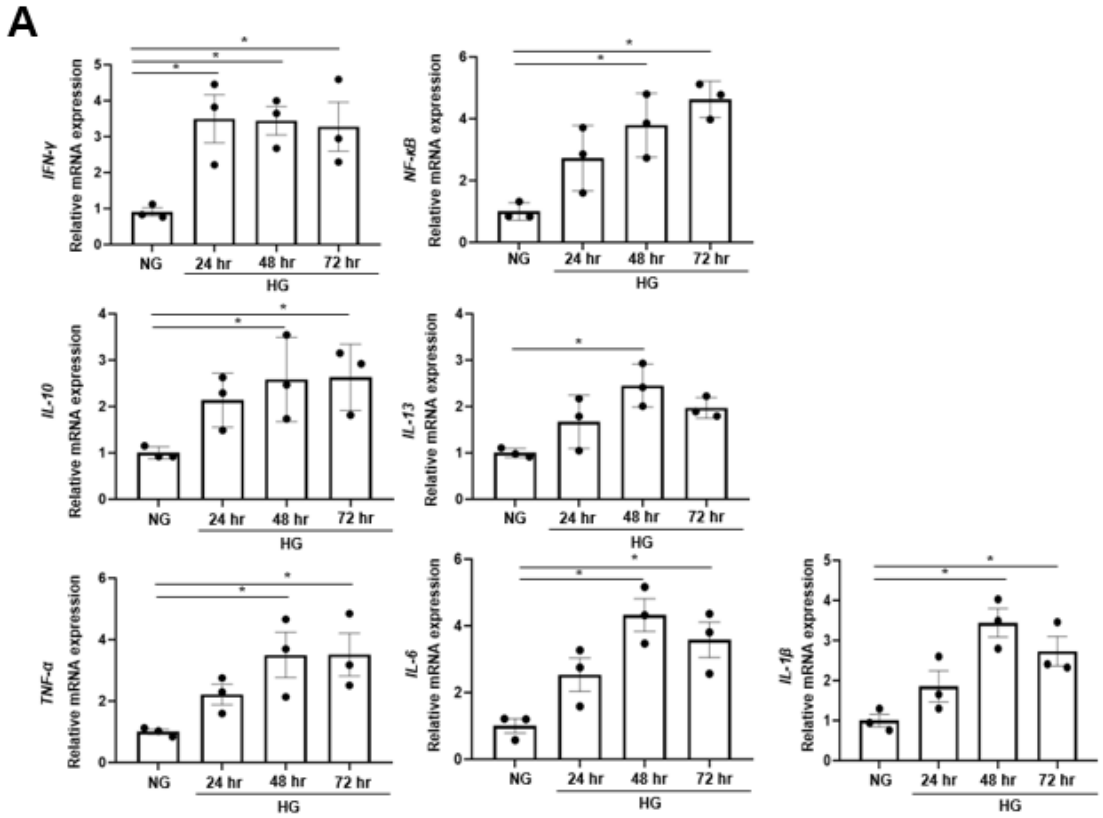

Figure 1.13. High glucose induces secretomal change of ARPE-19 cells related to tight junction integrity and microglia/macrophage polarization.

(A) Adult retinal pigment epithelial cell line-19 (ARPE-19) cells were incubated under normal (5 mM) and high glucose (25 mM) medium for 24, 48, 72 hours and analyzed mRNA levels of interferon gamma (*IFN-γ*), nuclear factor kappa light chain enhancer of activated B cells (*NFκB*), interleukin 10 (*IL-10*), interleukin 13 (*IL-13*), tumor necrosis factor alpha (*TNF-α*), interleukin 6 (*IL-6*), interleukin 1 beta (*IL-1β*). Each value represents the mean ± SEM (n=3). *$P < 0.01$ by one-way ANOVA and Tukey's post hoc tests. D; day.

high glucose treatment induces structural and functional change of RPE, leading to increasing the RPE permeability and secretomal change of RPE.

High glucose induces macrophages into a pro-inflammatory state.

Infiltrating macrophages in response to progression of inflammatory diseases such as diabetes, asthma, and atherosclerosis are considered to play an important role in regulation of tissue inflammation through their polarity change and release of pro- and anti-inflammatory cytokines, chemokines, and growth factors by affecting their surrounding cells (162, 163). In this point of view, the microglia/macrophages also have been suggested having an essential role in microvascular impairment and BRB breakdown in diabetic animal models (60, 61, 164, 165) and DR patients (63, 161). Thus, we examined whether high glucose treatment have direct effects on the macrophage activation and polarity change. We first confirmed human THP-1 monocytes were well differentiated into non-activated, resting (M0) macrophages by an incubation in the presence of phorbol 12-myristate 13-acetate (PMA) which is a widely used differentiation material to study human macrophage biology and function (166). Cells became adherent assessed by light microscopy (Fig. 1.14A) and the expression of representative common macrophage markers, clustered of differentiation 68 (CD68) and clustered of differentiation 14 (CD14) has significantly increased demonstrated by flow cytometry (Figure 1.14B).

Next, we incubated differentiated M0 macrophages under normal and high glucose medium for 24, 48, and 72 hours and evaluated polarity change assessed by flow cytometry following stained with clustered of differentiation 64 (CD64) as a classically activated pro-inflammatory (M1) macrophage marker, clustered of differentiation 163 (CD163) as an alternative anti-inflammatory (M2) macrophage marker, and clustered of differentiation 11b (CD11b) as common macrophage marker. High glucose treatment increased the proportion of $CD11b^{+}CD163^{+}$ cells on the 1 day after treatment compared to normal glucose conditions, while the proportion of CD11b+CD64+ cells increased from 48 hours after treatment. As a positive control, we polarized M0 macrophages into M1 macrophages treated with IFN-γ (20 ng/ml) and LPS (20 ng/ml) or M2 macrophages treated with IL-4 (20 ng/ml) and IL-10 (20 ng/ml) under

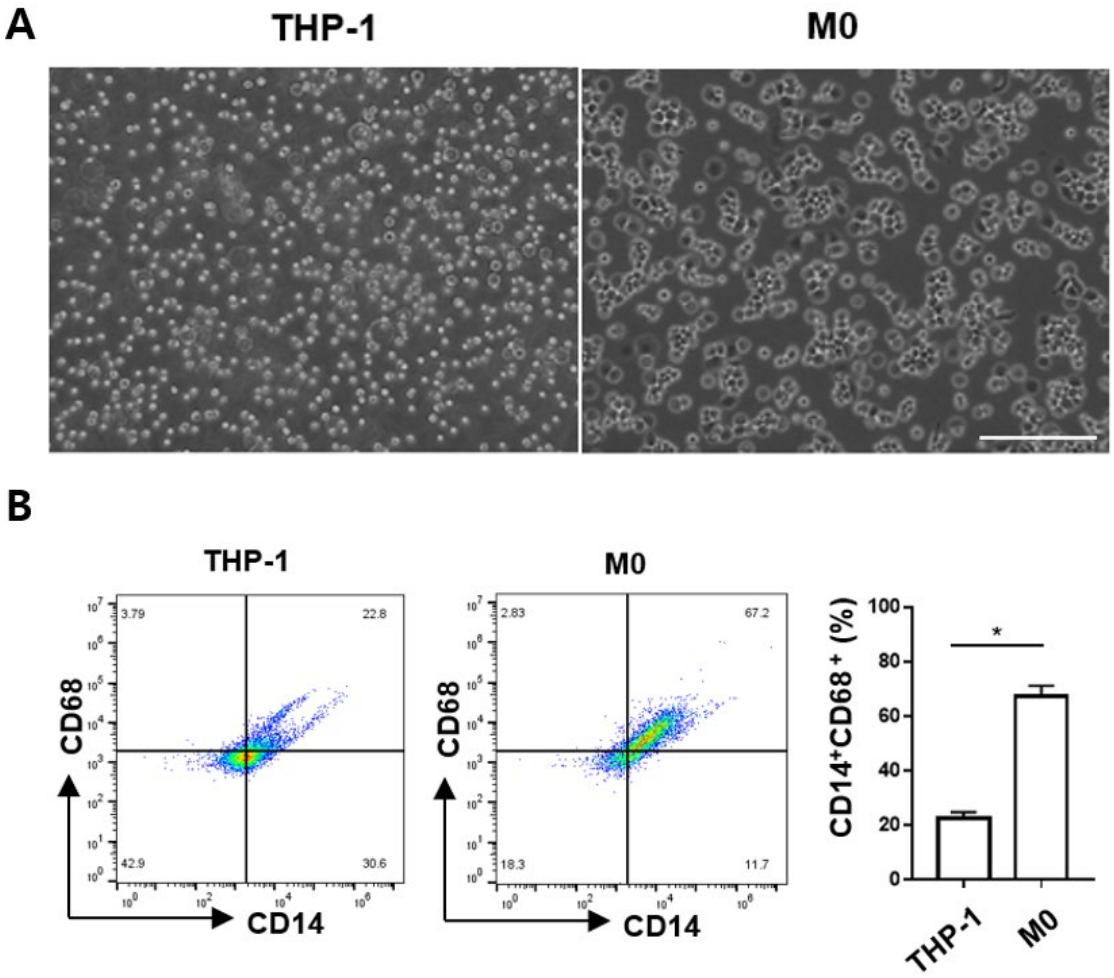

Figure 1.14. THP-1 monocytes differentiation in M0 macrophages.

(A) The human monocytic leukemia cells (THP-1 monocytes) were non-treated or incubated with 10 ng/mL phobol 12-myristate 13-acetate (PMA) for 24 hours and then incubated with the PMA-free medium. Scale bar = 400 μm.

(B) Representative flow cytometry cytograms of $CD14^{+}CD68^{+}$ cells in THP-1 cells and resting stage (M0) cells. Quantification of $CD14^{+}CD68^{+}$cells as analyzed by flow cytometry. The numbers indicate % of total cells. Each value represents the mean ± SEM (n=3). *$P < 0.01$ by Student's t test.

normal glucose medium and confirmed intended polarization with statistically significant high ratio of CD64/CD164 in M1 macrophages and low ratio of CD64/CD164 in M2 macrophages (Fig 1.15A).

To investigate the secretomal change of macrophages under high glucose treatment, which can affect outer BRB and macrophages polarization in DR, we incubated M0 macrophages under normal and high glucose medium for 24, 48, and 72 hours and evaluated the mRNA levels of *iNOS, Arg-1, IL-10, IL-13, TNF-α, IL-6,* and *IL-1β*. High glucose treatment significantly upregulated *iNOS*, M1 marker from the 2 days after treatment, and *Arg-1*, M2 marker on the 24 hours after treatment than those of normal glucose conditions. Among the pro-inflammatory cytokines which are mainly secreted by M1 macrophages, we found that the mRNA transcripts of *TNF-α* and *IL-6* were remarkably increased, while *IL-1β* was not significantly altered. The anti-inflammatory cytokines which are mainly secreted by M2 macrophages, the mRNA transcripts of *IL-10* were increased, while *IL-13* did not significantly change. The representative M1/M2 mRNA expression ratio (*iNOS/Arg-1*) was meaningfully increased at the 48 hours after treatment (Fig 1.15B). These results suggest that high glucose treatment promotes pro-inflammatory M1 macrophage polarization.

Alteration of macrophage polarity additionally influences the structural and functional integrity of ARPE-19 cells under the high glucose condition.

We next wondered whether the alteration of macrophage polarity could additionally affect the structural and functional integrity of ARPE-19 cells under normal and high glucose conditions. We cultured ARPE-19 cells for 14 days under the normal glucose conditions and differentiated macrophages into M0/M1/M2 macrophages, respectively. Then, ARPE-19 cells and macrophages were co-cultured in the transwell plate for 2 days under normal and high glucose conditions (Fig 1.16) followed by immunocytochemistry, transwell permeability, TEER, western blot (WB), and Enzyme-linked immunosorbent assay (ELISA).

Immunostaining data revealed that high glucose treatment remarkably reduced ZO-1 expression in the ARPE-19 alone group compared to normal glucose conditions. Co-culture with ARPE-19 cells and M0 or M1 macrophages under high glucose condition caused the

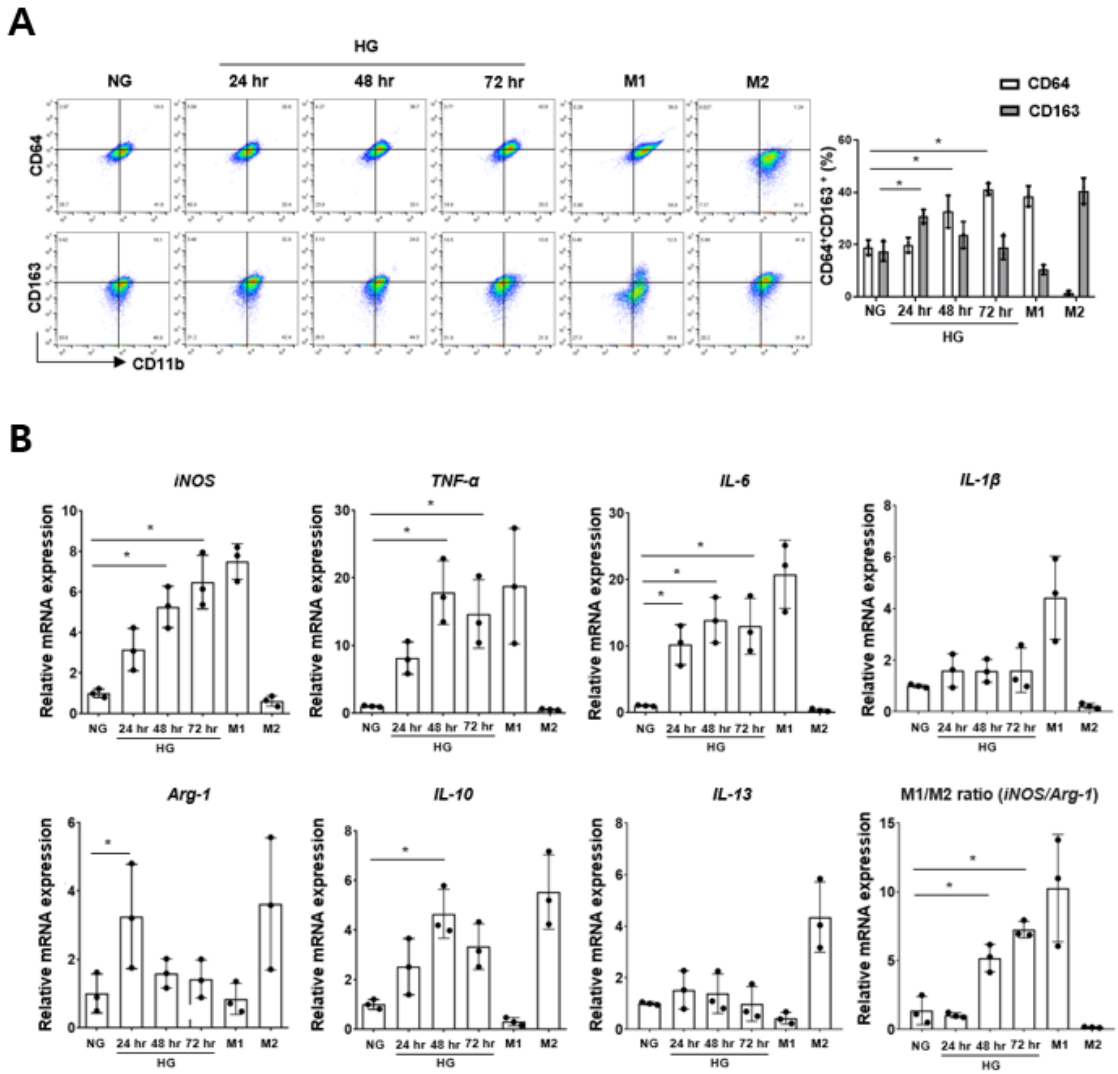

Figure 1.15. High glucose induces macrophages into a pro-inflammatory state.

(A) Representative flow cytometry cytograms of $CD11b^{+}CD64^{+}$ and $CD11b^{+}CD163^{+}$ cells in resting stage (M0) cells after incubation under normal (5 mM) and high glucose (25 mM) medium for 24, 48, 72 hours. Classically activated pro-inflammatory (M1) macrophages and alternative anti-inflammatory (M2) macrophages were induced by treated with IFN-γ (20 ng/ml) and LPS (20 ng/ml) or IL-4 (20 ng/ml) and IL-10 (20 ng/ml) under normal glucose medium, respectively as positive control group. Quantification of $CD64^{+}CD163^{+}$cells as analyzed by flow cytometry. The numbers indicate % of total cells. Each value represents the mean ± SEM (n=3). *$P < 0.01$ by one-way ANOVA and Tukey's post hoc tests.

(B) The inducible nitric oxide synthase (*iNOS*), tumor necrosis factor alpha (*TNF-α*), interleukin 6 (*IL-6*), interleukin 1 beta (*IL-1β*), arginase-1 (*Arg-1*), interleukin 10 (*IL-10*), interleukin 13 (*IL-13*) mRNA transcription were analyzed. Each value represents the mean ± SEM (n=3). *$P <$

0.01 by one-way ANOVA and Tukey's post hoc tests.

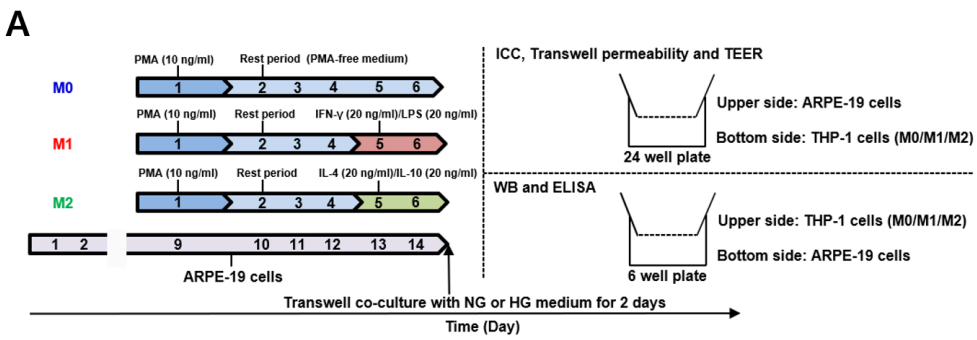

Figure 1.16. Timeline of co-culture experiments.

(A) Timeline of co-culture experiments of adult retinal pigment epithelial cell line-19 (ARPE-19) cells with resting stage (M0)/classically activated pro-inflammatory (M1)/alternative anti-inflammatory (M2) macrophages. ARPE-19 cells were cultured for 14 days under the normal glucose condition in DMEM/F-12 medium (a mixture of Dulbecco's Modified Eagle Medium and Ham's F-12 Nutrient Mix) with a normal glucose concentration (NG, 5 mM). Differentiation of the human monocytic leukemia cells, THP-1 cells into M0 macrophages was performed by incubating the cells with 10 ng/mL phobol 12-myristate 13-acetate (PMA) for 24 hours and then resting for 5 days incubated with the PMA-free medium. M1 or M2 macrophages were polarized from M0 macrophages by incubating the macrophages with 10 ng/mL PMA containing media for 24 hours and then resting for 72 hours incubated with the PMA-free medium before exposing the primed cells to 20 ng/ml of interferon gamma (IFN-γ) and 20 ng/ml of lipopolysaccharides (LPS) containing media for M1 macrophages or 20 ng/ml of interleukin 4 (IL-4) and 20 ng/ml of interleukin 10 (IL-10) for M2 macrophages. Thereafter, ARPE-19 cells were co-cultured with differentiated M0/M1/M2 macrophages under normal glucose (5 mM) and high glucose (25 mM) medium.

additional reduction of ZO-1 expression than that of ARPE-19 alone group under high glucose conditions, while co-culture with ARPE-19 cells and M2 macrophages notably recovered ZO-1 expression (Figure 1.17A). We also conducted WB analyses of the ARPE-19 cells, and our results showed that co-culture with ARPE-19 cells and M2 macrophages prevented downregulation of ZO-1 and occludin in the co-culture with ARPE-19 cells and M0 or M1 macrophages under the high glucose conditions (Fig. 1.17B).

To address whether different types of macrophage polarization could additionally affect functional integrity of APRE-19 cells, we examined transwell epithelial permeability and TEER in co-culture model with ARPE-19 cells and M0/M1/M2 macrophages. When the APRE-19 cells were co-cultured with M0 or M1 macrophages, ARPE-19 cells permeability was increased and TEER was decreased than those of under normal glucose conditions, while co-culture with ARPE-19 cells and M2 macrophages under high glucose conditions significantly reversed the effects of the co-culture conditions with APRE-19 cells and M1 macrophages (Fig. 1.18). ELISA analysis of the co-culture medium of ARPE-19 cells and M0 or M1 macrophages under high glucose conditions confirmed the increased level of TNF-α which is a mainly secreted inflammatory cytokine by M1 macrophages and is also known to induce the disruption of tight junction complexes between RPE cells (62, 167), while this effect was inhibited in the co-culture conditions of ARPE-19 cells and M2 macrophages (Fig. 1.19A). We also examined the ELISA analysis of IL-10 which is a mainly secreted anti-inflammatory cytokine by M2 macrophages and is known to inhibit nuclear factor kappa B (NFκB) activation that is related to disruption of RPE integrity (62, 168, 169). We confirmed the increased level of IL-10 in the co-culture conditions of ARPE-19 cells and M2 macrophages compared to co-culture conditions of ARPE-19 cells and M0 or M1 macrophages (Fig. 1.19B). These results demonstrate that modulation of macrophage polarization additionally influences the structural and functional integrity of APRE-19 cells under high glucose conditions.

The tight junction disruption along with increased number of microglia/macrophage recruitment and secretomal change of RPE occur during the early-stage DR progression.

Clinical evidence of RPE barrier breakdown and an increased leakage of blood content which is

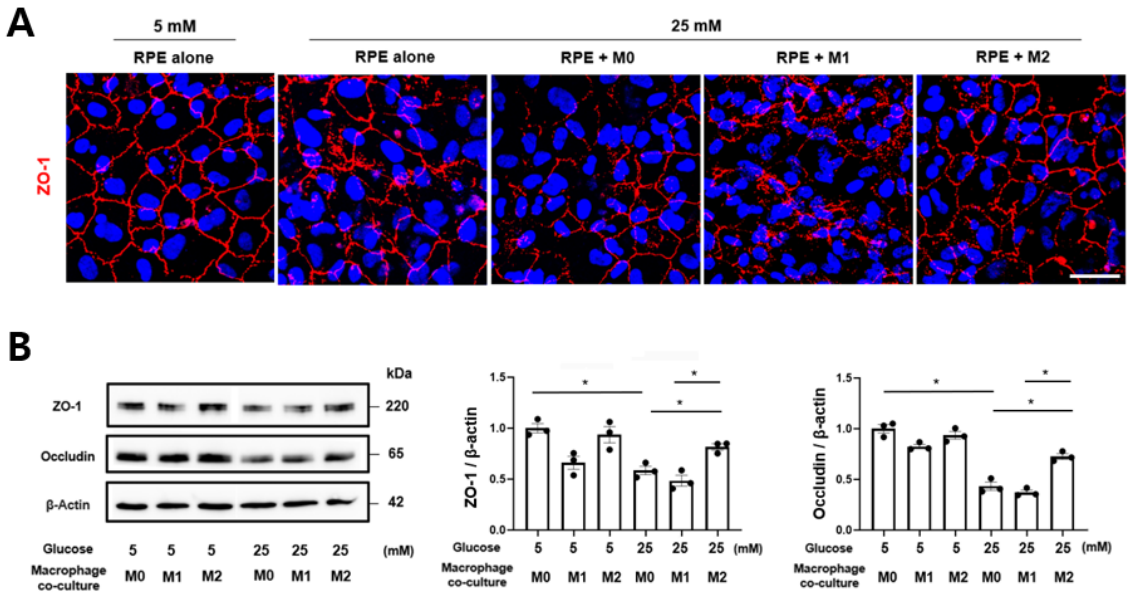

Figure 1.17. Alteration of macrophage polarity additionally influences the structural integrity of ARPE-19 cells under the high glucose condition.

(A) Representative immunofluorescence images stained with anti-zonula occludens-1 (ZO-1, red) and 4'6'-diamidino-2-phenylindole (DAPI, blue) in adult retinal pigment epithelial cell line-19 (ARPE-19) cells after 48 hours of co-culture with or without resting stage (M0) or classically activated pro-inflammatory (M1) or alternative anti-inflammatory (M2) macrophages under normal glucose (5 mM) or high glucose (25 mM) medium. Scale bar = 20 μm.

(B) Representative western blot data showing the expression of ZO-1, occludin, and beta-actin (β-actin) in different co-culture groups. Quantitative analysis using densitometry was performed by measuring protein expression relative to the loading control (β-actin). Each value represents the mean ± standard error of the mean (SEM). *$P < 0.01$ by one-way ANOVA and Tukey's post hoc tests.

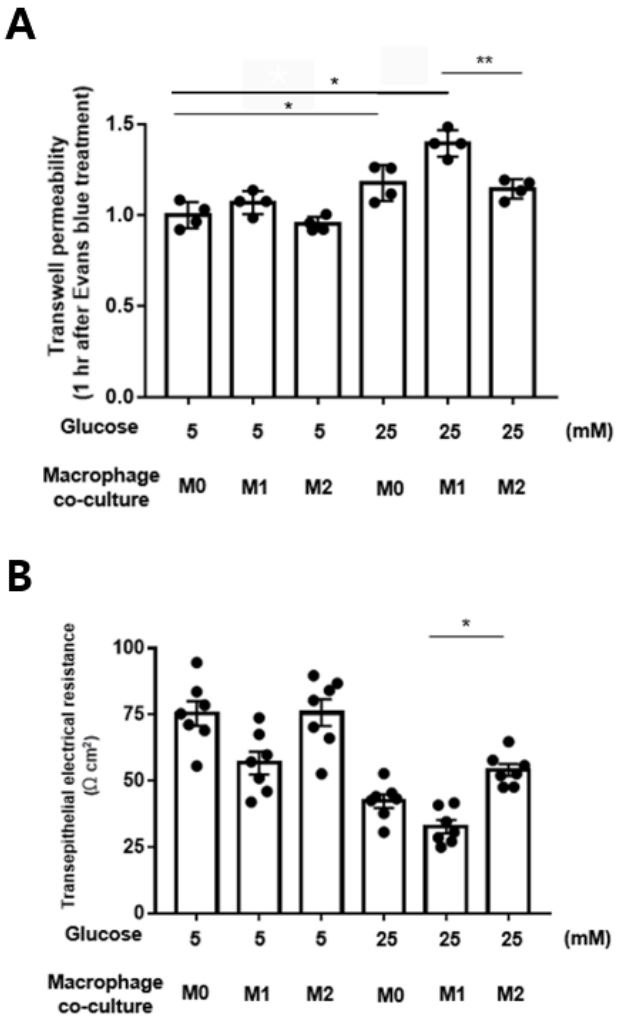

Figure 1.18. Alteration of macrophage polarity additionally influences the functional integrity of ARPE-19 cells under the high glucose condition.

(A) The adult retinal pigment epithelial cell line-19 (ARPE-19) cells monolayer integrity was evaluated by the trans-epithelial permeability test with Evans blue dye. ARPE-19 cells were co-cultured with resting stage (M0) or classically activated pro-inflammatory (M1) or alternative anti-inflammatory (M2) macrophages under normal glucose (5 mM) and high glucose (25 mM) medium for 48 hours. Each value represents the mean ± standard error of the mean (SEM) (n=4). *$P < 0.01$ by one-way ANOVA and Tukey's post hoc tests.

(B) Transepithelial electrical resistance was measured using EVOM3 voltohmmeter at 48 hours after co-culture with ARPE-19 cells and M0/M1/M2 macrophages under the treatment of normal glucose (5 mM) or high glucose (25 mM). Each value represents the mean ± SEM (n=7). *$P < 0.01$, **$P < 0.001$ by one-way ANOVA and Tukey's post hoc tests.

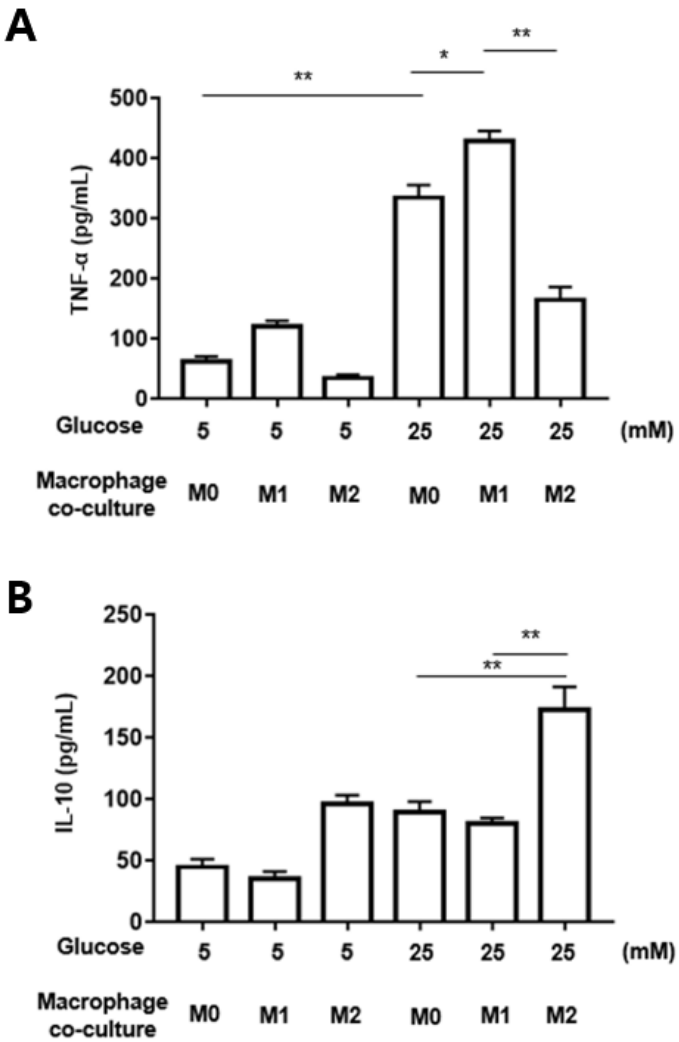

Figure 1.19. Relative amounts of TNF-α and IL-10 in the co-cultured medium from ELISA analyses

(A) The tumor necrosis factor alpha (TNF-α) protein amounts in the supernatant media were determined by ELISA (n=3).

(B) The interleukin 10 (IL-10) protein amounts in the supernatant media were determined by ELISA (n=3). Each value represents the mean ± standard error of the mean (SEM). *$P < 0.01$, **$P < 0.001$ by one-way ANOVA and Tukey's post hoc tests.

capable of causing diabetic macular edema has been observed in human DR (170, 171) and diabetic rat (144, 147, 172). Furthermore, recruitment of microglia/macrophages in the RPE layer of the diabetic mouse (62) and subretinal accumulation of microglia/macrophages through transcellular pores within RPE of the diabetic rat (147, 153) and human DR (173) also have been observed. Based on these observations, we hypothesized that recruited microglia/macrophages in the RPE layer could involve outer BRB disruption.

We first examined whether the outer BRB disruption is observed in the streptozotocin-treated DR mouse model, representative of type 1 diabetes which almost patients develop DR (174). We confirmed the intense fluorescent signals in the outer retina, between outer nuclear layer and RPE layer and significant tight junction disruption of RPE monolayer sheets at 2-week and 4-week streptozotocin-induced diabetic mice, which was not present in control mice (Fig. 1.20A and C). In addition, the tight junction disruption and immunopositivity area of ionized calcium binding adaptor molecule 1 (Iba-1), microglia/macrophage-specific marker in the RPE layer were significantly increased at 2-week and 4-week streptozotocin-induced diabetic mice than that in control mice, and these recruited microglia/macrophages to the RPE layer correspond to locations where tight junction disruption occurs (Fig. 1.20B and C). Furthermore, qRT-PCR analyses in RPE-choroid-scleral (RCS) complexes of STZ-treated mice demonstrated a significant increase in the level of *TNF-α*, *IL-10, NFκB* mRNA, which are important factors related to RPE integrity (Fig. 1.21). These results demonstrated that not only outer BRB disruption along with the increased number of microglia/macrophage recruitment but also secretomal change of RPE occur during the early stage of streptozotocin-induced DR progression.

The polarity changes of recruited microglia/macrophages occur during the early-stage of streptozotocin-induced DR progression.

Based on the previous reports about microglia/macrophage polarity change during the progression of db/db mice, representative of type 2 diabetes and increased mRNA level of Iba-1 (microglia/macrophage marker) and inducible nitric oxide synthase (iNOS as pro-inflammatory M1 marker), Arginase-1 (Arg-1 as anti-inflammatory M2 marker) in post-mortem diabetic

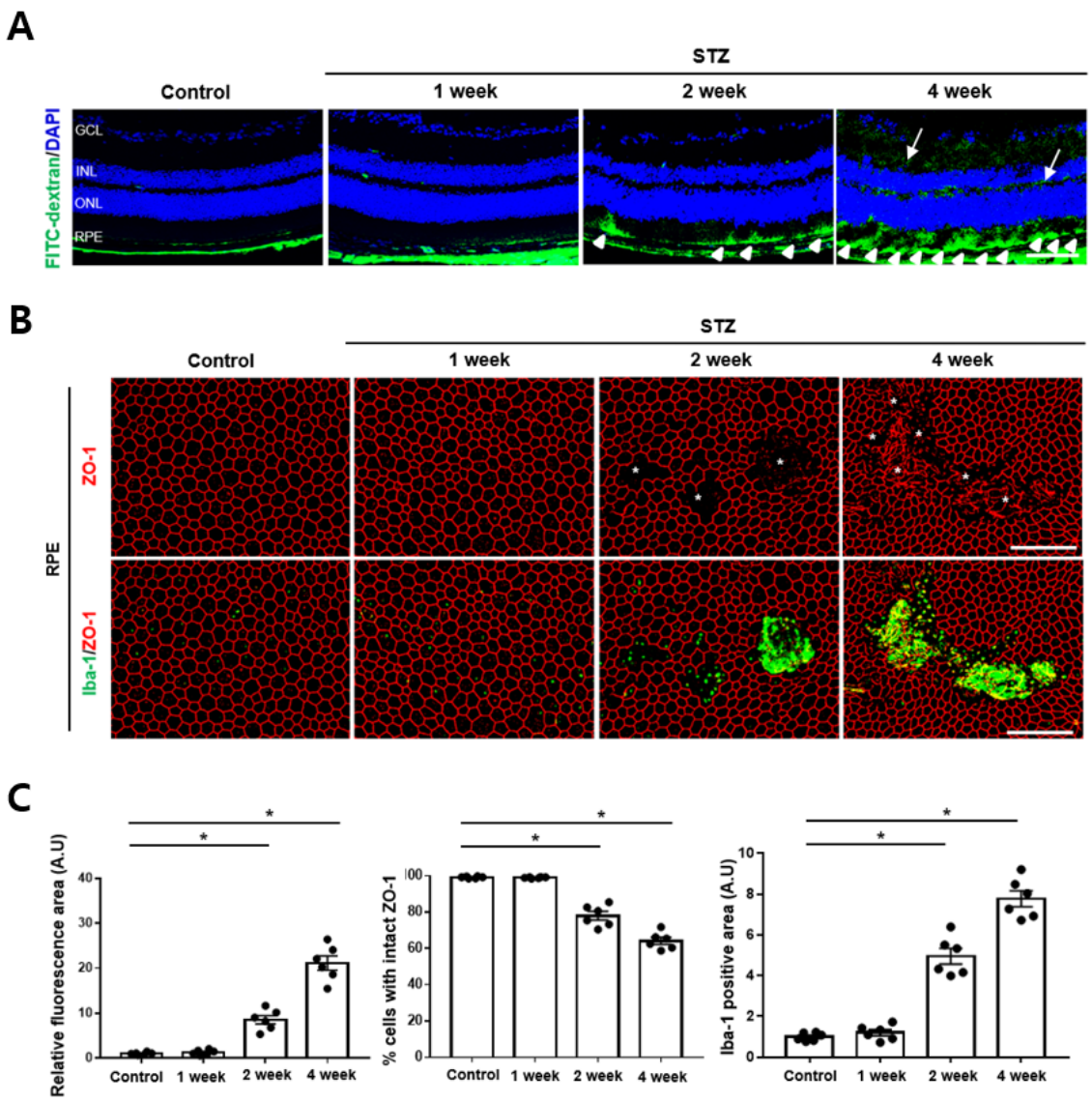

Figure 1.20. Breakdown of the retinal pigment epithelium barrier and vascular leakage in retinal section and microglia/macrophage recruitment in the whole-mounted RPE layer of STZ-induced diabetic mice.

(A) Imaging of vascular leakage in retinal sections from mice injected with fluorescence-labeled dextran (FITC-dextran, 60 kDa, 100 mg/kg) intracardiaclly. Arrows indicate microvascular leakage induced by inner blood-retinal barrier (BRB) disruption. Arrowheads indicate RPE barrier break points (outer BRB disruption) with vascular hyperpermeability at the subretinal space between photoreceptor layer and RPE layer. Scale bar = 100 μm. GCL = ganglion cell layer; INL = inner nuclear layer; ONL = outer nuclear layer; RPE = retinal pigment epithelium.

(B) Whole-mounted RPE layer stained with zonular occludens-1 (ZO-1, red) and ionized calcium binding adaptor molecule 1 (Iba-1, green). In controls, ZO-1 labeled the regular

hexagonal membrane of RPE cells, whereas in STZ-induced diabetic conditions, we observed some enlarged RPE cells with irregular ZO-1 labelling showing loss of tight junctions (asterisk) and numerous recruited Iba-1 positive cells mainly on the locations where the tight junction disruption occurs. Scale bar = 100 μm.

(C) Quantitative analyses for vascular leakage in retinal section, percentage of cells with intact ZO-1 in RPE sheets, and relative fluorescence intensity of Iba-1 positive area. All quantitative data were analyzed with NIH ImageJ software, and each value represents the mean ± standard error of the mean (SEM) (n = 6 mice for each data set). $*P < 0.01$ by one-way ANOVA and Tukey's post hoc tests.

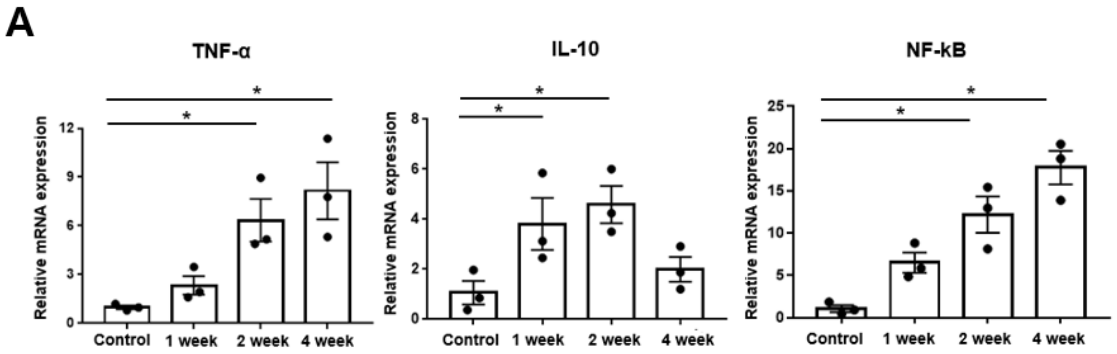

Figure 1.21. The mRNA expression of TNF-α, IL-10, and NFκB in the RCS complexes of STZ-induced diabetic mice.

(A) The level of tumor necrosis factor alpha (TNF-α), interleukin 10 (IL-10), nuclear factor kappa light chain enhancer of activated B cells (NF-κB) mRNA expression was analyzed in the retinal pigment epithelium-choroid-sclera complexes of at 1-week, 2-week and 4-week streptozotocin-induced diabetic mice. Each value represents the mean standard error of the mean (SEM, n=3 mice for each group set). *$P < 0.01$ by one-way ANOVA and Tukey's post hoc tests.

donor (154), we examined the expression and distribution of M1 and M2 markers (iNOS and Arg-1, respectively) to determine microglia/macrophage polarity change in the retinas of STZ-induced diabetic mice during DR progression. The immunofluorescence analysis in retinal sections revealed increased iNOS$^+$Iba-1$^+$ specific immunostaining both in inner retina and outer retina at 2-week and 4-week STZ-induced diabetic mice and increased Arg-1$^+$Iba-1$^+$ specific immunostaining in inner retina at 1-week, 2-week, and 4-week and in outer retina at 2-week and 4-week STZ-induced diabetic mice compared to control mice. Furthermore, the ratio of positive fluorescence area (iNOS/Arg-1) was significantly increased in inner retina at 2-week, and 4-week and in outer retina at 1-week, 2-week, and 4-week STZ-induced diabetic mice compared to control mice (Fig. 1.22). Taken together, the pre-dominant polarity changes of recruited microglia/macrophages occur during the early stage of streptozotocin-induced DR progression.

Intravitreal IL-10 injection significantly decreases M1/M2 polarization ratio and effectively suppresses outer BRB disruption in the early-stage of streptozotocin-induced diabetic mouse.

Given that not only the significant change of outer BRB breakdown and M1/M2 marker ratio at outer retina has been found between 1-week and 2-week hyperglycemia in STZ-induced diabetic mice compared to normal mice and but also changes of inner BRB breakdown such as retinal vascular leakage, pericyte loss and astrocyte loss has been reported begun between 3- to 8-week hyperglycemia in STZ-induced diabetic mice (140, 141, 175, 176), we evaluated whether modulation of recruited microglia/macrophages polarization in the retina from M1 to M2 could affect integrity of outer BRB at the early-stage of STZ-induced diabetic mice.

We conducted intravitreal IL-10 (50 ng/eye), M2 inducer injection at 11 days STZ-induced diabetic mice and examined the outer BRB disruption and microglia/macrophage polarity change at 14 days STZ-induced diabetic mice (Fig. 1.23). Three days after the intravitreal injection of mouse IL-10, the fluorescence leakage in outer retina was significantly decreased compared to that of the STZ-induced diabetic mice without IL-10 administration (Fig. 1.24). The IL-10 treatment also ameliorated the tight junction disruption of RPE tissues along with decreased ratio of iNOS$^+$Iba-1$^+$/Arg-1$^+$ Iba-1$^+$ area (Fig. 1.25). These results

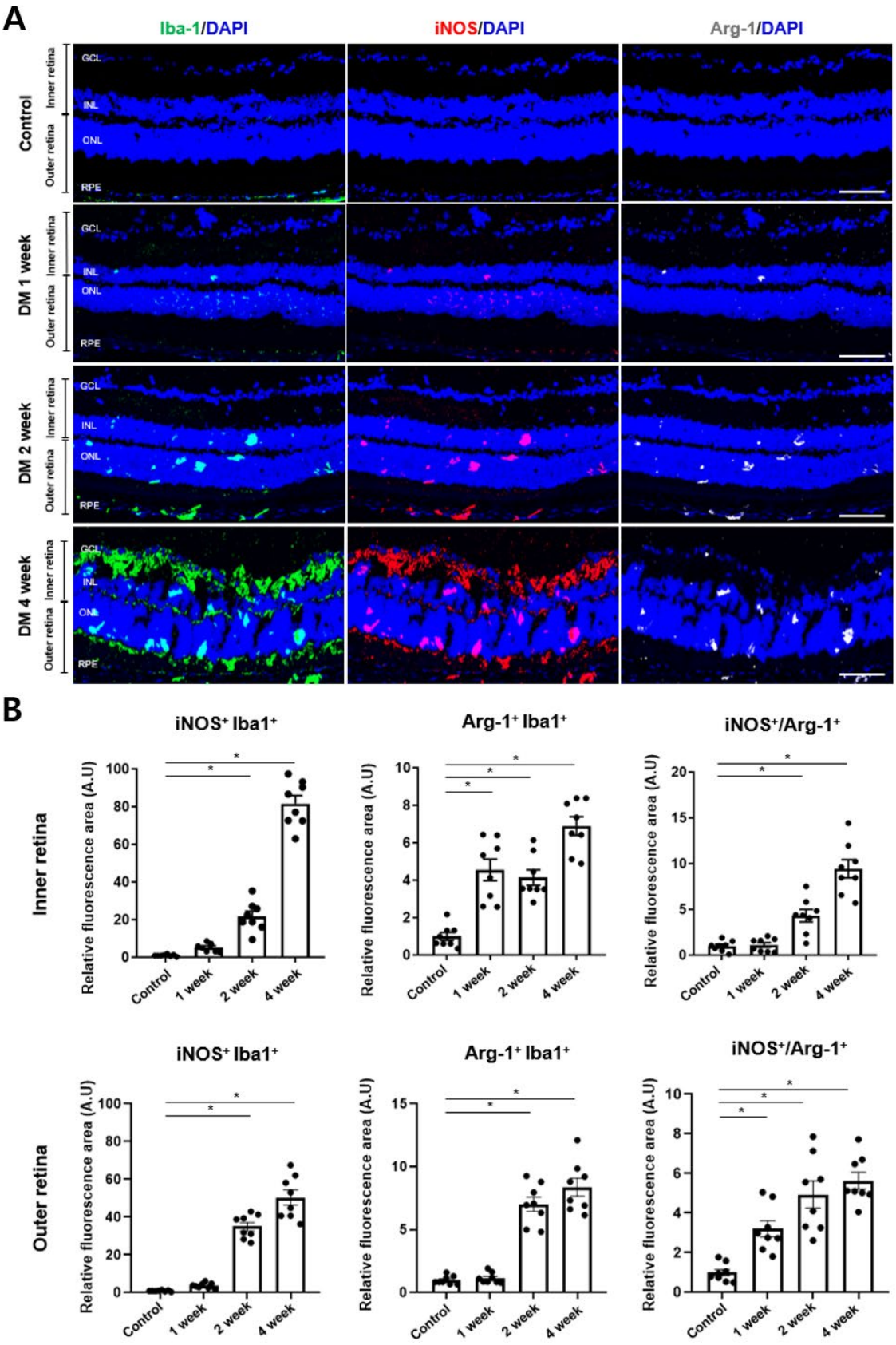

Figure 1.22. Analysis of M1 and M2 markers in retinas from STZ-induced diabetic mice during DR progression.

(A) Representative immunofluorescence images in retinal sections stained with ionized calcium

binding adaptor molecule 1 (Iba-1 as microglia/macrophage marker, green), inducible nitric oxide synthase (iNOS as pro-inflammatory M1 marker, red), Arginase-1 (Arg-1 as anti-inflammatory M2 marker, grey), and 4'6'-diamidino-2-phenylindole (DAPI, blue). Scale bar, 100 μm. The inner retina consists of the internal limiting membrane through to the inner nuclear layer, and the outer retina consists of the outer nuclear layer through to the retinal pigment epithelium (RPE). GCL = ganglion cell layer; INL = inner nuclear layer; ONL = outer nuclear layer; RPE = retinal pigment epithelium.

(B) Quantitative analyses of the Iba-1, iNOS, and Arg-1-positive area at inner retina and outer retina in the retinal section of control and streptozotocin-treated mice. Each value represents the mean standard error of the mean (SEM, n=8 mice for each group set). $*P < 0.01$ by one-way ANOVA and Tukey's post hoc tests.

Figure 1.23. Experimental timeline of IL-10 administration and tissue preparation in STZ-induced diabetic mouse model.

(A) Timeline of interleukin 10 (IL-10, 50 ng/eye), M2 inducer administration in streptozotocin (STZ)-induced diabetic mouse model.

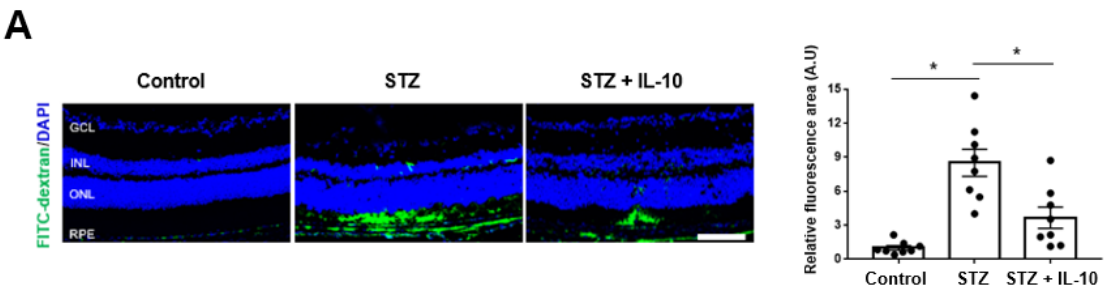

Figure 1.24. Evaluation of blood-retinal barrier leakage in retinal section of STZ-induced diabetic mice receiving IL-10, M2 inducer.

(A) Representative fluorescence images of retinal section comparing fluorescence-labeled dextran (FITC-dextran, 60 kDa, 100 mg/kg) staining pattern as measurement of outer blood-retinal barrier leakage at 3 days after intravitreal injection. Age-matched control mice were administered with vehicle control (citrate buffer) and streptozotocin-induced diabetic mice were administered with or without interleukin 10 (IL-10, 50 ng/eye). Scale bar = 500 μm. Each value represents the mean standard error of the mean (SEM, n=8 mice for each group set). *$P < 0.01$ by one-way ANOVA and Tukey's post hoc tests. GCL = ganglion cell layer; INL = inner nuclear layer; ONL = outer nuclear layer; RPE = retinal pigment epithelium

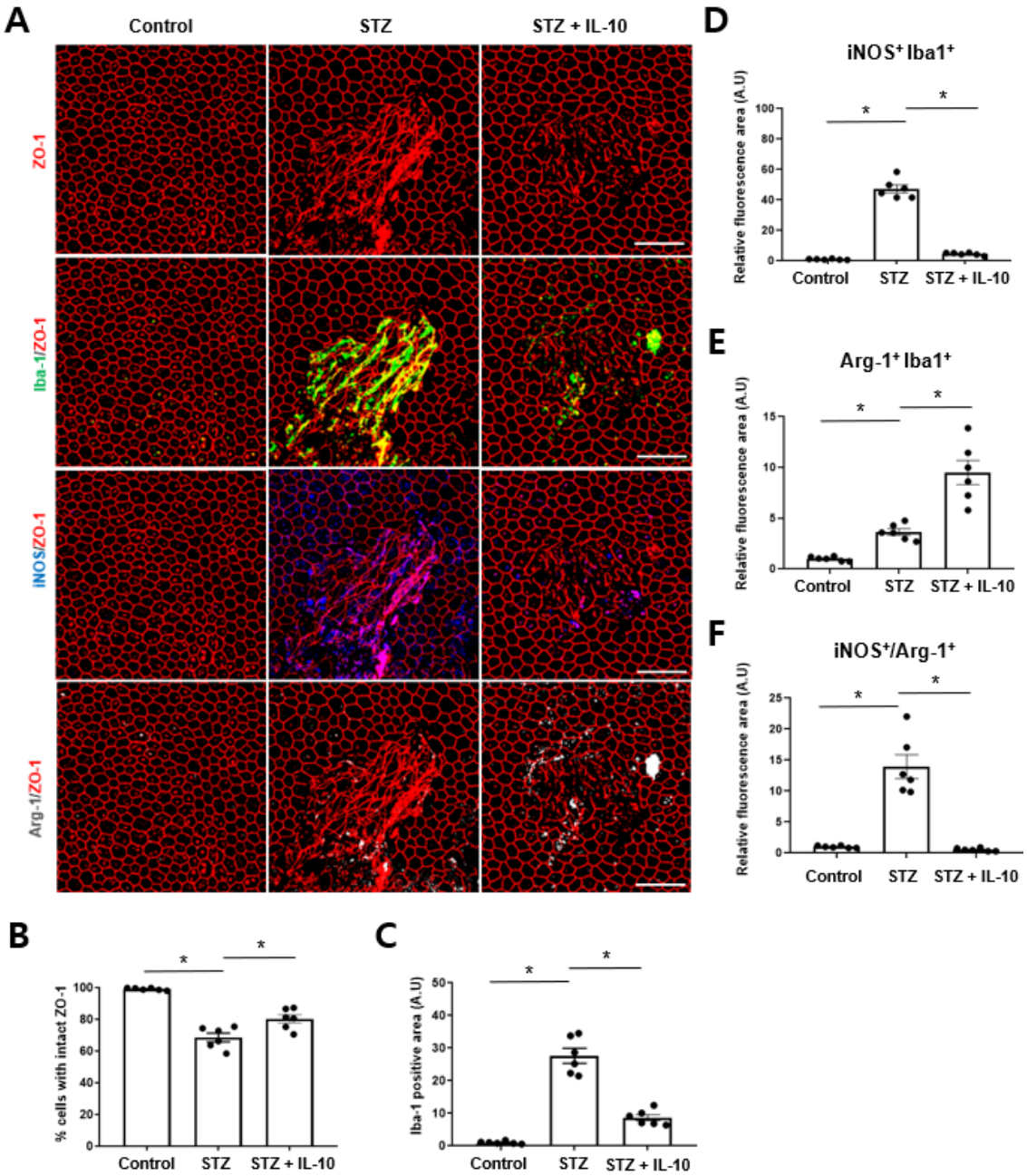

Figure 1.25. Intravitreal IL-10 injection decreases M1/M2 polarization ratio and effectively suppresses outer BRB disruption in the early-stage of streptozotocin-induced diabetic mouse.

(A) Representative immunofluorescence images stained with anti-zonula occludens-1 (ZO-1, red), ionized calcium binding adaptor molecule 1 (Iba-1 as microglia/macrophage marker, green), inducible nitric oxide synthase (iNOS as pro-inflammatory M1 marker, blue), Arginase-1 (Arg-1 as anti-inflammatory M2 marker, grey) in retinal pigment epithelium (RPE) tissues of age-matched control mice administered with vehicle control (citrate buffer) and streptozotocin-induced diabetic mice administered with or without interleukin 10 (IL-10, 50 ng/eye). Scale bar

= 100 μm.

(B) Quantitative analyses of percentage of cells with intact ZO-1 in RPE sheets.

(C) Quantitative analyses of relative fluorescence intensity of Iba-1 positive area.

(D-F) Quantitative analyses of Iba-1, iNOS, and Arg-1-positive area at RPE tissues. All quantitative data were analyzed with NIH ImageJ software, and each value represents the mean ± standard error of the mean (SEM) (n = 6 mice for each data set). $*P < 0.01$ by one-way ANOVA and Tukey's post hoc tests.

suggest that intravitreal injection of IL-10 effectively induces M2 polarization of recruited microglia/macrophage in the RPE layer and effectively suppressed outer BRB disruption in the early-stage of STZ-induced diabetic mice.

DISCUSSION

In this study, we observed a decrease in the structural and functional integrity of RPE cells and the transition to the pro-inflammatory state of macrophages under high glucose conditions. Furthermore, we confirmed that tight junction expression in RPE cells was additionally influenced by changes in macrophage polarity under co-culture conditions. Based on these *in vitro* results, this study was planned to conduct in vivo studies using STZ-induced diabetic mice to evaluate the relationship between disruption of the outer BRB, vascular leakage, and microglia/macrophage polarity change. We found not only outer BRB disruption and increased vascular leakage at the outer retina but also increased recruitment of microglia/macrophages, mainly at the locations where tight junction disruption of RPE occurs and increased M1/M2 microglia/macrophage polarity ratio during the progression of STZ-induced diabetes. Thereafter, we confirmed that the intravitreal IL-10, M2 inducer injection induced a decrease of M1/M2 polarization ratio and significantly suppressed outer BRB disruption and vascular leakage.

RPE is a polarized and pigmented monolayer epithelium located between the neurosensory retina and choroidal vessel, exerting numerous essential functions in retinal homeostasis such as absorption of light, phagocytosis, participation in the visual cycle, secretion of various cytokines, chemokines, growth factors, and maintenance of the outer BRB (159, 160, 177). Although the contribution of the RPE to the pathogenesis of DR remains largely unknown, there have been reports of diabetes-induced alteration on the RPE, including tight junction disruption, vascular leakage, and change of organelles in diabetic animal models (145, 146, 148, 178) and changes in RPE thickness of DR patients (179-181). We first investigated whether high glucose treatment affects structural and functional integrity and secretomal changes in APRE-19 cells. High glucose treatment significantly induced tight junction disruption and decreased functional integrity of APRE-19 cells (Fig. 1.11 and 1.12) and induced secretomal changes related to outer BRB disruption and microglia/macrophage polarization (Fig. 1.13). These results were consistent with previous reports on high glucose treatment-induced RPE integrity (62, 182) and secretomal changes in the RPE (160).

DR is a representative inflammatory retinal disease that includes uveitis, retinal

vascular occlusion, age-related macular degeneration, infectious retinitis, and retinitis pigmentosa (183). Inflammation refers to the invasion of immune cells to resolve tissue damage. It is well known that microglia/macrophages can modulate inflammatory processes through release of various cytokines, chemokines, and growth factors, which depend on phenotype change of their polarity. In hyperglycemia-induced inflammatory conditions, microglia/macrophage activation and phenotypic changes in the retinal layers including RPE, have been observed in diabetic animal model (59-62) and DR patients (63). These findings indicate that the activation of microglia/macrophages is a specific feature of DR and could influence outer BRB disruption and RPE leakage by releasing secretory factors. Thus, we examined the polarity change as well as the secretomal changes in macrophages under high glucose conditions. We confirmed that high glucose treatment leads macrophages to a pro-inflammatory state with increased release of pro-inflammatory cytokines rather than anti-inflammatory cytokines (Fig. 1.14 and 1.15)

Although the processes related to RPE barrier alteration *in vivo* are not fully understood, the release of several pro-inflammatory cytokines including TNF-α, IL-1β (184, 185), vascular endothelial growth factors (186, 187), matrix metalloproteinase (188, 189), cytoskeleton regulatory proteins (147, 190), and mast cell degranulation (191), is involved in RPE barrier dysfunction. In this regard, we co-cultured APRE-19 cells and macrophages with different polarization phenotypes under normal and high glucose conditions to evaluate the additional effects on the structural and functional integrity of APRE-19 cells. It was found that co-culture of ARPE-19 cells with M2 macrophages enhanced the structural and functional integrity of APRE-19 cells under high glucose conditions (Fig. 1.17 and 1.18). These results may be attributed to M2 macrophages secreting less pro-inflammatory cytokines such as TNF-α, IL-1β, and IL-6, and more anti-inflammatory cytokines, such as IL-4, IL-10, and IL-13, as demonstrated by RT-PCR (Fig. 1.15B) and ELISA (Fig. 1.19).

Using a streptozotocin-induced diabetic mouse model, representative of type 1 diabetes, in which almost all patients develop DR, we examined whether outer BRB disruption occurs and when it occurs. We confirmed the leakage of blood content confined to the outer retina, which is likely to be more associated with outer BRB disruption than inner BRB disruption and

significant tight junction disruption of the RPE layer at 2-week and 4-week of STZ-induced diabetic mice (Fig. 1.20). The levels of pro- and anti-inflammatory cytokines linked with outer BRB disruption were significantly elevated corresponding to the period of outer BRB disruption in STZ-induced diabetic mice (Fig. 1.21). Furthermore, we also found increased recruitment of microglia/macrophages to the RPE layer at 2-week and 4-week of STZ-induced diabetic mice, implying a positive relationship between outer BRB disruption and microglia/macrophage recruitment (Fig. 1.20 B and C).

Next, we examined the polarity change of the microglia/macrophages recruited to the retina during the early stage of DR progression. We confirmed that the polarity changes of recruited microglia/macrophages occurred with an increased M1/M2 ratio during the early stage of DR progression (Fig. 1.22). Thereafter, we evaluated whether modulation of microglia/macrophages polarization from M1 to M2 affects the integrity of the outer BRB at early stage of STZ-induced diabetic mice. To exclude the confounding effect of other retinal cells such as neurovascular units composed of inner BRB against outer BRB disruption under diabetic conditions, we intravitreally injected IL-10, a representative M2 inducer, at 11 days in STZ-induced diabetic mice and confirmed outer BRB disruption and microglia/macrophage polarity change at 14 days in STZ-induced diabetic mice (Fig. 1.23). We demonstrated that intravitreal IL-10 injection significantly decreased the M1/M2 polarization ratio and effectively suppressed outer BRB disruption in the early stages of STZ-induced diabetic mice (Fig. 1.24 and Fig. 1.25).

This is the first study to demonstrate the relationship between the polarity regulation of microglia/macrophage and outer BRB disruption in the early stage of STZ-induced diabetic mouse as far as we know. The limitations of our study are as follows. Given that DR and DME are multifactorial diseases with complex pathophysiology involved by various retinal cells, our study did not completely exclude the effect on outer BRB disruption by other retinal cells such as retinal vascular endothelial cell, pericyte, astrocyte, Müller cells under high glucose conditions. Instead, we found the timepoint that was only observed in the outer BRB disruption, while no change was observed in the inner BRB and neurovascular units in the STZ-induced diabetic mouse and focused on the effect of microglia/macrophage polarity change against outer

BRB disruption. Another important limitation was the use of diabetic mice, in which the fovea, the region composed of closely packed photoreceptor cells responsible for central vision in DME patients is lack. Instead, conventional mice with STZ-induced diabetes have the well-known disease phenotypes of vascular permeability and BRB disruption observed in patients with DME. As shown in Fig.1.24 and Fig.1.25, administration of IL-10 suppressed the increase in vascular permeability of the outer retina and increased in the outer BRB disruption, accompanied by a decreased M1/M2 polarization ratio and decreased number of microglia/macrophages. It is also necessary to consider that our results show a positive effect on outer BRB disruption of IL-10 only at a very early period of DR. Given that DR is an inflammatory retinal disease affected by chronic hyperglycemic damage, further comprehensive studies that consider the therapeutic effect of macrophage polarity modulation on inner and outer BRB disruption not only in the early period of DR but also intermediate and long periods of DR will be helpful in determining its translational value.

Despite the above limitations, this study experimentally showed that the modulation of the polarization phenotype of microglia/macrophages by IL-10 administration during early stage of DR has the potential to protect against outer BRB disruption and vascular leakage. These results suggest that microglia/macrophages are involved in the disruption of the outer BRB function in DR, supporting our proposal that modulation of microglia/macrophage polarization provides a novel therapeutic target and insights for early intervention of DR.

CHAPTER 2-1

Regulation of Choroidal Neovascularization in Age-Related Macular Degeneration via Intravitreal Antibody-Drug Conjugate Injection

INTRODUCTION

As intraocular VEGF secreted by vascular/extravascular components is one of the strongest inducers of ocular angiogenesis and vascular abnormalities including choroidal neovascularization (CNV) and abnormal vascular leakage, intravitreal anti-vascular endothelial growth factor (VEGF) drugs are the standard treatment for neovascular age-related macular degeneration (AMD) (18, 192-195). Although many patients benefit from injection into the eye of anti-VEGF drugs such as such as brolucizumab (Beovu®, Novartis), aflibercept (Eylea®, Regeneron), or ranibizumab (Lucentis®, Roche/Genentech), approximately up to 30% patients suffer from incomplete to anti-VEGF therapy due to inadequate choroidal neovascularization response, progression of atrophy, and subretinal fibrosis and scar formation (44, 196, 197). As a result, more than half of patients may have vision worse than 20/40 that limit their life activities with long-term follow-up (198). Therefore, there is an unmet need for more effective therapeutic agents.

Among the several molecules that are involved in the development of ocular neovascularization (NV), platelet-derived growth factor-BB (PDGF-BB) is the predominant isoform of PDGF in the ocular system, which is primarily expressed on vascular endothelial cells (104, 105, 199), and PDGF receptor β (PDGFRβ) is commonly expressed on pericytes, smooth muscle cells, vascular endothelial cells, and retinal pigment epithelium (RPE) (200-202). The ligand/receptor pair of PDGF-BB/PDGFRβ not only induces the recruitment of pericytes to neovessels, which then cover these vessels (203) but also the secretion of VEGF and other cell survival factors from pericytes (105, 118, 121). These protective functions of pericytes enable endothelial cell survival independent of VEGF, rendering anti-VEGF therapy less efficient (119, 204-206).

In the laser-induced CNV animal model which is the most implemented method in multiple species to study neovascular AMD, laser injury promotes the recruitment of pericyte-like cells into the CNV lesions and induces their proliferation, leading to the expression of markers such as smooth muscle actin and PDGFRβ (207, 208). These infiltrated pericyte-like cells form a scaffold for subsequent vascular endothelial cell infiltration to complete the NV process (126). In this animal model, PDGF-BB/PDGFRβ signaling inhibitors have

demonstrated additive benefits for suppressing CNV when employed in combination with anti-VEGF agents (125, 126). However, in the human studies, PDGF and PDGFRβ targeting medications in CAPELLA phase 2 trial with rinucumab/aflibercept combination as well as in phase 3 trial investigating the efficacy of E10030 and ranibizumab combination, have not provided visual or anatomical advantages in combination with anti-VEGF agents over anti-VEGF monotherapy.

There is no clear reason to explain these failures. However, previous studies reported an inverse correlation between concentrations of PDGF/PDGFRβ and VEGF during anti-VEGF treatments (22, 209, 210) as well as excessive coverage of PDGFRβ-positive cells in CNV lesions of patients resistant to anti-VEGF therapy (211). Thus, we hypothesized that therapy combining PDGF/PDGFRβ signaling inhibitors with anti-VEGF drugs is insufficient to ablate pericytes and inhibit the PDGF/PDGFRβ-related signaling pathway in the pathologic ocular environment.

Antibody-drug conjugates (ADCs) are monoclonal antibodies linked to cytotoxic effector molecules that induce cell death upon binding and internalization of antibody by the target cell. In the current study, we tested whether specific delivery of ADCs targeting PDGFRβ could ablate pericytes and effectively in reduce pathologic CNV in the laser-induced CNV mouse model. ADC targeting PDGFRβ effectively removed PDGFRβ-expressing pericytes and led to the suppression of CNV lesions, with no visible signs of anatomical and functional toxicity.

MATERIALS AND METHODS

1. Mice

C57BL/6J mice were maintained in a specific pathogen-free facility at Seoul National University. The mice (aging-matched: 6- week-old, weight range: 20–24 g) were allocated into experimental groups. The total number of mice used in each experiment was determined based on the preliminary result of the LI-CNV mouse study using ADC. No statistical methods were used to predetermine sample size. All animal procedures were approved by the Seoul National University Animal Care and Use Committee (Permit Number: SNU-171203-1-2) and were conducted following the guidelines of the Association for Research in Vision and Ophthalmology Statement for the use of Animals in Ophthalmic and Vision Research.

2. Immunofluorescence staining

The eyes were enucleated and fixed with 4% paraformaldehyde (#P2031; Biosesang, Seongnam, Gyeonggi-do, Korea) for 15 minutes at room temperature (RT). After washing with PBS, the eyes were gently dissected to remove all components except the RPE-choroid- scleral (RCS) complexes. The RCS complexes were whole mounted and incubated in Perm/Block solution (0.2% Triton X-100 and 0.3% BSA in PBS) at room temperature for 1 hour. Next, the samples were incubated overnight at 4°C with rabbit anti-PDGFRβ antibody (1:100; #3169, Cell Signaling Technology, Danvers, MA, USA). After washing with PBS, the samples were incubated at room temperature for 2 hours with Alexa Fluor 647- labeled donkey anti-rabbit IgG antibody (1:400; #A31573; Invitrogen, Carlsbad, CA, USA). After washing with PBS, the samples were stained with Alexa Fluor 568-conjugated anti-IB4 antibody (1:400; #I21412; Invitrogen, Carlsbad, CA, USA) and Alexa Fluor 488-conjugated anti-NG2 antibody (1:400; #AB5320A4; Sigma- Aldrich, St. Louis, MO, USA) at room temperature for 2 hours. After washing with PBS, the samples were counterstained with 10 mg/ ml of DAPI (1:1000; #D9542; Sigma-Aldrich, St. Louis, MO, USA) at room temperature for 15 minutes. After washing with PBS, the retina and RCS complexes were mounted with Fluoromount™ Aqueous Mounting Medium (#F4680, Sigma-Aldrich, St. Quentin, France) and observed under a confocal microscope (Leica TCS STED; Leica Microsystems Ltd., Wetzlar, Germany).

3. Induction of laser-induced choroidal neovascularization

Six-week-old wildtype C57BL/6J male mice (n = 6 per group, n = 18 in total) were fully anesthetized by intraperitoneal injection using a mixture (3:1 ratio, 1 mL/kg) of zolazepam and

tiletamine (Zoletil 50®, Virbac, Carros, France) and xylazine (Rompun®, Bayer Korea, Seoul, Korea). After dilating the pupils with tropicamide 1% (Tropherin®, Hanmi. Pharm Co. Ltd., Seoul, Korea), a laser photocoagulator with an indirect headset delivery system (Ilooda, Suwon, Gyeonggi-do, Korea) was used to visualize the retina. The laser parameters were as follows: wavelength: 810 nm; spot size: 200 μm; power: 1W; and exposure time: 100 msec. Sufficient laser energy was delivered to four locations for each eye (the 3, 6, 9, and 12 o'clock positions of the posterior pole around the optic disc) to induce rupture of Bruch's membrane. Only burns that produced a bubble without vitreous hemorrhage were included in the study. The mice were then divided into three groups (six mice per group). On day 7 after laser photocoagulation, the six mice in each group received an intravitreal injection of PBS as a vehicle control, control ADC (667.7 pg), and ADC targeting mPDGFRβ (667.7 pg). To evaluate the effect of ADC on choroidal neovascularization, the eyes were enucleated, fixed in 4% paraformaldehyde, and then prepared for whole-mounted RCS complex formation. After immunofluorescence staining described above, CNV area and volume, NG2 volume, and PDGFRβ volume of all the laser burn sites (four laser burn sites for each eye) were quantitatively analyzed using a built-in measuring tool, the LAS X systems (Leica Microsystems Ltd., Wetzlar, Germany).

4. Preparation of bispecific scFv-Cκ-scFv fusion protein and ADC targeting mPDGFRβ

Anti-mPDGFRβ × cotinine was expressed and purified as described previously (109). Clone PRb-CN01 developed in our previous study was used for anti-mPDGFRβ scFv. As a control, we also prepared anti-HER2 × cotinine, where anti-HER scFv was derived from trastuzumab (109). The expression vectors encoding these bispecific scFv-Cκ-scFv fusion proteins were transfected into Expi293F cells (Thermo Fisher Scientific Inc., Waltham, MA, USA), and the scFv-Cκ-scFv fusion proteins were purified using KappaSelect resin (GE Healthcare, Buckinghamshire, UK) following the manufacturer's instructions. ADC targeting mPDGFRβ was prepared by mixing anti-mPDGFRβ × cotinine (1 μM) with cotinine-duocarmycin (1 μM) at a 1:1 molar ratio as described previously (109). The complex was then incubated for 30 minutes at room temperature to allow complex formation before being used. Control ADC was prepared in the same way. The schematic diagrams of a bispecific antibody, cotinine-duocarmycin, and the

conjugation process are represented in Fig. 1.2A and B. The RP-HPLC analysis that empirically determine the drug-to-antibody ratio were performed by Levena Biopharma (San Diego, CA, USA) and the data are shown in in Fig. 1.2C.

5. Statistics and reproducibility

Statistical analyses were performed using SPSS software version 22.0 (SPSS Inc., Chicago, IL, USA) and GraphPad Prism v.8.0.1. The experimental data were presented as mean ± standard error of the mean. P values were determined using one-way ANOVA and Tukey post-hoc tests for multiple groups. All the data in our manuscript were repeated at least three times independently with similar results. The experiments were not randomized, and the investigators were not blinded to allocation during experiments and outcome assessment.

RESULTS

PDGFRβ is highly expressed on pericytes in pathologic neovessels of LI-CNV mouse model.

To evaluate the expression patterns of PDGFRβ in retinal pigment epithelium (RPE) of laser-induced choroidal neovascularization (LI-CNV) mouse model, eyeballs were retrieved after inducing choroidal neovascularization (CNV). The whole mounted RPE in wild-type mice and LI-CNV mice was stained with anti-PDGFRβ, IB4, or NG2 antibodies. The CNV lesion showed highly increased levels of PDGFRβ, compared with control RPE (Fig. 2.1A and B). The pericyte marker NG2 was dramatically co-localized with PDGFRβ in the CNV lesion, confirming that PDGFRβ was mainly expressed by pericytes.

ADC targeting mPDGFRβ significantly suppresses CNV in LI-CNV mouse model and shows no anatomical functional toxicity in retina.

As the CNV lesion of LI-CNV mouse model is quite variable depending on operators and consistent laser scar formation requires meticulous hand-eye-foot coordination skills to operate laser (212, 213), we first evaluated the CNV size pattern at different times after laser induction. We confirmed that the optimum time point to assess CNV formation in our laser setting is at day 7 or day 10 after laser induction (Fig. 2.2).

In LI-CNV mouse model, laser photocoagulation was performed to induce CNV. Seven days later, ADC targeting mPDGFRβ (667.7 pg) was intravitreally injected into mice. In parallel experiments, PBS, or control ADC (667.7 PG) were intravitreally injected. At ten days after laser photocoagulation, RPE-choroid-sclera (RCS) complexes were retrieved from the mice and stained with anti-IB4, anti-PDGFRβ, or anti-neural/glial antigen 2 (NG2) antibodies (Fig. 2.3A). The volume and area of CNV and the volume of NG2- and PDGFRβ-positive tissue were remarkably decreased in mice treated with ADC targeting mPDGFRβ (Fig. 2.3B and C). In the retinal toxicity test of ADC, ADC targeting PDGFRβ did not induce anatomical or functional abnormalities of the retina at the therapeutic dose (Fig 1.7).

ADC targeting mPDGFRβ in combination with anti-VEGF agent shows additional benefit in the suppression of CNV in LI-CNV mouse model.

To evaluate additional anatomical benefit of ADC targeting mPDGFRβ in combination with conventional anti-vascular endothelial growth factor (VEGF) agent in wet-type AMD (aflibercept, EYLEA®; BAYER AG, Leverkusen, Germany) over aflibercept alone in LI-CNV mouse model, ADC targeting mPDGFRβ (667.7 pg) alone, ADC targeting mPDGFRβ (667.7

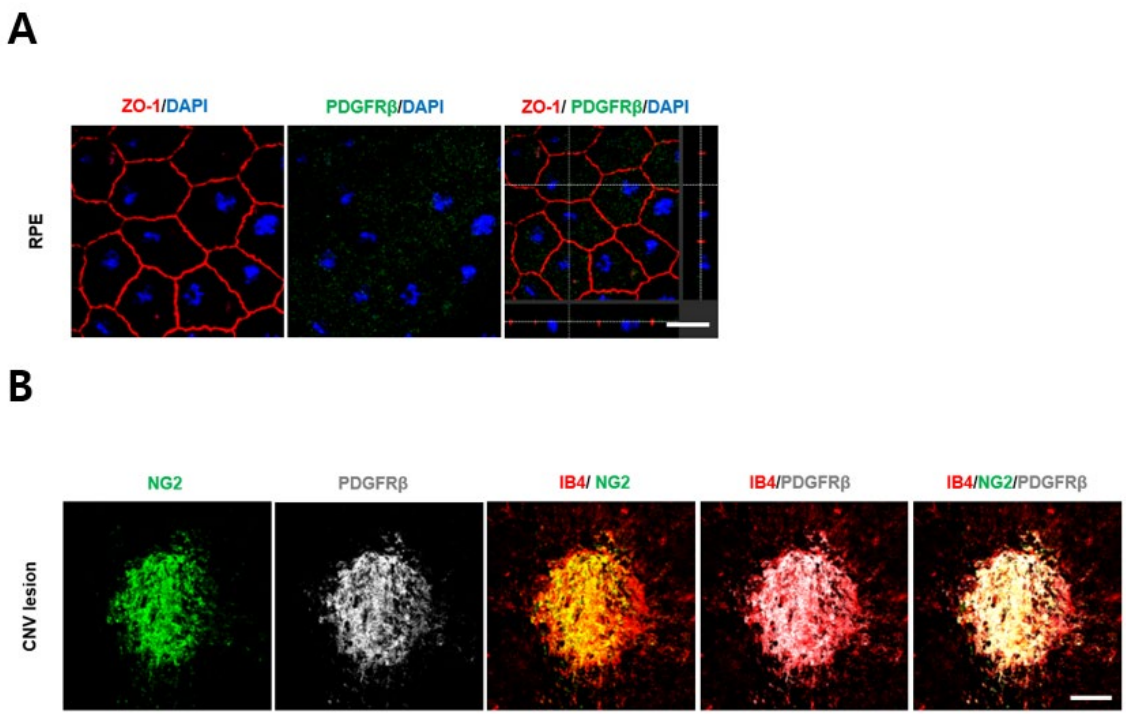

Figure 2.1. PDGFRβ is highly expressed on pericytes in pathologic neovessels of LI-CNV mouse model.

(A) Representative immunofluorescence images of the retinal pigment epithelium (RPE) in a wild-type (control) mouse. Immunofluorescence images of anti-platelet-derived growth factor receptor β (PDGFRβ, green), zonular occludens-1 (ZO-1, red), and 4'6'-diamidino-2-phenylindole (DAPI, blue). Scale bar, 20 μm

(B) Representative immunofluorescence images of the RPE in LI-CNV mouse. Immunofluorescence images of anti-neural/glial antigen 2 (NG2, green), anti-isolectin B4 (IB4, red), and anti-PDGFRβ (PDGFRβ, gray). The CNV lesion in the LI-CNV mouse shows strong PDGFRβ expression. Scale bar, 200 μm

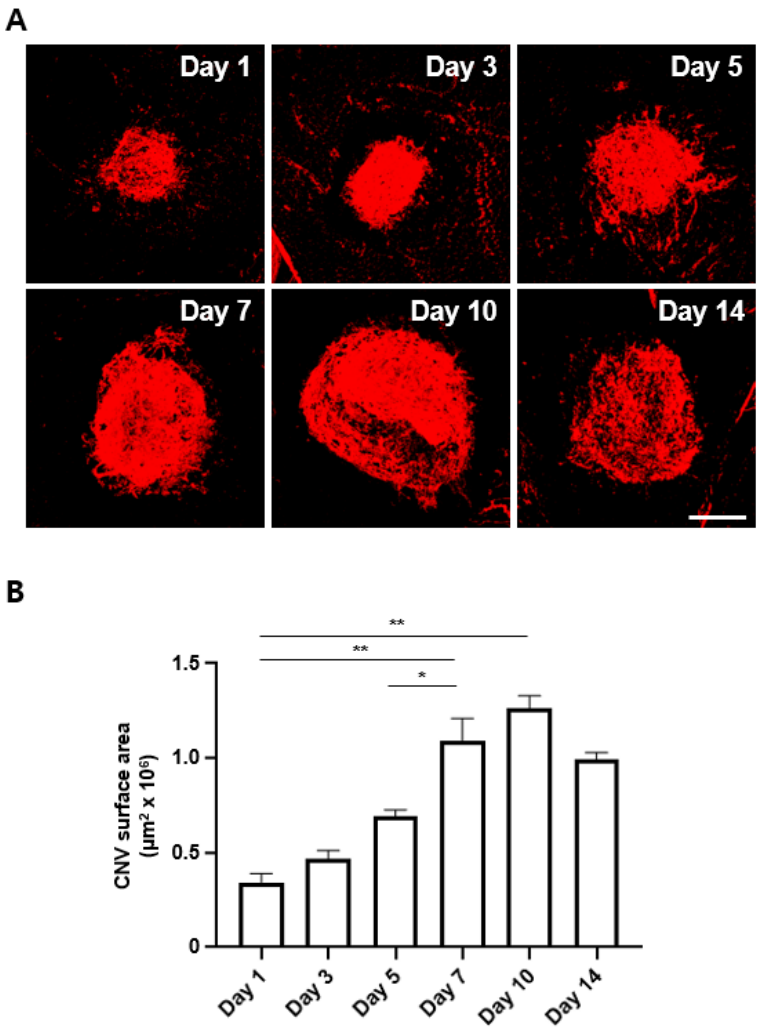

Figure 2.2. IB4+ labeled choroidal neovascularization at different times after laser induction.

(A) Representative immunofluorescence images of isolectin B4 (IB4) positive labeled choroidal neovascularization (CNV) at day 1 to day 14 in laser-induced CNV mouse model. The laser photocoagulation was performed on 6-week-old wild-type C57BL/6J male mice, rupturing Bruch's membrane (the innermost later of the choroid) to induce CNV. Scale bar, 200 μm

(B) Quantification of the surface area of IB4+ CNV. All quantitative data were measured using the built-in tools, the LAS X systems (Leica Microsystems, Wetzlar, Germany). Error bars represent standard error mean (SEM, n =6 mice for each data set). *$P < 0.01$, **$P < 0.001$, obtained using one-way ANOVA and Tukey's post-hoc tests.

compared with mice injected with vehicle control or control ADC (P-value < 0.01, Fig 2.3B and C).

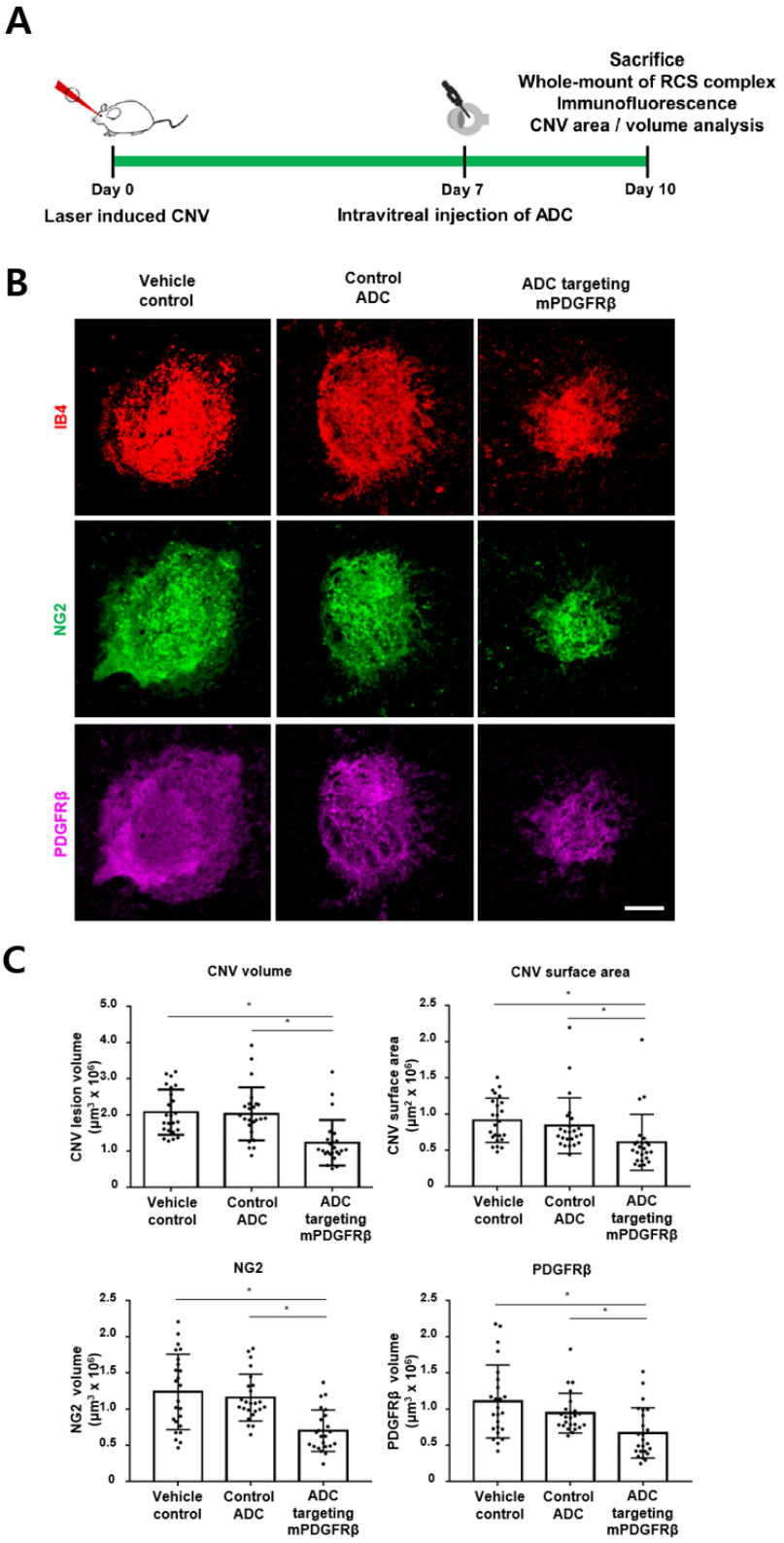

Figure 2.3. ADC targeting mPDGFRβ effectively inhibits LI-CNV.

(A) Schematic experimental timeline of the laser-induced choroidal neovascularization (LI-CNV) mouse model. Six-week-old wild-type C57BL/6J male mice received laser photocoagulation and were treated with vehicle control, control antibody-drug conjugate (ADC), or ADC targeting mouse platelet-derived growth factor receptor β (mPDGFRβ) through

intravitreal injection at seven days after laser photocoagulation. Phosphate-buffered saline was used as the vehicle control. Anti-human epidermal growth factor receptor 2 (HER2) x cotinine complexed with cotinine-duocarmycin was used as a control ADC; anti-HER2 single-chain variable fragment (scFv) was derived from trastuzumab.

(B) Representative immunofluorescence images of CNV at ten days after laser photocoagulation and immunostaining with anti-isolectin B4 (IB4, red), anti-neural/glial antigen 2 (NG2, green), and anti-PDGFRβ (pink). Scale bar, 200 μm.

(C) Quantitation of CNV volume, CNV area, NG2 volume, and PDGFRβ volume. All quantitative data were measured using the built-in tools, the LAS X systems (Leica Microsystems, Wetzlar, Germany). Each value represents the mean ± standard error mean (SEM, n = 6 mice for each group set). *$P < 0.01$, obtained using one-way analysis of variance (ANOVA) and Tukey's post-hoc tests.

pg) with aflibercept (2 μg), aflibercept alone were intravitreally injected into mice. In parallel experiments, vehicle control was intravitreally injected. Interestingly, the combination treatment of ADC targeting mPDGFRβ with aflibercept were superior to monotherapy for the decrease of the CNV volume, CNV area, NG2 volume, and PDGFRβ volume (*P*-value < 0.01, Fig 2.4).

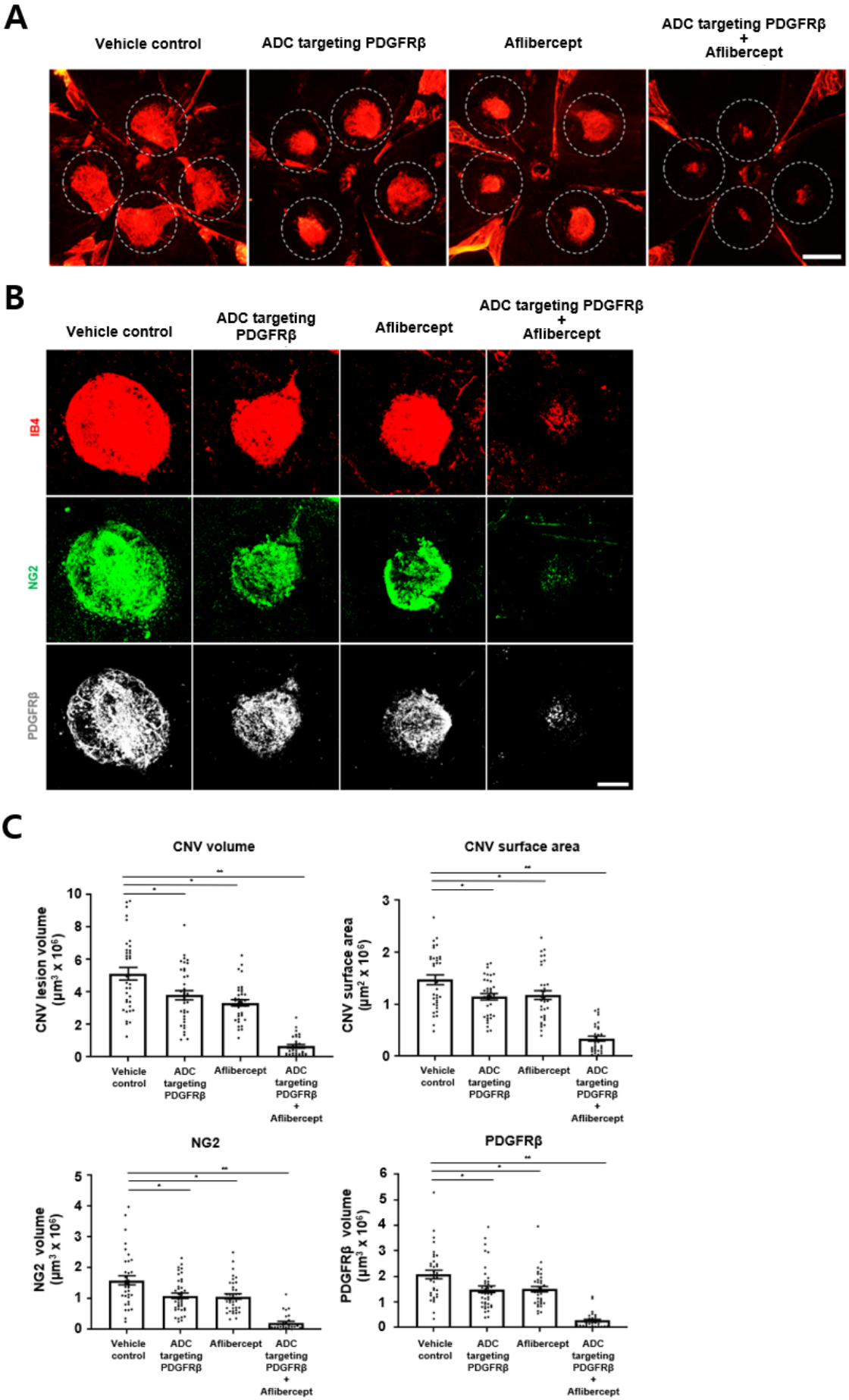
A
Vehicle control
ADC targeting PDGFRβ
Aflibercept
ADC targeting PDGFRβ + Aflibercept
B
Vehicle control
ADC targeting PDGFRβ
Aflibercept
ADC targeting PDGFRβ + Aflibercept
IB4
NG2
PDGFRβ
C
CNV volume
CNV lesion volume (μm³ x 10⁶)
CNV surface area
CNV surface area (μm² x 10⁶)
NG2
NG2 volume (μm³ x 10⁶)
PDGFRβ
PDGFRβ volume (μm³ x 10⁶)
Vehicle control
ADC targeting PDGFRβ
Aflibercept
ADC targeting PDGFRβ + Aflibercept

Figure 2.4. The combination treatment of ADC targeting mPDGFRβ with aflibercept shows additional benefit in the suppression of CNV in LI-CNV mouse model.

(A) Representative immunofluorescence images of retinal pigment epithelium-choroid-sclera (RCS) complex stained with isolectin B4 (IB4) to visualize choroidal neovascularization (CNV) at ten days after laser photocoagulation. Scale bar, 500 μm.

(B) Representative immunofluorescence images of CNV at ten days after laser photocoagulation and immunostaining with anti-IB4 (red), anti-neural/glial antigen 2 (NG2, green), and anti-platelet-derived growth factor receptor β (PDGFRβ, gray). Scale bar, 200 μm.

(C) Quantitation of CNV volume, CNV area, NG2 volume, and PDGFRβ volume. Each value represents the mean ± standard error mean (SEM, n = 8-10 mice for each group set). $^{*}P < 0.01$, $^{**}P < 0.001$ obtained using one-way analysis of variance (ANOVA) and Tukey's post-hoc tests.

DISCUSSION

Anti-VEGF drugs are standard therapeutics for neovascular AMD. Recently, new research has been bringing longer lasting anti-VEGF drugs, like brolucizumab (214, 215), and anti-VEGF gene therapy (216-218) such as RGX-314 (phase 2, Regenxbio) that produces ranibizumab following either subretinal or suprachoroidal injection, ADVM-022 (phase 1, Averum Biotechnologies) that produces aflibercept following intravitreal injection, which could enable the anti-VEGF effect to last longer, so patients may not need to have frequent injections. However, repeated intravitreal injection of anti-VEGF agents to reduce intraocular VEGF levels lead to intraocular complications, such as vitreous hemorrhage, fibrosis, inflammation, and atrophy of the retina and choroid (44, 196, 219). Therefore, there are still unmet needs for the development of novel therapeutics for neovascular AMD.

In the eye, PDGFs has been reported to be another imperative pro-angiogenic factors involved in choroidal and retinal NV via activation of the tyrosine kinase receptors, PDGFRs in both VEGF-dependent and -independent manners (220, 221). Some studies have reported that patients who respond poorly to anti-VEGF therapy have elevated levels of PDGFs/PDGFRs indicating the alternative pro-angiogenic effect of the PDGFs/PDGFRs axis (22, 209, 210, 222). Other study described excessive coverage of PDGFRβ-positive cells in the NV region in LI-CNV (126). Furthermore, in a patient with bilateral CNV, the neovascular membrane of the eye unresponsive to bevacizumab exhibited increased numbers of pericytes, whereas the eye that responded to treatment had a limited number of these cells (211). These findings suggest that inhibition of PDGFs/PDGFRs might be a promising therapy for suppressing angiogenesis, either alone or in combination with anti-VEGF therapy.

In preclinical studies, pegpleranib, an aptamer that binds to PDGF-AB and PDGF-BB and inhibits their interaction with PDGFRα and PDGFRβ, showed efficacy in inhibiting CNV (126), and an anti-PDGFRβ antibody, rinucumab, also inhibited mouse CNV. However, neither pegpleranib nor rinucumab have exhibited additive therapeutic effects when used in combination with anti-VEGF agents in clinical trials(127). A few small-molecule tyrosine kinase inhibitors of both VEGF and PDGF receptors, including DE-120 and vorolanib, have

been tested clinically. However, none of these agents are unavailable due to failure to improve the pathologic anatomy of the retina and choroid or enhance visual acuity. We hypothesized that therapy combining PDGF/PDGFR signaling inhibitors with anti-VEGF agents is not enough to ablate pericytes and inhibit the PDGF/PDGFR-related pro-angiogenic effect in the pathologic ocular environment. In the current study, we considered the use of ADC that specificically deliver the cytotoxic reagents to PDGFRβ-overexpressing cells for reducing pathologic ocular NV.

To date, nine ADCs targeting HER2, CD22, CD30, CD33, CD79B, Nectin-4, and Trop-2 are clinically available for the treatment of HER2-positive metastatic breast cancer, B-cell acute lymphoblastic leukemia, Hodgkin's lymphoma, acute myeloid leukemia, B-cell lymphoma, bladder cancer, and triple-negative breast cancer, respectively (223). However, until now, ADCs have rarely been evaluated outside oncologic applications, although a few studies have reported such uses of ADCs (224, 225). For ADC to be effective and to be avoided toxicity, a sufficient number of target antigens should be present on the target cell surface, compared with normal cells (128, 129). PDGFRβ was significantly overexpressed in the choroidal NV region, compared with the control RPE in LI-CNV mouse model (Fig. 2.1). Based on this observation, we evaluated whether ADC targeting PDGFRβ induces cytotoxicity specifically toward pericytes of neovessels and inhibit choroidal NV.

We first confirmed that ADC targeting mPDGFRβ effectively internalized and killed MBVP cells. Furthermore, ADC targeting mPDGFRβ did not compete with PDGF-BB under the typical ocular NV environment, which is increased PDGF-BB levels but did induce cytotoxicity independent of PDGF-BB (Fig. 1.4). Thereafter, we established the LI-CNV mouse model and confirmed that ADC targeting mPDGFRβ suppressed the CNV lesions (Fig. 2.3). Interestingly, we also found that the combination treatment of ADC targeting mPDGFRβ with aflibercept was superior to monotherapy for the decrease of the CNV volume, CNV area, NG2 volume, and PDGFRβ volume (Fig 2.4).

Regarding the systemic clearance of ADC targeting mPDGFRβ, the in vivo half-life of the anti-cotinine antibody and cotinine-conjugate complex was 15 hours when injected intravenously (226) and that of scFv-C_{κ}-scFv molecule was approximately 6 hours. It was

reported that ranibizumab (48 kDa) with a half-life of 2.88 days showed faster penetration and elimination from retina than bevacizumab (149 kDa) with a half-life of 4.32 days due to smaller size (227). Because the molecular weight of the cotinine-duocarmycin conjugate is 6.27 kDa, it would be rapidly excreted through the kidney after being released from anti-mPDGFRβ × cotinine. We selected cotinine as a hapten to conjugate duocarmycin because of its non-toxic nature, with its absence in physiologic situations and relative pharmacologic inertness (228) as well as a median lethal dose of 4 ± 0.1 g/kg in mice (229). In conclusion, PDGFRβ-overexpressing pericytes ablation with ADC effectively inhibited pathologic CNV in LI-CNV mouse model. At the therapeutic dose, ADC targeting PDGFRβ did not induce anatomical or functional toxicity in the retina and cause systemic or behavioral toxicity. We believe that ADC targeting PDGFRβ can be a therapeutic option for CNV after repeated clinical failures of PDGF/PDGFR signaling inhibitors.

CHAPTER 2-2

Regulation of Epithelial-Mesenchymal Transition in Age-Related Macular Degeneration via Intravitreal AICAR or GKT137831 Injection

INTRODUCTION

The retinal pigment epithelium (RPE) consists of a homogeneous single layer of hexagonal cells, which are considered to have a typical epithelial cell morphology. RPE cells are highly polarized with apical to basal/basolateral characteristics, which are supported by the cytoskeleton and connection of the extracellular matrix (ECM) to the RPE (230). This strong connection between the intracellular cytoskeleton and the ECM is important for maintaining the morphology and polarity of the RPE. Accumulating evidence has confirmed that cytoskeleton derangement such as fragmentation or reorganization of F-actin, results in stress fiber formations in the cytosol, which correlate with poor physiologic function in RPE cells (231-233).

In the aging process or pathological conditions, structural and functional alterations in RPE cells occur, including morphometric changes (231, 234, 235), epithelial-mesenchymal transition (EMT) (236, 237), decrease in antioxidant capacity (238), and secretomal change (160). Representative morphometric alterations include an increase in cell area, a decrease in cell density, and loss of hexagonality. Morphometric changes and EMT, which is a switch to a mesenchymal phenotype with cytoskeleton rearrangement have been observed not only in senescent RPE, but also in retinal diseases such as age-related macular degeneration (AMD), diabetic retinopathy, and proliferative vitreoretinopathy (230, 239, 240).

Transforming growth factor-beta (TGF-β) signaling plays an important role as a senescence-promoting factor in both normal aging and age-related diseases (241, 242). Increased TGF-β expression and oxidative stress due to metabolic burden can induce EMT (236, 237, 239) and degenerative changes in the RPE, such as neovascularization (243-245), atrophy of the choriocapillaris (246) linked with AMD. In vitro experiments have been conducted to examine the EMT of TGF-β1 or TGF-β2 in RPE cells (247-251). Among TGF-β-related signal regulators, mammalian target of rapamycin C1 (mTORC1) and NADPH oxidase (NOX) have been reported to be involved in cellular senescence and EMT (252, 253). However, few studies have investigated age-related morphometric changes and the EMT of the RPE *in vivo*.

In this study, we investigated whether intravitreal injection of TGF-β1 induces morphometric changes and EMT observed during the process of normal aging and AMD of the

RPE. We also examined how these processes are affected by the suppression of the mTORC1-NOX- ROS pathway using an AMP-dependent protein kinase (AMPK) activator or a NOX1/4 inhibitor.

MATERIALS AND METHODS

1. Mice

Six-week-old C57BL/6J male mice were maintained in a specific pathogen-free facility at Seoul National University. The mice were allocated into experimental groups. All animal experiments in this study were conducted in strict agreement with by the guidelines of the Association for Research in Vision and Ophthalmology Statement for the use of Animals in Ophthalmic and Vision Research (Permit Number: SNU-190814-2-1).

2. Intravitreal injection

The mice were fully anesthetized by intraperitoneal injection using the mixture (3:1 ratio, 1 mL/kg) of the zolazepam and tiletamine (Zoletil 50, Virbac, Carros, France) and xylazine (Rompun, Bayer Korea, Seoul, Korea) and pupils were dilated with tropicamide 1% (Tropherin, Hanmi. Pharm Co. Ltd., Seoul, Korea). Then, microliter syringe with 33 gauge blunt needle (Hamilton Bonaduz AG, Bonaduz, Switzerland) was inserted into the vitreous cavity through 6 o'clock position of the limbus with a 45° injection angle for right eye followed by gently loading each reagent under the surgical microscope (Leica Microsystems, Ltd., Wetzlar, Germany). Intravitreal injection was only conducted in the right eye.

3. Immunofluorescence of RPE tissue

For the immunofluorescence staining of the RPE tissue, C57BL/6J mice were sacrificed 3 days after intravitreal injection of PBS in the control group and recombinant mouse TGF-β1 (200 ng/eye, #7666-MB- 005/ CF, R&D Systems), AICAR (500 μM/eye, #A9978, Sigma-Aldrich), and GKT137831 (50 μM/eye, #17764, Cayman Chemical) in the experiment group. The eyes were enucleated and fixed by 4% of paraformaldehyde (#P2031, Biosesang, Seongnam, Korea) for 15 minutes at room temperature (RT). After washing with the PBS, eyes were gently dissected to remove all the components except RPE-choroid- scleral (RCS) complexes. The RCS complexes were whole-mounted and incubated in Perm/ Block solution (0.2% Triton-X 100 and 0.3% BSA in PBS) at room temperature for 1 hour Then, it was incubated overnight at 4°C with primary antibodies against rabbit anti-zonula occludens (ZO)-1 (1:100, #61-7300,

Invitrogen) and mouse anti-alpha- smooth muscle actin (α-SMA) (1:100, #ab18460-1, Abcam). After washing with PBS, it was incubated at room temperature for 2 hours with secondary antibodies (1:400, Alexa fluor 594 donkey anti-rabbit IgG; #A11012, Invitrogen, 1:400, Alex Fluor 647 donkey anti-mouse IgG; #A31571, Invitrogen). After washing with PBS, it was stained with Alexa fluor 488-conjugated phalloidin (1:200, #A12379, Invitrogen) at room temperature for 2 hours After washing with PBS, it was counterstained with 10 mg/ mL 4´6-diamidino- 2- phenylindole dihydrochloride (DAPI) (1:1000, #D9542, Sigma-Aldrich) at room temperature for 15 minutes. After washing with PBS, the RCS complexes were mounted with Fluoromount Aqueous Mounting Medium (#F4680, Sigma Aldrich) and observed under a confocal microscope (Leica TCS STED, Leica Microsystem Ltd.).

4. Western blotting of RPE-choroid-scleral (RCS) complexes

For the western blot analysis, the RCS complexes isolated from enucleated eyes were put into microcentrifuge tubes and lysed with RIPA buffer (50 mM Tris-HCl, 150 mM NaCl, 1% Triton X-100, 1% sodium deoxycholic acid, 0.1% SDS containing complete protease, and phosphatase inhibitor cocktails). The tubes were centrifuged (15 000 rpm, 20 minutes) to obtain supernatants following sonication. Equal amounts of protein lysates (20 μg) were separated by electrophoresis on 6%-10% of SDS-PAGE for 2 hours and transferred to nitrocellulose membranes for 1 hour After blocking in 5% of BSA in TBST for 30 minutes, the membranes were incubated overnight at 4°C with primary antibodies for ZO-1 (1:1000, #8193, Cell Signaling Technology), E-cadherin (1:1000, #3195, Cell Signaling Technology), α-SMA (1:1000, #ab5694, Abcam), and GAPDH (1:1000, #sc-25778, Santa Cruz Biotechnology Inc). Then, the membranes were incubated with the respective secondary antibodies (1:5000, anti-rabbit IgG-HRP conjugate; #31460, Thermo Fisher Scientific, 1:5000, anti-mouse IgG-HRP conjugate; #31450, Thermo Fisher Scientific) for 2 hours at room temperature. The membranes were incubated with chemiluminescent substrates (#34580, Thermo Fisher Scientific) and exposed in ImageQuant LAS 4000 (GE Healthcare Life Sciences). The relative band intensity was quantified using ImageJ 1.42 software (National Institutes of Health, Bethesda, MD, USA).

5. Cell culture

Adult retinal pigment epithelial cell line-19 (ARPE-19) cells were obtained from American Type Cell Culture (ATCC; CRL2302) and maintained in DMEM/F-12 medium (a mixture of Dulbecco's modified Eagle's minimum essential medium and Hank's Balanced salt solution, HyClone, Thermo Fisher Scientific) supplemented with 10% of fetal bovine serum (FBS, Gibco, Thermo Fisher Scientific), 100 U/ml of penicillin, and 100 μg/mL of streptomycin (HyClone).

6. Immunocytochemistry of APRE-19 cells

ARPE-19 cells grown on 18 mm coverslips were washed twice with PBS and fixed with 4% of paraformaldehyde for 15 minutes at 37℃. Next, cells were permeabilized with 0.25% of Triton X-100 for 5 minutes and blocked with 1% of BSA in PBS for 30 minutes. Incubation with antibodies for Alexa fluor 488-conjugated phalloidin (1:100, #A12379, Invitrogen) or ZO-1 (1:50, #61-7300, Invitrogen), α-SMA (1:100, #ab18460- 1, Abcam) was performed overnight at 4℃ followed by incubation with secondary antibody for 1 hour at room temperature in a dark room. Cells were washed and counterstained with 1 μg/mL DAPI for 5 minutes. Fluorescence images were obtained using a laser scanning confocal microscope (LSM800, Zeiss).

7. Western blotting of ARPE-19 cells

Western blot analysis was performed using following antibodies: anti-TGFβ (1:250, #MAB1835, R&D Systems), anti-phospho-ERK1/2 (1:1000, #4370, Cell Signaling Technology), anti-ERK1/2 (1:1000, #9102, Cell Signaling Technology), anti-phospho- 70S6K (1:1000, #9205, Cell Signaling Technology), anti-70S6K (1:1000, #9202, Cell Signaling Technology), anti-phospho-Smad3 (1:1000, #9520, Cell Signaling Technology), anti-Smad3 (1:1000, #9523, Cell Signaling Technology), anti-α- SMA (1:1000, #ab5694, Abcam), anti-Col1α1 (1:1000, #PA5-29569, Thermo Fisher Scientific), anti-PAI- 1 (1:1000, #PA5-27216, Thermo Fisher Scientific), anti-ZO- 1 (1:1000, #8193, Cell Signaling Technology), anti-E-cadherin (1:1000, #3195, Cell Signaling Technology), anti-GAPDH (1:1000, #sc-25778, Santa Cruz Biotechnology Inc), anti-rabbit IgG-HRP conjugate (1:5000, #31460, Thermo Fisher Scientific), and anti-mouse IgG-

HRP conjugate (1:5000, #31450, Thermo Fisher Scientific). Protein intensity was quantified using ImageJ 1.42 software (National Institutes of Health, Bethesda, MD, USA).

8. Measurement of ROS

ROS generation was detected by chloromethyl-H2-dichlorofluorescein diacetate (CM-H2DCF-DA), which is rapidly oxidized to highly fluorescent 2,7-dichlorofluorescein (DCF) by intracellular ROS. In brief, cultured ARPE-19 cells were treated with 5 μM working concentration of CM-H2DCF- DA for 20 minutes at 37°C and rinsed with Krebs-Ringer bicarbonate (KRB) solution (135 mM NaCl, 3.6 mM KCl, 2 mM NaHCO3, 0.5 mM NaH2PO4, 0.5 mM MgSO4, 1.5 mM CaCl2, and 10 mM HEPES; pH 7.4). Fluorescence images (excitation/emission: 490/535 nm) were captured using microscopy (IX81, Olympus) and the intensity was analyzed by Metamorph 6.1 software (Molecular Devices, Sunnyvale, CA).

9. Statistics

Statistical analyses were performed using SPSS software version 22.0 (SPSS Inc, Chicago, IL, USA). Experimental data were presented as mean ± standard error of the mean. P values were determined by the Mann-Whitney U test, Student's t tests or one-way ANOVA and Tukey's post hoc tests for multiple groups.

RESULTS

Intravitreal injection of TGF-β1 induces morphometric changes and EMT of the RPE.

To evaluate whether TGF-β1 induces structural changes of the RPE observed in aged RPE, we intravitreally injected TGF-β1 or PBS into mouse eyeballs. The TGF-β1 injected RPE showed typical stress fibers of F-actin, a specific finding for epithelial-mesenchymal transition (EMT) three days after injection (Fig. 2.5A). TGF-β1 injected RPE also induces loss of ZO-1 and increase of alpha-smooth muscle actin (α-SMA) (Fig. 2.5B and C).

Next, we examined senescence-like morphological alterations in the RPE in response to intravitreal TGF-β1 treatment by analyzing confocal microscopy images. The average cell area (361.12 ± 354.19 μm^2) and its coefficient of variation (CV, 82.14% ± 9.23%) in the TGF-β1-treated RPE were higher than those of the PBS-treated control (224.79 ± 64.05 μm^2, 26.39% ± 5.78%; Fig. 2.6A). Furthermore, intravitreal TGF-β1 treatment also decreased cell density (1725.22 ± 176.45 cells/mm^2) of RPE compared to that of PBS-treated control (2416.67 ± 244.33 cells/mm^2; Fig. 2.6B). Taken together, these results suggest that intravitreal TGF-β1 treatment triggers EMT and morphometric changes to RPE, which are consistent with previous observations in aged RPE (231, 234, 235, 254).

TGF-β1-mTORC1-NOX-ROS pathway regulates EMT in ARPE-19 cells.

To figure out the mechanism which intravitreal TGF-β1 induces pathogenic alterations *in vivo*, we incubated human retinal pigment epithelial cell line (adult retinal pigment epithelial cell line-19, ARPE-19) with TGF-β1, and examined the expression of signaling molecules involved in EMT and fibrosis of RPE by western blot analysis. TGF-β1 treatment significantly increased endogenous TGF-β1 expression, which reflects autocrine action of TGF-β1 via a positive feedback loop. TGF-β1 treatment increased the phosphorylation of suppressor of mothers against decapentaplegic 3 (Smad3), extracellular signal-regulated kinase 1/2 (ERK 1/2), and ribosomal protein S6 kinase (p70S6K). We also observed increased expression of mesenchymal markers, α-SMA, alpha-1 type I collagen (collagen 1α1), and plasminogen activator inhibitor-1 (PAI-1), while attenuated expression of the epithelial markers, E-cadherin, and ZO-1 (Fig. 2.7A and B).

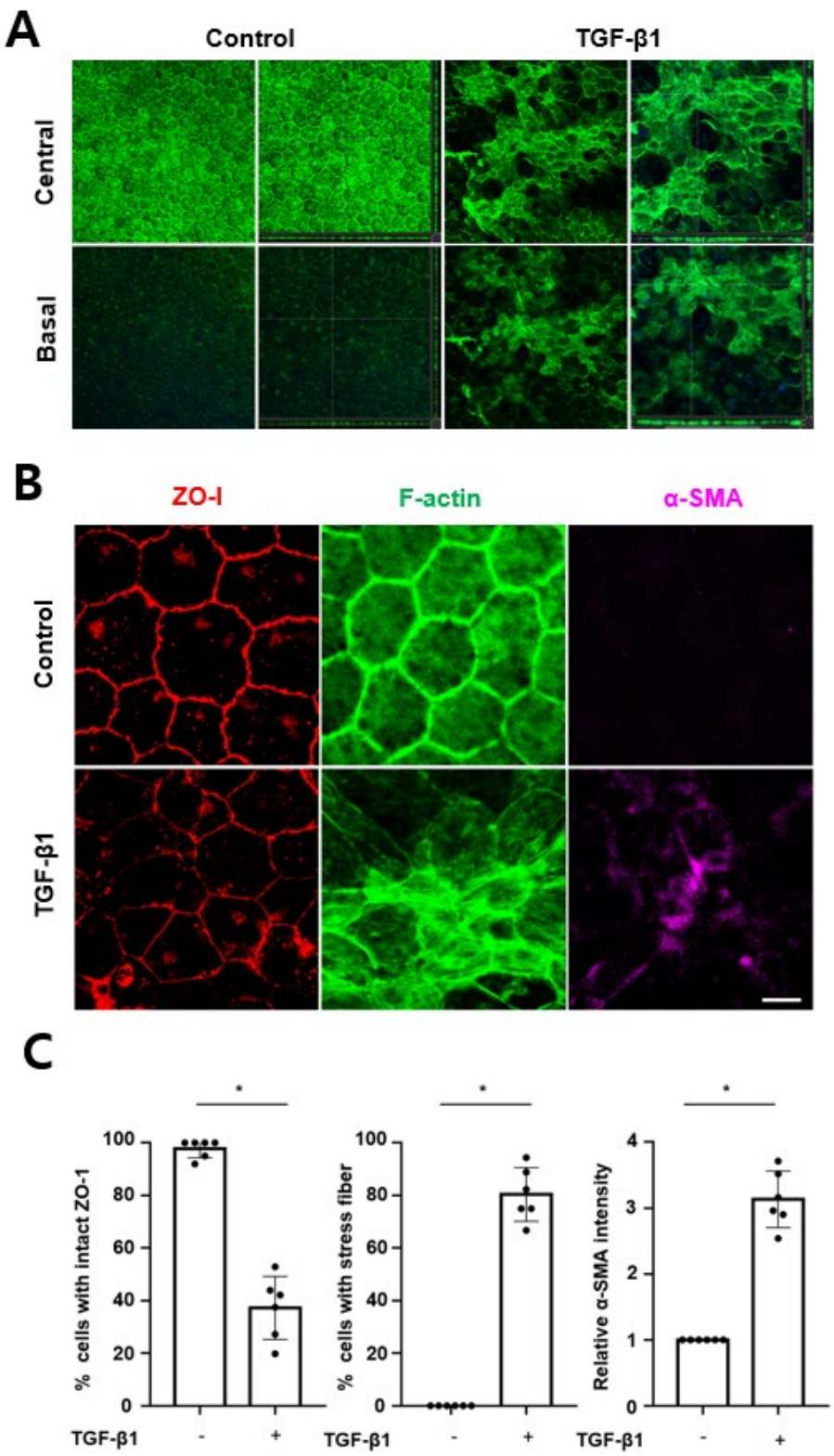

Figure 2.5. Intravitreal injection of TGF-β1 induces EMT of the RPE.

(A) Representative immunofluorescence images of retinal pigment epithelium (RPE) sheets stained with anti-F-actin (green) and 4'6'-diamidino-2-phenylindole (DAPI, blue) showing that intravitreal transforming growth factor-beta 1 (TGF-β1) injection induces formation of F-actin stress fibers of the RPE layer. Separated individual x-y (left, each group) and x-z confocal sections (right, each group) of the same field, representing the central (upper level of the

nucleus) and basal (lower level of the nucleus) aspects of the RPE. Scale bar = 50 μm.

(B) Representative immunofluorescence images of RPE sheets stained for epithelial-mesenchymal transition (EMT) markers; zonula occludens-1 (ZO-1, red), F-actin (green), alpha-smooth muscle actin (α-SMA, pink). Scale bar = 20 μm.

(C) Quantification analysis for EMT markers in RPE sheets. The bar graph shows the percentage of cells with intact ZO-1, stress fiber, and relative fluorescence intensity of the α-SMA in the RPE. All quantitative data were analyzed with NIH ImageJ software, and each value represents the mean ± standard error of the mean (SEM) (n = 6 mice for each data set). $*P < 0.01$ by Student's t test.

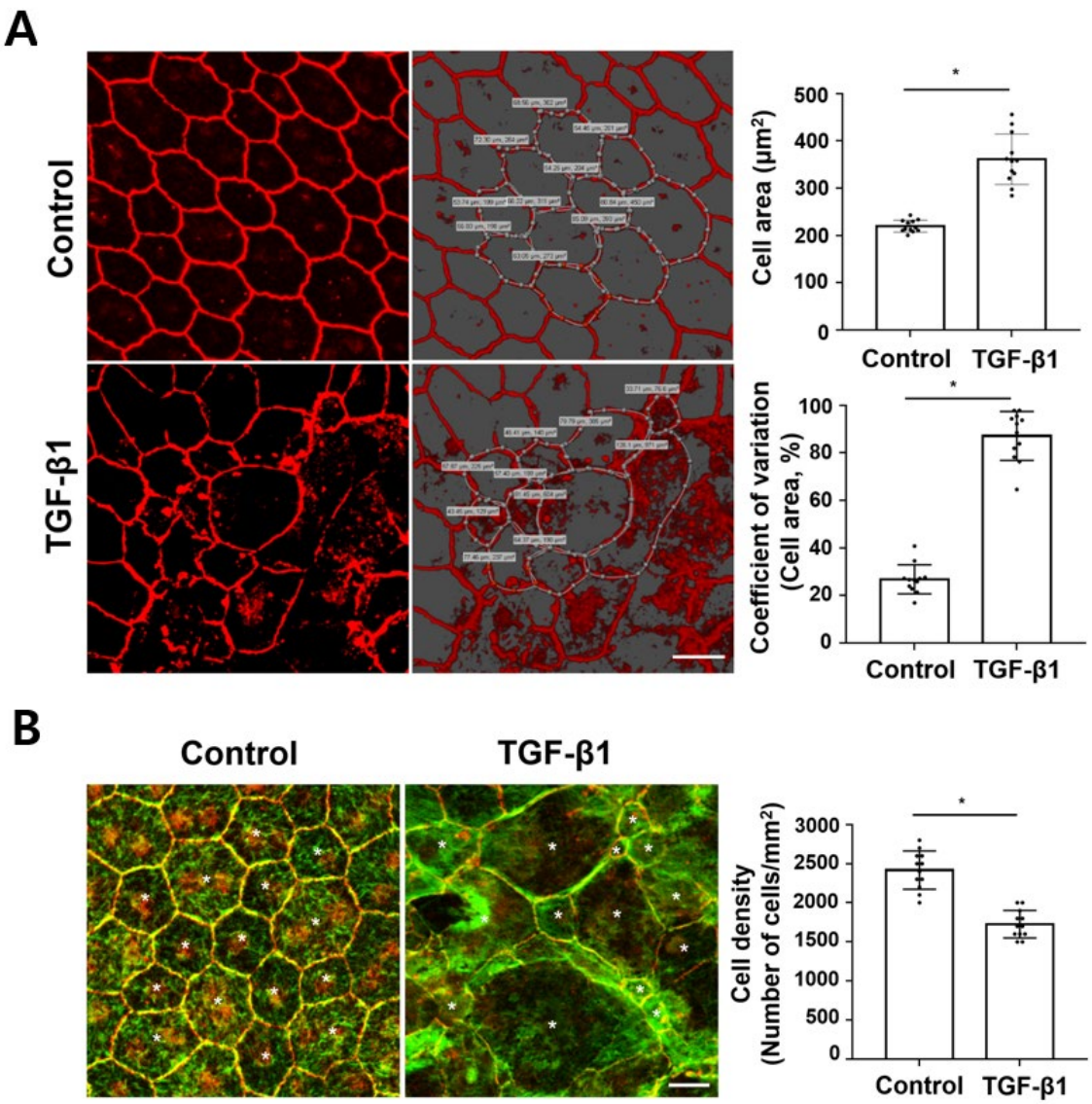

Figure 2.6. Intravitreal injection of TGF-β1 induces morphometric changes of the RPE.

(A) Representative immunofluorescence images of retinal pigment epithelium (RPE) sheets stained with zonula occludens-1 (ZO-1, red) to evaluate morphometric measurements of RPE. Each value indicates the mean ± standard error of the mean (SEM) (n = 6 mice for each data set). *$P < 0.01$ by Student's t test. Scale bar = 20 μm.

(B) Representative immunofluorescence images of RPE sheets co-stained with anti-ZO-1 (red) and anti-F-actin (green) to evaluate cell density. We counted the RPE cells, which could only distinguish all cell boundaries in the randomly selected sampling box (100 × 100 μm). Asterisks indicate RPE cells that met the aforementioned condition. Each value indicates the mean ± SEM (n = 6 mice for each data set). *$P < 0.01$ by Student's t test. Scale bar = 20 μm.

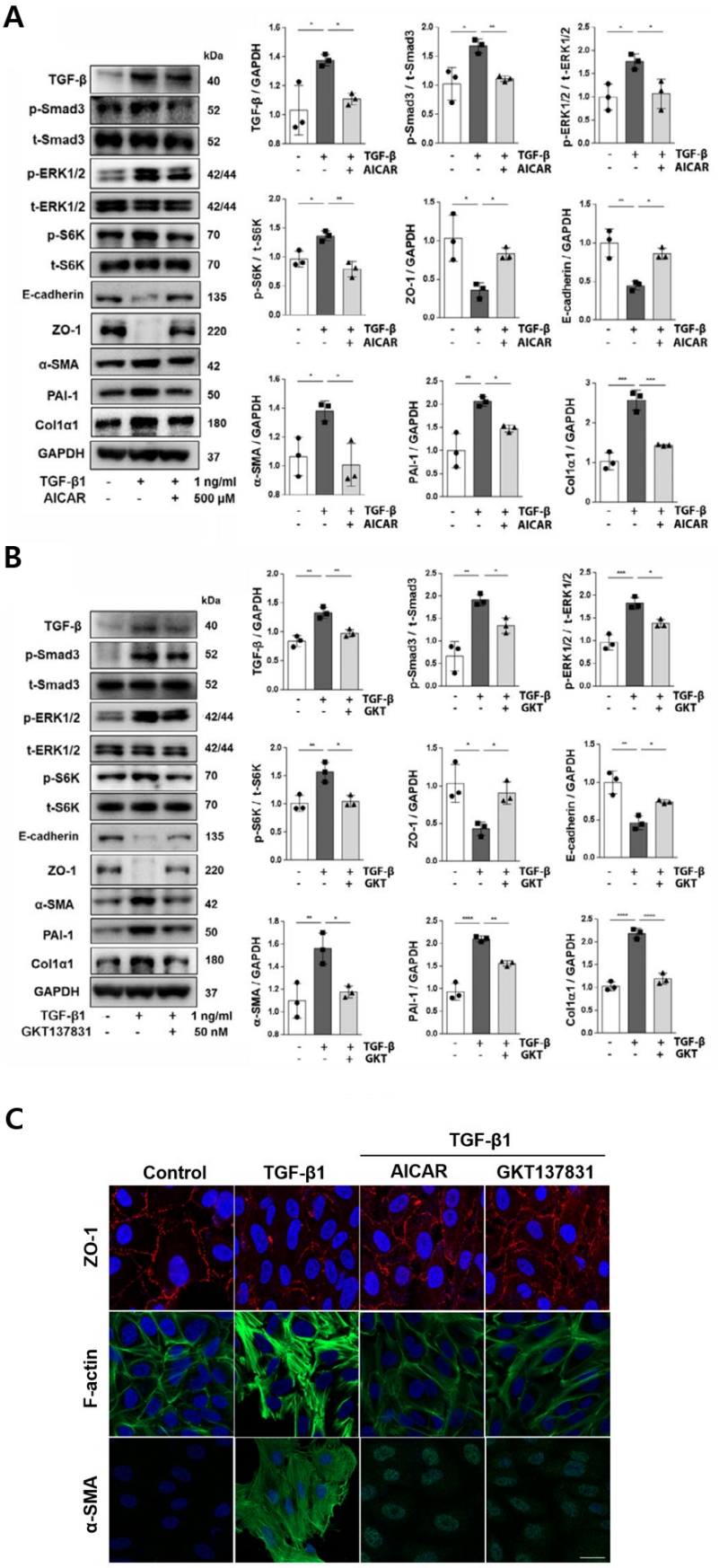

Figure 2.7. The TGF-β1-mTORC1-NOX-ROS pathway regulates EMT in ARPE-19 cells.

(A-B) Representative western blot data showing the expression of transforming growth factor beta-1 (TGF-β1), total (t) and phosphorylated (p) suppressor of mothers against decapentaplegic

3 (Smad3), extracellular signal-regulated kinase 1/2 (ERK 1/2), and ribosomal protein S6 kinase (S6K), E-cadherin, zonula occludens-1 (ZO-1), alpha-smooth muscle actin (α-SMA), plasminogen activator inhibitor-1 (PAI-1), alpha-1 type I collagen (collagen 1α1), and glyceraldehyde 3-phosphate dehydrogenase (GAPDH) in different treatment groups. 5-aminoimidazole-4-carboxamideribonucleotide (AICAR, 500 μM) or GKT137831 (50 nM) were pretreated before TGF-β1 treatment (1 ng/ml for 48 hours). Quantitative analysis using densitometry was performed by measuring protein expression relative to the loading control (GAPDH). Each value represents the mean ± standard error of the mean (SEM). *$P < 0.01$ by by Mann-Whitney U test.

(C) Representative immunofluorescence images stained with anti-zonula occludens-1 (ZO-1), anti-F-actin, anti-alpha-smooth muscle actin (α-SMA) in adult retinal pigment epithelial cell line-19 (ARPE-19) cells after 24 hours of stimulation with transforming growth factor beta-1 (TGF-β1, 1 ng/ml) with or without 5-aminoimidazole-4-carboxamideribonucleotide (AICAR, 500 μM) or GKT137831 (50 nM). Scale bar = 20 μm.

* Figure 2.7 data was prepared by Soo-Jin Kim and Professor Kyu-Sang Park.

To evaluate TGF-β1-induced EMT, ARPE-19 cells were stained with anti-ZO-1, anti-F-actin, or anti-α-SMA antibodies. Immunostaining data revealed that TGF-β1 downregulated ZO-1 expression in the epithelial membrane and upregulated F-actin stress fiber and α-SMA expression in the cytosol, similar to the findings in intravitreal TGF-β1 injected RPE tissue (Fig. 2.7C). Furthermore, to investigate whether TGF-β1 treatment generated oxidative stress, we treated APRE-19 cells with a fluorescent dye, 2',7'-dichlorodihydrofluorescein diacetate (DCF-DA), and measured fluorescence intensity reflecting cytosolic reactive oxygen species (ROS). We found that TGF-β1 treatment significantly stimulated the generation of intracellular ROS (Fig. 2.8).

Next, we pretreated ARPE-19 cells with 5-aminoimidazole-4- carboxamide ribonucleotide (AICAR), an adenosine monophosphate-activated protein kinase (AMPK) activator, which is known to suppress mTOR activation, or nicotinamide adenine dinucleotide phosphate (NADP) oxidase 1/4 (NOX1/4) inhibitor, GKT137831 to evaluate the effect on EMT of RPE by inhibiting TGF-β1 signaling or by inhibiting NOX4, respectively. Pretreatment with AICAR or GKT137831 not only inhibited endogenous TGF-β1 upregulation but also blocked activation of TGF-β1-related mediators, including Smad3, ERK1/2, and p70S6K. Moreover, AICAR or GKT137831 abrogated all the pathogenic alterations triggered by TGF-β1, including loss of epithelial markers, upregulation of mesenchymal markers (Fig. 2.7A-C), and ROS generation (Fig. 2.8). These results provide evidence that the ERK1/2-mTORC1-NOX-ROS pathway is critically involved in TGF-β1- induced EMT and structural changes in RPE cells.

Blockade of the mTORC1-NOX pathway ameliorates EMT and protects morphometric changes of the RPE induced by intravitreal TGF-β1 injection.

To investigate the protective effect of AICAR or GKT137831 against EMT of the RPE tissue *in vivo*, we intravitreally injected AICAR (500 μM/eye) or GKT137831 (50 μM/eye) alongside TGF-β1 (200 ng/eye). We observed that cotreatment with AICAR or GKT137831 remarkably reduced the stress fiber stained with F-actin and α-SMA but increased intact ZO-1 expression (Fig. 2.9A). We further conducted western blot analyses of the RCS complex, showing that AICAR or GKT137831 treatment prevented TGF-β1-induced EMT, inhibiting downregulation of ZO-1 and E-cadherin, and upregulation of α-SMA (Fig. 2.9B).

A

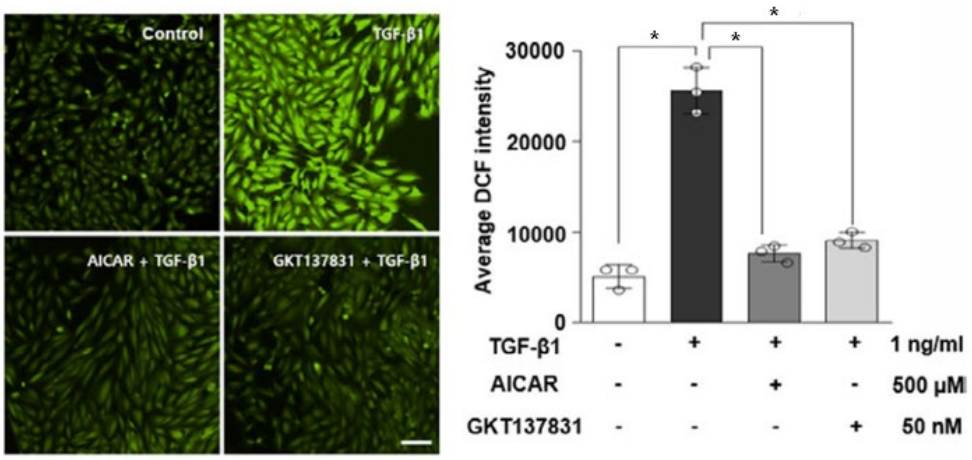

Figure 2.8. The TGF-β1-mTORC1-NOX-ROS pathway regulates ROS production.

(A) Representative fluorescence images of intracellular reactive oxygen species (ROS) in ARPE-19 cells and quantitative analysis of intracellular ROS using 2', 7'-dichlorofluorescein (DCF) dye. Scale bar = 100 μm. Each value represents the mean ± standard error mean (SEM). *P <0.01, obtained using one-way ANOVA and Tukey's post-hoc tests.

* Figure 2.8 data was prepared by Soo-Jin Kim and Professor Kyu-Sang Park.

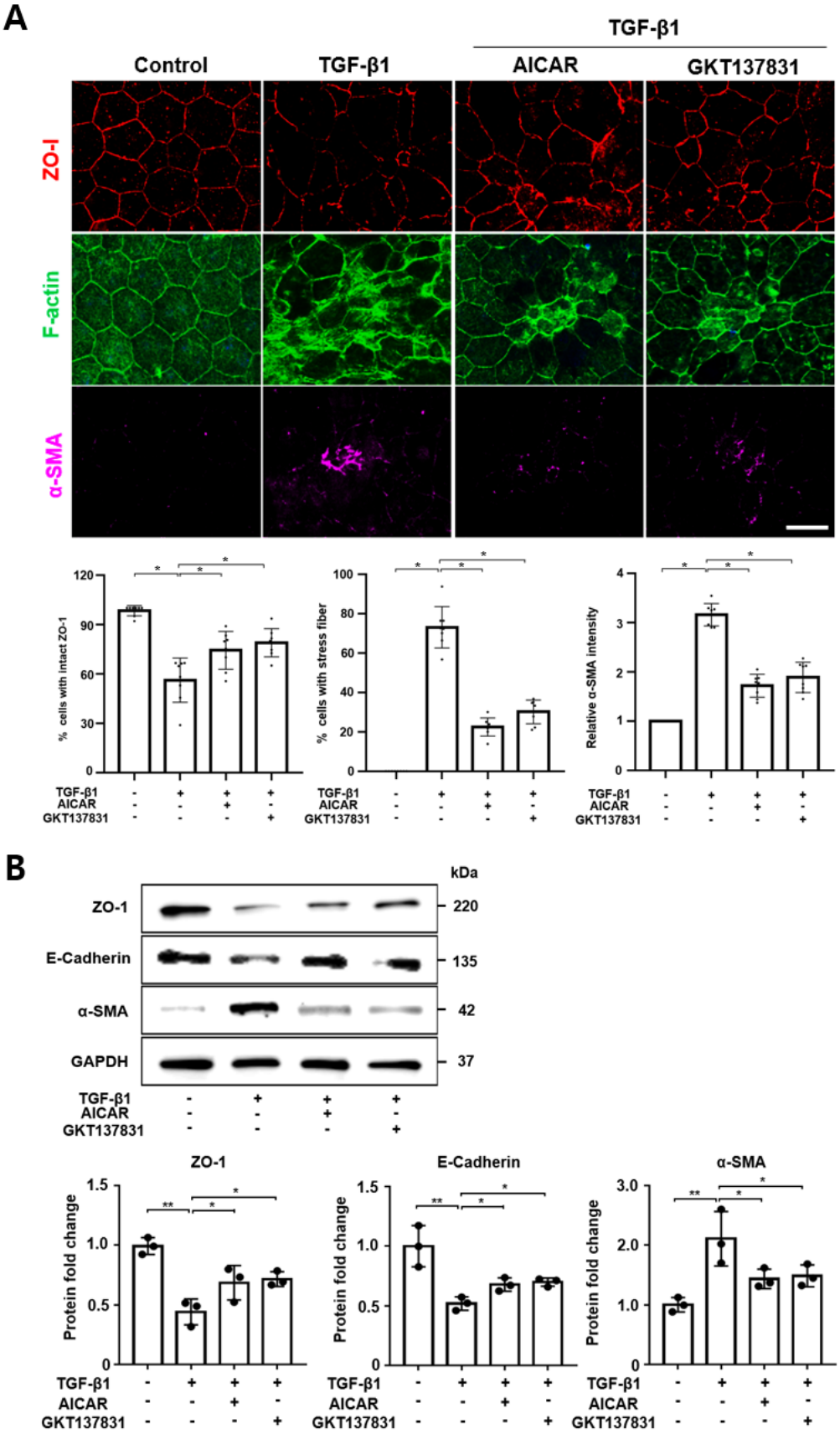

Figure 2.9. Blockade of the mTORC1-NOX pathway ameliorates EMT of the RPE induced by intravitreal TGF-β1 injection.

(A) Representative confocal immunofluorescence images by groups stained with epithelial-

mesenchymal transition (EMT) markers: zonula occludens-1 (ZO-1, red), F-actin (green), alpha-smooth muscle actin (α-SMA, pink). Scale bar = 50 μm. Treatment groups were dosed with 5-aminoimidazole-4-carboxamideribonucleotide (AICAR, 500 μM) or GKT137831 (50 μM/eye) along with transforming growth factor beta-1 (TGF-β1, 200 ng/eye). Quantitative analysis of EMT markers in RPE tissues shows the percentage of cells with intact ZO-1, stress fiber, and relative fluorescence intensity of α-SMA in the RPE tissue. All quantitative data were analyzed with NIH ImageJ software. Each value indicates the mean ± standard error of the mean (SEM) (n = 8 mice for each data set). *P < 0.01 by one-way ANOVA and Tukey's post hoc tests.

(B) Western blot analysis of retinal pigment epithelium-choroid-scleral complex treated with intravitreal phosphate buffer saline or treatment materials (TGF-β1 alone, TGF-β1 with AICAR, TGF-β1 with GKT137831). Expression of EMT markers (ZO-1, E-cadherin, and α-SMA) and a loading control (glyceraldehyde 3-phosphate dehydrogenase, GAPDH) was analyzed. Intensity values of densitometry were normalized relative to control values. Each value indicates the mean ± SEM. *P < 0.01, **P < 0.001 by one-way ANOVA and Tukey's post hoc tests.

To confirm the protective effect of AICAR or GKT137831 on morphometric changes of the RPE, we analyzed immunofluorescence staining images stained with ZO-1 and F-actin by confocal microscopy. AICAR or GKT137831 cotreatment rescue the cell area and its coefficient of variation induced by TGF-β1 treatment (Fig. 2.10A). Furthermore, AICAR or GKT137831 cotreatment showed protective effect against the reduction of cell density induced by TGF-β1 treatment (Fig. 2.10B). Taken together, these results suggest that AICAR or GKT137831 treatment attenuated EMT and morphometric changes of RPE induced by intravitreal TGF-β1 injection.

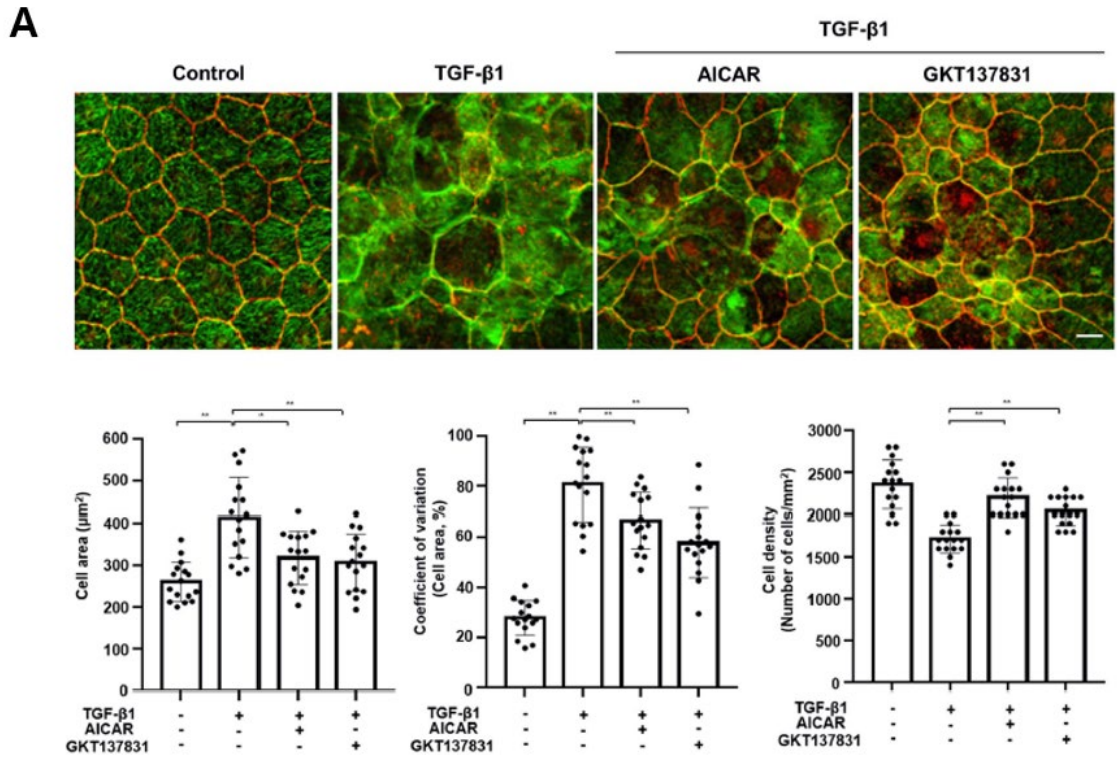

Figure 2.10. Blockade of the mTORC1-NOX pathway protects morphometric changes of the RPE induced by intravitreal TGF-β1 injection.

(A) Representative images of retinal pigment epithelium (RPE) sheets stained with zonula occludens-1 (ZO-1, red), F-actin (green) to evaluate morphometric changes.

Randomly selected sampling box (100 × 100 μm) images were collected and analyzed of cell area, coefficient of variation, and cell density. Each value indicates the mean ± SEM. *P < 0.01, **P < 0.001 by one-way ANOVA and Tukey's post hoc tests.

DISCUSSION

In this study, we confirmed that intravitreal TGF-β1 injection triggers morphometric changes and EMT in the RPE during normal aging and AMD. We found the ERK1/2-mTORC1- NOX-ROS pathway is crucially involved in the TGF-β1-induced EMT of the RPE. Blockade of this pathway attenuates EMT and improves the regularity of the RPE structure *in vitro* and *in vivo*.

RPE is essential for maintaining homeostasis of the visual sensory system by supporting the neuronal retina and choroid, regulating metabolic transport, participating in the visual cycle, secreting cytokines, chemokines, and growth factors, and forming the outer blood-retinal barrier (177, 254). During the aging process, one of the phenotypic changes is the acceleration of EMT in the RPE. EMT is characterized by the loss of intercellular junctions, switching to a mesenchymal phenotype with cytoskeleton rearrangement (255). We demonstrated that intravitreal TGF-β1 injection mimicked age-related morphometric changes in RPE tissues, including structural alterations and EMT (Fig. 2.5 and 2.6). These findings suggest the possibility of establishing a screening model that reflects the phenotype observed in aging and age-related retinal diseases, which may be useful for the development of therapeutic strategies against AMD, DR, and proliferative vitreoretinopathy.

As RPE ages, the decline in antioxidant activity and the ability to decrease intracellular ROS can induce endogenous TGF-β expression (255, 256). Interestingly, the downstream effect of TGF-β1 is NOX4-mediated ROS production, comprising a feed-forward activation loop via oxidative stress-mediated TGF-β1 upregulation, leading to the amplification of TGF-β1-mTORC1-NOX4-ROS signaling, which promotes the EMT of the RPE (257). The pathological consequences are evident in previous reports showing that abnormal activation of the mTORC1 pathway or ROS production correlates with EMT in aged RPE cells (255, 258, 259). In this regard, we employed a strategy involving the activation of AMPK using AICAR and blockade of NOX activity and ROS generation using GKT137831 to examine the pathogenic roles of mTORC1 and NOX signaling in the development of structural changes and EMT in RPE.

AMPK not only interferes with upstream mTOR signaling in TGF-β signaling, including Smad3 and ERK1/2 phosphorylation (260, 261), but also decreases TGF-β

transcription, leading to a reduction in its serum concentration (262). Meanwhile, the upregulation of NOX4 is an essential mechanism underlying TGF-β1- induced oxidative stress, leading to the EMT of the RPE (257). In this study, we demonstrated that AICAR and GKT137831 protected against structural alterations in RPE tissue induced by intravitreal TGF-β1 injection *in vivo* and by incubating ARPE-19 cells with TGF-β1 in vitro. It is noteworthy that both AMPK activation and NOX inhibition prevented upstream and downstream signaling of TGF-β1 and endogenous TGF-β1 expression. These results imply that blocking any step in this amplifying loop could be similarly effective for attenuating EMT and morphometric changes in the RPE. These findings may play an important role in the development of an effective therapeutic strategy aimed at inhibiting TGF-β signaling.

In this study, we focused on reflecting the partial phenotypes observed in aged RPE and AMD, such as morphometric changes and EMT of the RPE. However, there are certain limitations to our study. First, the concentration of TGF-β1 is much higher than pathogenic concentrations in the eyes of patients with AMD (244, 245). Second, our TGF-β1-induced experimental model was applied for a short period (three days) and a single injection. Therefore, this acutely induced RPE injury model dose not fully reflect the various pathophysiological features of AMD, considering that AMD is a multifactorial disease that develops over years or decades. Therefore, we require attention that this model is not a disease model but more suitable as a screening model for AMD therapeutics.

In conclusion, intravitreal TGF-β1 injection effectively induced morphometric changes and EMT in the RPE *in vivo*, mimicking the status of the epithelium in aged RPE and AMD. Furthermore, AICAR and GKT137831 ameliorated morphometric changes and EMT in RPE induced by TGF-β1 treatment. Thus, we suggest that intravitreal TGF-β1 injection can be a useful experimental tool for studying morphometric changes and the EMT of the RPE. From the perspective that structural changes and cell functions are closely connected, regulation of the mTORC1-NOX-dependent ROS pathway may be a potential therapeutic target to guard against functional alterations observed in aged RPE and AMD.

CHAPTER 3-1

Regulation of Corneal Neovascularization in Dry Eye Disease via Subconjunctival NK1R Antagonist Injection

INTRODUCTION

Dry eye disease (DED) is a multifactorial disorder of ocular surface that causes visual disturbances and ocular discomfort (67). Among various factors, inflammation and immune responses play an important role in the pathogenesis of DED. Notably, a unique form of selective corneal lymphangiogenesis without associated hemangiogenesis has been reported in DED in the experimental and clinical settings (69, 70). This growth of lymphatic vessels into the cornea acts as an afferent arm, which facilitates the migration of mature antigen-presenting cells (APCs) to the regional lymph nodes (RLNs), followed by the activation of effector T helper type 1 (Th1) cells and Th17 cells (71, 263, 264).

Substance P (SP) is an 11-amino acid neuropeptide produced by neuronal and inflammatory cells. SP exerts its inflammatory and immunological activities via the high-affinity neurokinin-1 receptor (NK1R) (76, 77). The cornea is densely innervated by sensory nerves originating from the trigeminal ganglion, which produce various neuropeptides, including SP, neuropeptide Y, calcitonin gene-related peptide, and vasoactive intestinal peptide (72, 265). Although the pathogenic mechanisms remain unclear, SP promotes corneal hemangiogenesis following inflammation not only in alkali burn or suture models but also in a co-culture system of trigeminal ganglion isolated from mice with DED and vascular endothelial cells *in vitro* (78, 266). Furthermore, SP involves the maturation of APCs in the cornea, as well as activation of Th17 cells in the conjunctiva and RLNs (267).

Corneal lymphangiogenesis is an essential finding in the pathogenesis of DED related to ocular surface immunity disruption (69, 71, 268). Although vascular endothelial growth factor C and D (VEGF-C and VEGF-D)/VEGF receptor 3 (VEGFR3) is generally regarded as the principal inducer of corneal lymphangiogenesis, it has been reported that the SP/NK1R system can also induce corneal lymphangiogenesis in diverse corneal inflammatory conditions (78, 79). However, to the best of our knowledge, no study has evaluated the efficacy of blocking the SP/NK1R system to regulate corneal lymphangiogenesis in DED.

In this study, we evaluated the role of the SP/NK1R system in the regulation of pathologic corneal lymphangiogenesis and investigated the mechanism by which SP promotes lymphangiogenesis using human dermal lymphatic endothelial cells (HDLECs) and a controlled

environment chamber (CEC)-induced dry eye mouse model.

MATERIALS AND METHODS

1. Cell culture

Human dermal lymphatic microvascular endothelial cells (HDLECs) were obtained from Lonza (#CC-2810, HMVEC-dLyAd) and maintained in endothelial basal medium-2 (EBM-2, #CC-3156, Lonza) supplemented with EGM-2 MV BulletKit (#CC-3125, Lonza), and 7–10 passages were used for experiments.

2. Immunocytochemistry

HDLECs grown on eight chamber culture slides (1×10^4 cells/well, # 30108, SPL) were rinsed twice with phosphate-buffered saline (PBS) and fixed with 4% paraformaldehyde for 15 minutes at room temperature (RT). Next, cells were permeabilized with 0.25 % Triton X-100 for 5 min and blocked with 1 % BSA in PBS for 30 min. Incubation with antibodies for NK1R (1:100), lymphatic vessel endothelial hyaluronan receptor-1 (LYVE-1) (1:100) was performed overnight at 4 ◦C followed by incubation with secondary antibody for 1 hour at room temperature in a dark room. Fluorescence images were obtained using a confocal microscope (Leica TCS STED, Leica Microsystem Ltd.).

3. Western blotting

Western blot analysis was performed using following antibodies: anti-VEGFR3 (1:1000), anti-GAPDH (1:1000), anti-rabbit IgG-HRP conjugate (1:5000), anti-mouse IgG-HRP conjugate (1:5000). The protein intensity was quantified using ImageJ 1.53c software (National Institutes of Health, Bethesda, MD, USA).

4. Proliferation assay

HDLECs (5×10^3 cells) were seeded into each well of 96-well plates with 100 μL of EBM-2 containing 2 % (v/v) FBS. After incubation for 24 h, cells were treated with or without 1 μM SP (#05-23-0600, Calbiochem) alone, 1 μM SP with 10 μM NK1R antagonist (L733,060, #1145, Tocris Bioscience), 10 μM NK1R antagonist alone for 48 hours. Then, the medium was exchanged and added 10 μL of WST-1 solution (#EZ-1000, Daeil Lab Service Co. Ltd). After

incubation for 2 hours, absorption at 450 nm was measured using a microplate spectrophotometer (Molecular Devices, Sunnywale, CA, USA).

5. Tube formation assay

HDLECs (1×10^5 cells) were plated on 35 mm dishes and cultured in media with or without treatment material for 5 hours. Tube formation image was captured and quantitatively analyzed by calculating number of tube junctional node in randomly selected fields.

6. Cell migration assay

HDLECs (5×10^5 cells) were plated on 35 mm dishes and incubated with media and wounded with a pipette tip. After incubation with or without treatment material for 24 hours, the degree of migration was quantified by analyzing percentage of wound closure using NIH ImageJ software.

7. NK1R inhibition with siRNA transfection and gel electrophoresis of PCR products

siRNA targeting NK1R was chemically synthesized and purified in the 2'-deprotected and desalted form (Bioneer). Negative control siRNA (Bioneer) was used as a control for comparison. The sequences of human NK1R siRNA pair were 5'-CGUAGUGGGAAUCACACUATT-3' and 5'-UAGUGUGAUUCCCACUACGTT-3' and the sequences of control siRNA pair were 5'-CUAUCAAGUGUCUCGUUGUTT-3', 5'-ACAACGAGACACUUGAUAGTT'3'. Human dermal lymphatic endothelial cells (HDLECs) were 50-70% confluent on the day of transfection. Lipofectamine 3000-siRNA was prepared with the commercial Lipofectamine 3000 Transfection Reagent (Invitrogen) according to the instruction. After 48 h incubation time, the cells were lysed in RNA isolation reagent (trizol reagent, #15596026, Invitrogen). Equal amounts of RNA from each sample were used to synthesize double-stranded cDNA by reverse transcription (High Capacity RNA-to-cDNA Kit, #4388950, Applied Biosystem). The PCR was done using NK1R, VEGFR3, and β-actin primers. Primers sequences: NK1R (185 bp), 5'-CATTGTGGTGACCTCTGTGG-3' (sense) and 5'-ACAGGCCGTAGTACCATTCG-3'(anti-sense), VEGFR3 (529 bp), 5'-TGCGAATACCTGTC CTACGATGC-3' (sense) and 5'-CTTGTGGATGCCGAAAGCGGAG-3'(anti-sense), and β-

actin (513 bp), 5'-GTGCTATCCCTGTACGCCTC-3' (sense) and 5'-AATGCCAGGG TACATGGTGG-3' (anti-sense). RT-PCR was performed under these reactions: initial denaturation in one cycle at 95°C for 15 minutes followed by 45 cycles of thermal degeneration at 95°C for 30 seconds, annealing at 60°C for 1 minute, and elongation reaction at 72°C for 1 minute. Then, gel electrophoresis of PCR products (2% agarose in 1 X TAE, electrophoresis running condition: 100 V, 30 minutes) was done and exposed in ImageQuant LAS 4000 (GE Healthcare Life Sciences).

8. Mice

Eight to ten-week-old C57BL/6J female mice maintained in a specific pathogen-free facility in the Seoul National University, which were purchased from Central Laboratory (Seoul, Korea). All animal experiments in this study were approved by the Seoul National University Animal Care and Use Committee and conducted in strict agreement with the guidelines of the Association for Research in Vision and Ophthalmology Statement. The mice were fully anesthetized by inhalation of 4% of isoflurane (Ifran®; Hana Pharm, Seoul, Korea) with oxygen in the chamber (0.5–1L/minute, flow rate).

9. Experimental dry eye mouse model

Dry eye was induced by housing the mice in the controlled environmental chamber (CEC), allowed for a relatively low humidity (<25 %), continuous regulation of airflow, and constant temperature of 21°C–23°C for 14 or 21 days. To avoid possible compounding effects in terms of immunopathogenesis of DED, subcutaneous scopolamine, which attenuates Th17 activity and enhances Th2 and Treg responses (269), was not administered as previously reported (266, 267). The room air control group mice were housed in room air conditions.

10. Corneal disepithelization model

Experimental corneal disepithelization model was generated in the right eyes of ten-week-old C57BL/6J female mice. The mice were fully anesthetized by intraperitoneal injection using the mixture (3:1 ratio, 1 mL/Kg) of zolazepam and tiletamine (Zoletil 50, Virbac) and xylazine

(Rompun, Bayer Korea). The whole corneal epithelium was scraped with a blunt spatula with care taken to avoid limbal blood vessels. After the debridement, the eyes were rinsed with saline, and applied a topical 0.5% levofloxacin (Cravit®, Santen). The topical 0.5% levofloxacin was applied one time per day for the 7 days to minimize infection.

11. Corneal fluorescein staining (CSF) and phenol red thread test

To examine CFS, 0.7 μL of 2.5% fluorescein was gently applied into the lateral conjunctival sac of the mice, and after 3 minutes, corneas were observed with a slit-lamp microscope (Leica Microsystems, Ltd.) under cobalt blue light. Punctuate epithelial staining was recorded in a masked manner according to the standard National Eye Institute grading system (Bethesda, MD) of 0–3 to each of five areas of the cornea, and scores of five areas were added to calculate a final grade (total, 15 points). The amount of tears was measured with the phenol red thread tear test using cotton threads (PRT-TEST, Tianjin Jingming New Technological Development Co., Ltd.) on days 0, 3, 7, 13 at the same time point of the day (1 p.m.). Briefly, the lower eyelid of mice was pulled down gently, and a 1 mm portion of the thread was inserted in the lateral conjunctival sac. Each eye in two groups (control and experimental group) was tested with the eyes open for 15 seconds. The portion of thread stained with red was measured in millimeters.

12. Subconjunctival injection of NK1R antagonist in experimental dry eye mouse model

A total of 6.6 μg/5 μL of L733,060 (NK1R antagonist) for the DED treatment group or 5 μL of phosphate-buffered saline (PBS) for DED control group was administered through subconjunctival injection with microliter syringe with 34 gauge beveled needle (Hamilton Bonaduz AG, Bonaduz, Switzerland) under inhalation anesthesia at every 48–72 hours from day 0 to day 14 of DED induction by CEC. (Subconjunctival injection time: day 0, 2, 4, 7, 9, 11, 14).

13. Subconjunctival injection of siNK1R and NK1R antagonist in corneal disepithelization model

Negative control siRNA (20 μM/5 μL), siNK1R (20 μM/5 μL), or NK1R antagonist (6.6 μg/5 μL, L733,060) were administered through subconjunctival injection with microliter syringe with

34 gauge beveled needle (Hamilton Bonaduz AG, Bonaduz, Switzerland) under anesthesia at day 0, 2, 5 after corneal disepithelization injury. The sequences of siNK1R pair were 5'-CUCUGACUGAAUAUGUCUATT-3', 5'-UAGACAUAUUCAGUCAGAGTT-3'. The sequences of control siRNA pair were 5'-CUAUCAAGUGUCUCGUUGUTT -3', 5'-ACAAC GAGACACUUGAUAGTT'3'.

14. Immunohistochemistry and morphometry

Prepared whole-mounted corneas were rinsed in PBS and fixed by ice-chilled mixture of acetone and methanol (1:1) for 10 minutes at room temperature. After washing with the PBS, whole-mounted corneas were incubated in Perm/ Block solution (0.2% Triton-X 100 and 0.3% bovine serum albumin in PBS) at room temperature for 30 minutes. Immunohistochemistry was performed using following antibodies: anti-CD31 (1:200) and anti-LYVE-1 (1:200), Alexa Fluor 488 goat anti-rabbit IgG (1:400), Alex Fluor 594 goat anti-rat IgG (1:400).

15. RNA extraction and quantitative real time PCR

The cornea and conjunctiva were lysed in RNA isolation reagent (trizol reagent, #15596026, Invitrogen) and homogenized using a probe sonicator (Branson 450 Digital Sonifier, Emerson., Danbury, CT, USA). Equal amounts of RNA from each sample were used to synthesize double stranded cDNA by reverse transcription (High Capacity RNA-to-cDNA Kit, #4388950, Applied Biosystems). The cDNA was analyzed by realtime PCR (Step one plus, Applied Biosystems, USA) for the following cytokines: Tac1 (Taqman Gene Expression Assays ID, Mm01166996_m1), VEGF-C (Mm00437310_m1), VEGF-D (Mm00438965_m1), and VEGFR3 (Mm00433337_m1). GAPDH (Mm99999915_g1) was used for normalization of gene expression.

15. Statistical analysis

Statistical analyses were performed using SPSS software version 22.0 (SPSS Inc., Chicago, IL, USA). Experimental data were presented as mean ± standard error of the mean (SEM). *P* values were determined by the multiple groups.

RESULTS

Lymphangiogenesis is induced in the originally avascular cornea by the conditions which can cause dry eye in the mice.

We utilized a controlled environmental chamber (CEC) that can induce desiccated conditions via compressed air with an adjustable temperature-dehumidifier to confirm corneal lymphangiogenesis in dry eye disease (DED) mouse model. Next, the corneas were mounted and stained with anti-cluster of differentiation 31 (CD31) and anti-lymphatic vessel endothelial hyaluronan receptor 1 (LYVE1) antibodies at day 0 (control), 7, 14, and 21 after induction of dry eye (Fig. 3.1A). The area of corneal lymphatics significantly increased at day 21 after dry eye induction compared to the control cornea (Fig. 3.1B). These results suggest that CEC-induced desiccating stress-induced lymphangiogenesis in the cornea.

SP/NK1R system promotes lymphangiogenesis of lymphatic endothelial cells *in vitro*.

To evaluate whether substance P/neurokinin-1 receptor (SP/NK1R) system regulates corneal lymphangiogenesis, we first incubated human dermal lymphatic endothelial cells (HDLECs) and conducted immunocytochemistry and real-time polymerase chain reaction (RT-PCR) to determine the expression of NK1R in the HDLECs. We confirmed NK1R expression in HDLECs (Fig. 3.2). Thereafter, we performed angiogenic assays (proliferation assay, tube formation, and migration assay) of HDLECs to examine the lymphangiogenic effect of SP (1 μM) and NK1R antagonist (10 μM, L733,060). SP treatment promoted the HDLECs proliferation compared to that in control, which was significantly ameliorated by co-treatment of NK1R antagonist (Fig. 3.3). Furthermore, tube formation of HDLECs was markedly increased in the average number of branching points with SP treatment, which was significantly inhibited by NK1R antagonist (Fig. 3.4). In migration assay, VEGF-C (10 ng/ml) significantly induced migration of HDLECs, whereas SP and additional NK1R antagonist had minimal effect on HDLECs migration compared to control (Fig. 3.5).

To uncover the mechanism through which exogenous SP treatment induces lymphangiogenic alteration *in vitro*, we incubated HDLECs with SP and/or NK1R antagonist

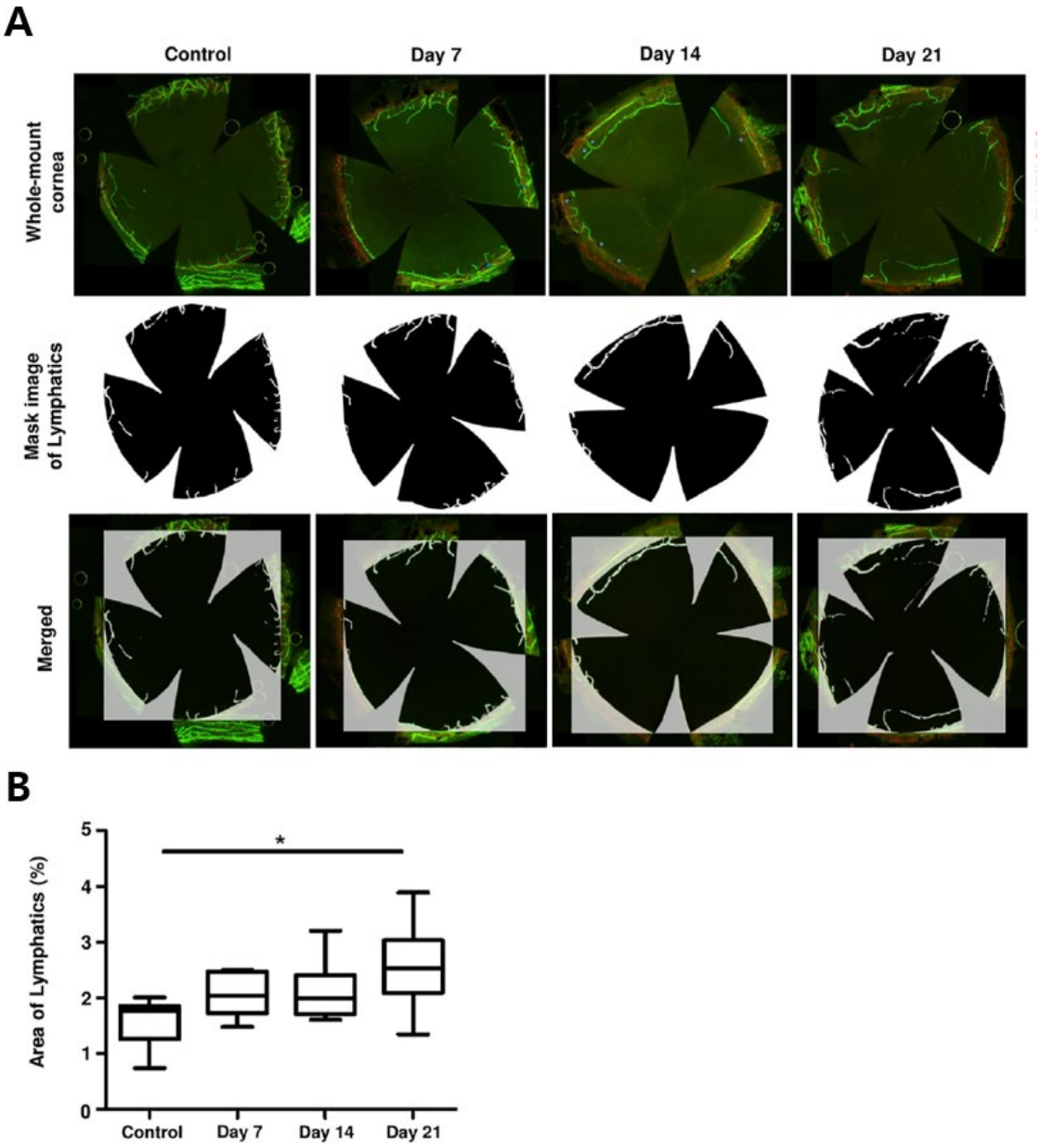

Figure 3.1. Corneal lymphangiogenesis is induced by housing mice in desiccating conditions by CEC.

(A) Representative immunofluorescence images of whole-mounted cornea stained with anti-cluster of differentiation 31 (CD31, red) and anti-lymphatic vessel endothelial hyaluronan receptor 1 (LYVE1, green) antibodies of control group and dry eye group on day 7, 14, and 21 following dry eye induction by controlled environmental chamber (CEC, upper set), their mask images of lymphatics automatically generated by the custom-designed macro of ImageJ (middle set), and merged shole-mounted and mask images (lower set).

(B) Box plot of the area of lymphatic vessels in corneal boundary by period. Each value indicates the mean ± standard error of the mean (SEM) (n = 7-8 mice for each data set). *P <

0.05 by one-way ANOVA and Tukey's post hoc tests.

* Figure 3.1 data was prepared by Professor Sang-Mok Lee.

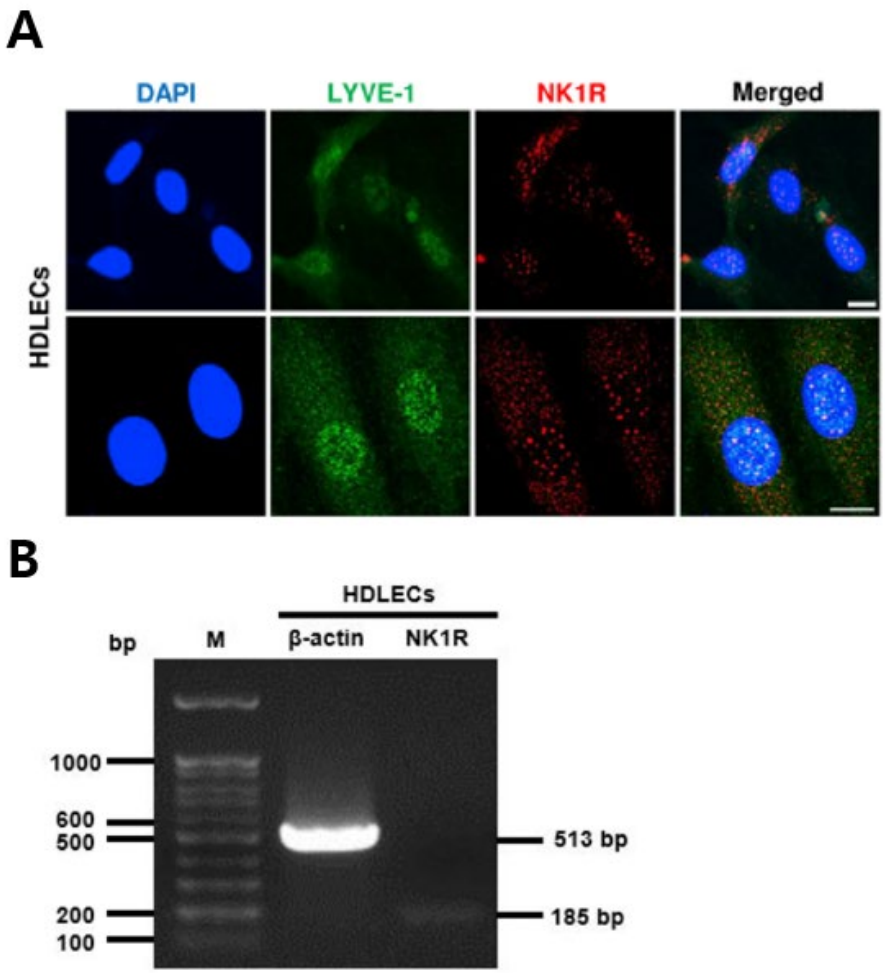

Figure 3.2. The expression of NK1R in the HDLECs.

(A) Representative image of immunocytochemistry of human dermal lymphatic endothelial cells (HDLECs) stained with anti-cluster of differentiation 31 (CD31, red) and anti-lymphatic vessel endothelial hyaluronan receptor 1 (LYVE1, green), 4'6'-diamidino-2-phenylindole (DAPI, blue) showing that neurokinin-1 receptor (NK1R) is expressed in HDLECs. Scale bar, 10 μm.

(B) The mRNA expression level of NK1R and beta-actin (β-actin) in HDLECs identified by gel electrophoresis of polymerase chain reaction products extracted from HDLECs. bp, base pair; M, marker.

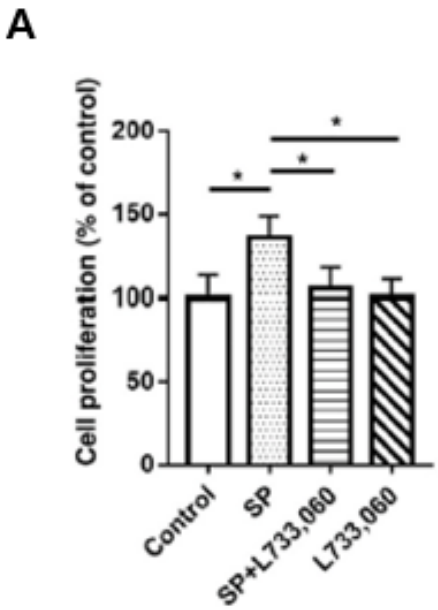

Figure 3.3. Inhibitory effect of NK1R antagonist on SP-induced proliferation of HDLECs.

(A) Human dermal lymphatic endothelial cells (HDLECs) were treated with substance P (SP) alone, SP with neurokinin-1 receptor (NK1R) antagonist (L733,060), NK1R antagonist alone, or medium only for 48 hours. Cell proliferation was evaluated with WST-1 assay. Each value indicates the mean ± standard error of the mean (SEM) (n = 3 for each data set).

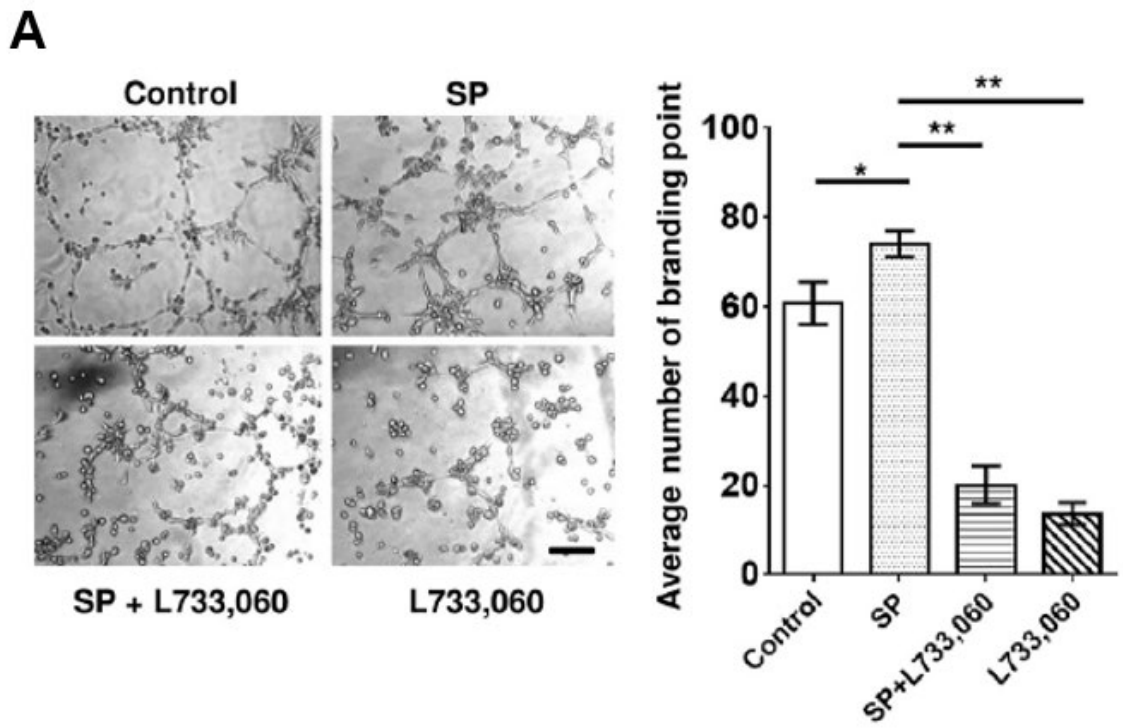

Figure 3.4. Inhibitory effect of NK1R antagonist on SP-induced tube formation of HDLECs. (A) Human dermal lymphatic endothelial cells (HDLECs) were treated with substance P (SP) alone, SP with neurokinin-1 receptor (NK1R) antagonist (L733,060), NK1R antagonist alone, or without treatment material. Tube formation was photographed at 5 hours and quantified as the average number of branching point. Each value indicates the mean ± standard error of the mean (SEM) (n = 5 for each data set). *P < 0.05, **P < 0.01 by one-way ANOVA and Tukey's post hoc tests. Scale bar, 100 μm.

* Figure 3.4 data was prepared by Sang-Taek Im and Professor Sang-Mok Lee.

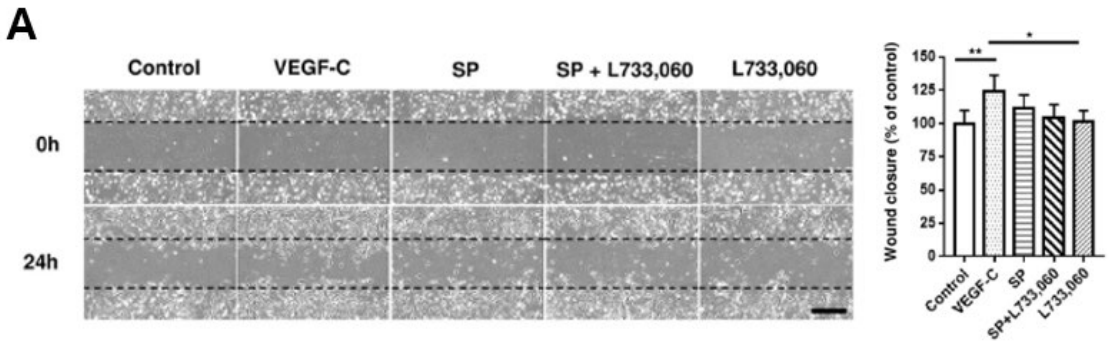

Figure 3.5. Migration assay of HDLECs.

(A) Migration of human dermal lymphatic endothelial cells (HDLECs) when cultured with vascular endothelial growth factor C (VEGF-C), substance P (SP) alone, SP with neurokinin-1 receptor (NK1R) antagonist (L733,060), NK1R antagonist alone, or without treatment material. The migration of HDLECs was photographed at 0 hour and 24 hours and quantified. Each value indicates the mean ± standard error of the mean (SEM) (n = 5 for each data set). *P < 0.05, **P < 0.01 by one-way ANOVA and Tukey's post hoc tests. Scale bar, 100 μm.

and evaluated the vascular endothelial growth factor receptor 3 (VEGFR3) expression, which is the main regulatory receptor of corneal lymphangiogenesis by western blot analysis. SP treatment significantly increased endogenous VEGFR3 expression, which was inhibited by co-treatment of NK1R antagonist (Fig. 3.6). We incubated HDLECs and transfected HDLECs with NK1R-targeted siRNA under incubated with or without SP to exclude the off-target effect of NK1R antagonist on the regulation of VEGFR3 expression. Transfection with NK1R-targeted siRNA dose-dependently reduced NK1R mRNA expression and knockdown of NK1R significantly suppressed SP-induced upregulation of VEGFR3 expression (Fig. 3.7A). Furthermore, knockdown of NK1R as well as NK1R antagonist successfully inhibited SP treatment-induced tube formation. (Fig. 3.7B). Taken together, these findings provide evidence that SP/NK1R system promotes proliferation and tube formation of lymphatic endothelial cells in vitro, possibly through the regulation of the expression of VEGFR3.

NK1R blockade suppresses pathological corneal lymphangiogenesis and improves clinical signs of dry eye *in vivo*.

To further figure out the effect of SP signaling blockade in the corneal lymphangiogenesis *in vivo*, we used established a CEC-induced dry eye mouse model and administrated PBS (5 μL, control group) or NK1R antagonist (6.6 μg/5 μL, L733,060, treatment group) through subconjunctival injection under inhalation anesthesia at every 48-72 hours from day 0 to day 14 after DED induction. Fourteen days following DED induction, we prepared isolated corneal tissues and performed immunofluorescence staining with antibodies specific for vascular endothelial cells (CD31) and lymphatic endothelial cells (LYVE-1). We found that NK1R antagonist treatment significantly reduced the lymphatic areas progressed toward the center of cornea compared to those in PBS treated control group, confirmed by reduction of LYVE-1 expression (Fig. 3.8). Furthermore, we conducted corneal fluorescein staining and phenol red thread test, which reflects corneal epithelium damage and tear volume, respectively. NK1R antagonist treatment partially inhibited the increased punctate corneal epithelial damage and maintained tear volume at 13 days after dry eye induction (Fig. 3.9).

To exclude off-target effect of NK1R antagonist, we performed an inhibition test of

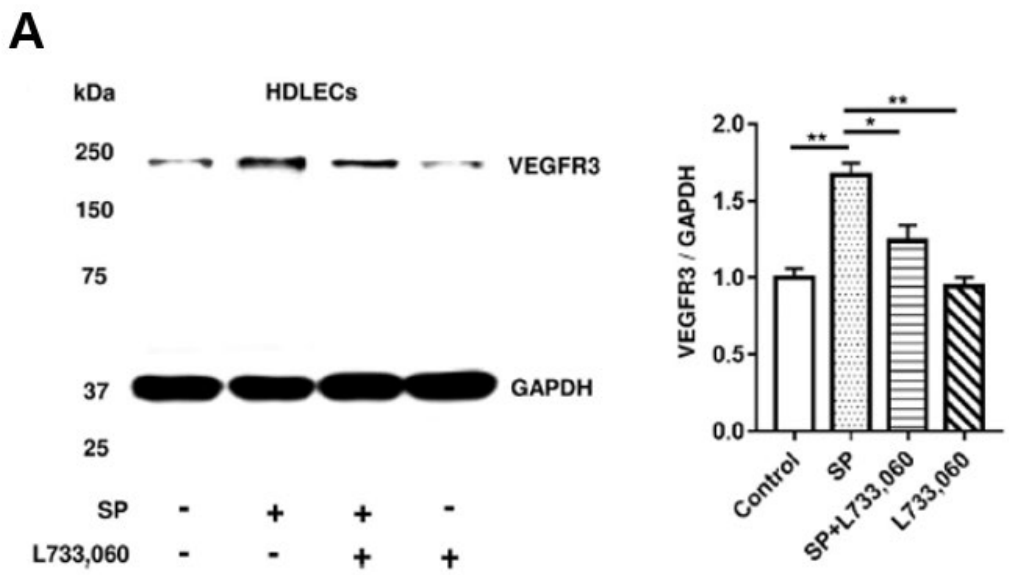

Figure 3.6. SP/NK1R system induces VEGFR3 overexpression in HDLECs related to lymphangiogenesis.

(A) Representative western blot data of human dermal lymphatic endothelial cells (HDLECs), showing expression of vascular endothelial growth factor receptor 3 (VEGFR3) and glyceraldehyde 3-phosphate dehydrogenase (GAPDH) in different treatment groups. Quantitative analysis using densitometry was performed by measuring protein expression relative to the loading control (GAPDH). Each value represents the mean ± standard error of the mean (SEM). *P < 0.05, **P < 0.01 by one-way ANOVA and Tukey's post hoc tests.

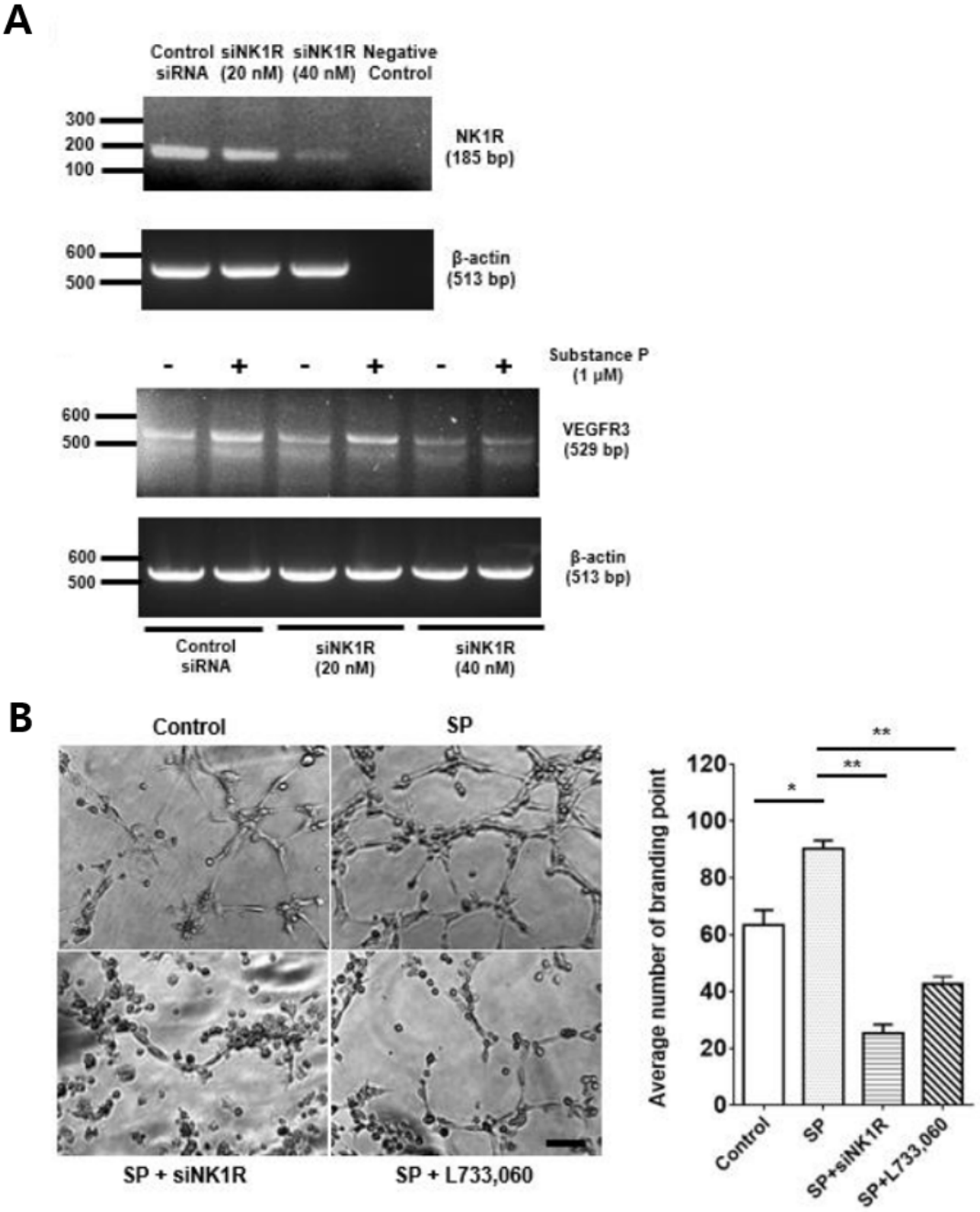

Figure 3.7. The effect of siRNA knockdown of NK1R on lymphatic endothelial cells *in vitro*.

(A) Human dermal lymphatic endothelial cells (HDLECs) were transfected with negative siRNA (control siRNA) or neurokinin-1 receptor (NK1R) targeted siRNA (siNK1R, 20 nM and 40 nM) with or without substance P (1 μM). The mRNA expression level of NK1R, vascular endothelial growth factor receptor 3 (VEGFR3), and beta-actin (β-actin) in HDLECs were identified by gel electrophoresis of polymerase chain reaction (PCR) products extracted from HDLECs.

(B) Representative images of tube formation assay with treatment material (SP [1 μM] alone, SP

with siNK1R [40 nM], SP with L733,060 [10 μM]) or without treatment material. The images were photographed at 5 hour and quantified as the average number of branching point. Quantitative value represents the mean ± standard error of the mean (SEM). *P<0.05, **P<0.01 by one-way ANOVA and Tukey's post hoc test. Scale bar = 100 μm.

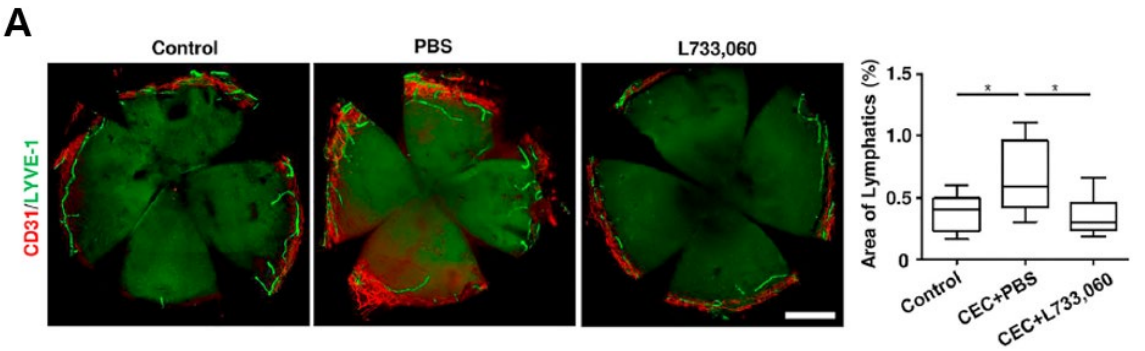

Figure 3.8. The blockade of NK1R ameliorates pathological corneal lymphangiognenesis of dry eye *in vivo*.

(A) Representative immunofluorescence images of the cornea stained with anti-cluster of differentiation 31 (CD31, red) and anti-lymphatic vessel endothelial hyaluronan receptor 1 (LYVE1, green) and quantification of lymphatic area covered with LYVE-1 in the cornea at 14 days after induction of dry eye using CEC. Each value represents the mean ± standard error of the mean (SEM, n=9 mice for each group set). *P < 0.05 by Mann-Whitney U test. Scale bar, 500 μm.

* The quantitative analysis of Figure 3.8 data using ImageJ program was helped by Professor Sang-Mok Lee.

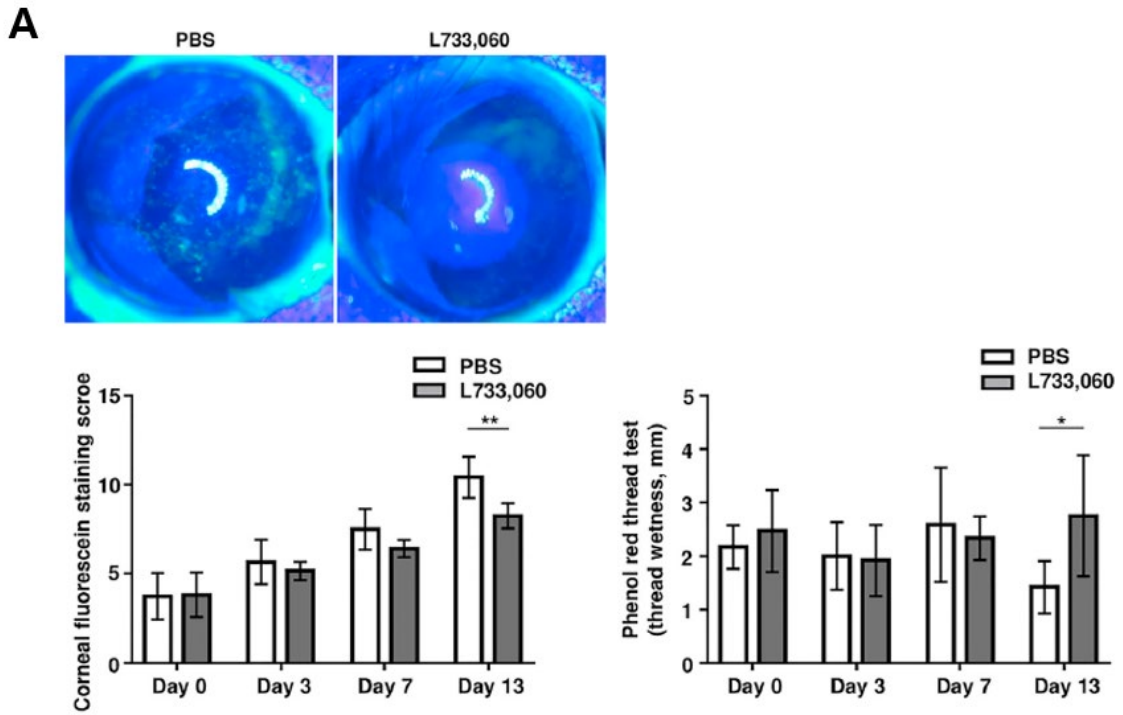

Figure 3.9. The blockade of NK1R improves clinical sings of dry eye *in vivo*.

(A) Representative corneal fluorescein staining images showing punctate epithelial damage at 14 days after induction of dry eye in controlled environment chamber. Quantification of corneal fluorescein staining scoring according to the standard National Eye Institute grading system (Bethesda, MD) and the amount of tears measured by the phenol red thread test. Each value represents the mean ± standard error of the mean (SEM, n=6 mice for each group set). *P < 0.05, **P < 0.01 by Mann-Whitney U test.

NK1R comparing control siRNA, siNK1R, or NK1R antagonist through subconjunctival injection at day 0, 2, 5 of corneal disepithelialization mouse model, a robust *in vivo* model for corneal lymphangiogenesis. We confirmed that siNK1R and NK1R antagonist treatment significantly reduced the area of lymphatic vessels compared to control siRNA treatment (Fig. 3.10). These findings suggest that blockade of SP/NK1R system effectively suppressed pathological corneal lymphangiogenesis and improved clinical signs of dry eye *in vivo*.

The blockade of NK1R in DED downregulates mRNA expression of endogenous SP, VEGF-C, VEGF-D, and VEGFR3 in cornea and conjunctiva

To investigate the mechanism underlying the activation of corneal lymphangiogenesis in DED, we administrated PBS (5 μL, control group) or NK1R antagonist (6.6 μg/5 μL, L733,060, treatment group) through subconjunctival injection every 48-72 hours from day 0 to day 14 following DED induction. NK1R antagonist treatment significantly downregulated SP, VEGF-C, VEGF-D, and VEGFR3 mRNA levels in the cornea and conjunctiva at 14 days after dry eye induction compared to that of control group (Fig. 3.11). These data suggest that blockade of NK1R downregulates endogenous SP, VEGF-C, VEGF-D, and VEGFR3, which can contribute to suppression of the lymphangiogenic effect induced by CEC.

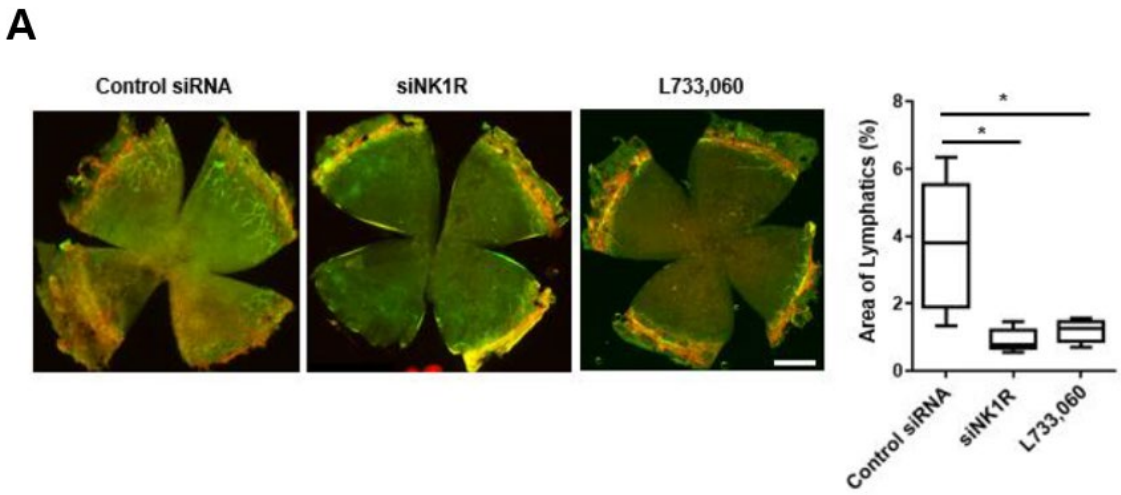

Figure 3.10. The effect of siRNA knockdown of NK1R on lymphatic area in corneal disepithelization model *in vivo*.

(A) Representative immunofluorescence images of the cornea stained with anti-cluster of differentiation 31 (CD31, red) and anti-lymphatic vessel endothelial hyaluronan receptor 1 (LYVE1, green) and quantification of the lymphatics area covered with LYVE-1 in the cornea at 7 days after corneal disepithelization injury. Control siRNA (20 μM/5 μL), siNK1R (20 μM/5 μL), or NK1R antagonist (6.6 μg/5 μL, L733,060) were administered through subconjunctival injection at day 0, 2, 5 after corneal disepithelization injury. Each value represents the mean standard error of the mean (SEM, n=6 mice for each group set). *P<0.05 by Mann-Whitney U test. Scale bar = 500 μm.

* The quantitative analysis of Figure 3.10 data using ImageJ program was helped by Professor Sang-Mok Lee.

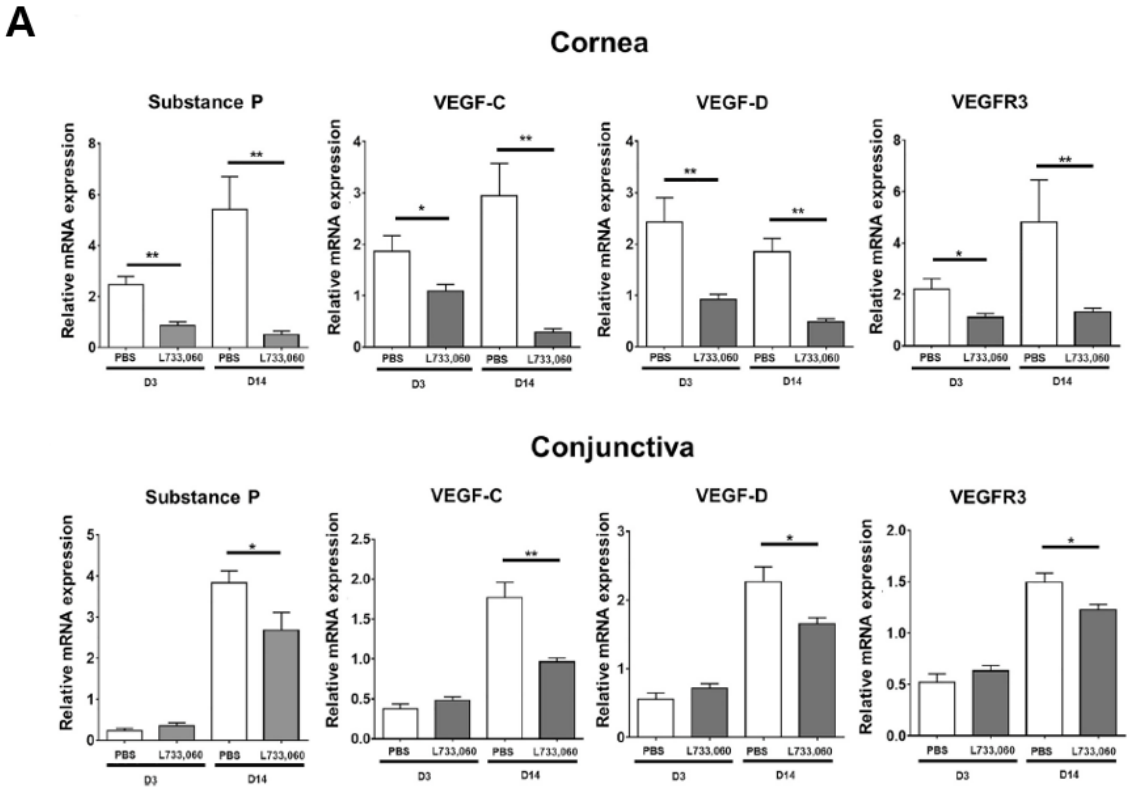

Figure 3.11. Effect of NK1R blockade on the mRNA expression of SP, factors related to lymphangiogenesis in cornea and conjunctiva.

(A) Substance P (SP), vascular endothelial growth factor C (VEGF-C), vascular endothelial growth factor D (VEGF-D), vascular endothelial growth factor receptor 3 (VEGFR3) mRNA expression was analyzed in the cornea and conjunctiva of dry eye disease mouse model. Each group received a subconjunctival injection of phosphate buffered saline (PBS, 5 μL) as vehicle control or neurokinin-1 receptor (NK1R) antagonist (L733,060, 6.6 μg/5 μL) every 48-72 hours and sacrificed at 3 days and 14 days from induction of dry eye in controlled environment chamber. Each value represents the mean standard error of the mean (SEM, n=6 mice for each group set). *P < 0.05, **P < 0.01 by Mann-Whitney U test.

* Figure 3.11 data was prepared by Sang-Taek Im and Professor Sang-Mok Lee.

DISCUSSION

In this study, we investigated the relationship between the SP/NK1R system and corneal lymphangiogenesis in DED. We demonstrated that the SP/NK1R system promotes lymphangiogenesis *in vitro* and that NK1R antagonism suppresses pathologic corneal lymphangiogenesis in DED *in vivo*.

DED is a disease associated with pathologic ocular lymphangiogenesis, including herpetic stromal keratitis, corneal transplantation rejection, chemical burns, glaucoma, and ocular tumor (270-273). Given that corneal lymphatics are important for the migration of mature APCs to RLNs, inhibition of pathological corneal lymphangiogenesis may be a promising strategy to suppress the vicious circle of DED pathogenesis.

SP is an 11-amino acid neuropeptide that originates from the tachykinin precursor 1 gene and is produced by neuronal and inflammatory cells (77). SP binds to NK1R, a member of the neurokinin family of G protein-coupled receptors, and is involved in neurogenic inflammation and immune responses in several organs, exerting physiological and pathological activities such as nociception, inflammation, angiogenesis, and wound healing (274-276). SP is mainly released by corneal nerves originating from the trigeminal ganglion. SP has been reported to affect corneal wound healing and ocular inflammatory response via NK1R interaction (76, 77, 277). Furthermore, NK1R antagonism improved DED signs by inhibiting APCs maturation and Th17 cell activation in vivo, and elevated SP levels in co-cultured trigeminal neuronal cells isolated from DED mice promoted corneal hemangiogenesis *in vitro* (266, 267, 278).

To evaluate the association between the SP/NK1R system and pathological corneal lymphangiogenesis in DED, we established a DED mouse model utilizing CEC and evaluated whether the CEC-induced DED mouse model effectively induced corneal lymphangiogenesis (Fig. 3.1). HDLECs were then incubated to evaluate the direct effect of SP on lymphangiogenesis as various factors such as activation of inflammatory/immune cells and the effect of the surrounding tissue environment can influence pathological lymphangiogenesis *in vivo* (279). We first confirmed that HDLECs expressed NK1R (Fig. 3.2). Then, we determined

the effects of exogenous SP and NK1R antagonist (L733,060) on lymphangiogenesis using an *in vitro* angiogenesis assay. SP potently activated the proliferation and tube formation of HDLECs, and the NK1R antagonist, along with SP, effectively ameliorated SP-induced lymphangiogenesis (Fig. 3.3 and 3.4), whereas SP had minimal effects on the migration of HDLECs (Fig. 3.5). The minimal effect of tube formation was consistent with a previous report on the SP-induced hemangiogenic properties of vascular endothelial cells (266). To elucidate the mechanism by which the SP/NK1R system involves changes in lymphangiogenesis, the expression of VEGFR3, a main regulatory receptor of lymphangiogenesis, was analyzed by western blotting in HDLECs. We found an increase in endogenous VEGFR3 expression by SP and inhibition of these changes by the NK1R antagonist in western blot analysis (Fig. 3.6). To exclude the off-target effect of the NK1R antagonist on the regulation of VEGFR3 expression by the SP/NK1R system, we incubated HDLECs and transfected HDLECs with NK1R-targeted siRNA with or without SP and conducted gel electrophoresis of PCR products and tube formation assay. Knockdown of NK1R significantly suppressed SP-induced upregulation of VEGFR3 expression and SP-induced increase in tube formation in gel electrophoresis of PCR products and tube formation assay, respectively (Fig. 3.7). These findings suggest that the SP/NK1R system induces lymphangiogenesis through VEGFR3 overexpression. Based on a previous report that SP induces VEGFR1 overexpression in human esophageal squamous cell carcinoma related to tumor-associated angiogenesis (280), we suggest that SP promotes corneal lymphangiogenesis through increased expression of VEGFR3 via a similar mechanism.

Next, we examined the role of SP/NK1R pathway in corneal lymphangiogenesis *in vivo*. Subconjunctival NK1R antagonist injection significantly attenuated pathological corneal lymphangiogenesis and improved clinical signs in the CEC-induced DED mouse model (Fig. 3.8 and 3.9). Thereafter, we performed an NK1R inhibition test comparing control siRNA, siNK1R, or NK1R antagonist through subconjunctival injection of corneal disepithelialization model, a robust in vivo model for corneal lymphangiogenesis to exclude off-target effects of the NK1R antagonist, confirming that siNK1R and NK1R antagonist treatment significantly reduced the area of lymphatic vessels compared to control siRNA treatment (Fig. 3.10). To further investigate the mechanism of corneal lymphangiogenesis, mRNA expression of

endogenous SP and pro-lymphangiogenic factors was evaluated in corneal and conjunctival tissues of a CEC-induced dry eye mouse model. NK1R antagonist remarkably suppressed the increased expression of VEGFR3, VEGF-C, VEGF-D, and endogenous SP (Fig. 3.11). Taken together with the *in vitro* and *in vivo* findings, we suggest that the SP/NK1R system induces VEGFR3 overexpression on the ocular surface, which leads to corneal lymphangiogenesis.

REFERENCES

1. Lee, S. J., Kim, S., Jo, D. H., Cho, C. S., Kim, S. R., Kang, D., Chae, J., Yoo, D. K., Ha, S., Chung, J., and Kim, J. H. (2021) Specific ablation of PDGFRβ-overexpressing pericytes with antibody-drug conjugate potently inhibits pathologic ocular neovascularization in mouse models. *Commun Med (Lond)* **1**, 58
2. Lee, S. J., Kim, S. J., Jo, D. H., Park, K. S., and Kim, J. H. (2021) Blockade of mTORC1-NOX signaling pathway inhibits TGF-β1-mediated senescence-like structural alterations of the retinal pigment epithelium. *Faseb j* **35**, e21403
3. Lee, S. J., Im, S. T., Wu, J., Cho, C. S., Jo, D. H., Chen, Y., Dana, R., Kim, J. H., and Lee, S. M. (2021) Corneal lymphangiogenesis in dry eye disease is regulated by substance P/neurokinin-1 receptor system through controlling expression of vascular endothelial growth factor receptor 3. *Ocul Surf* **22**, 72-79
4. Carmeliet, P., and Jain, R. K. (2000) Angiogenesis in cancer and other diseases. *Nature* **407**, 249-257
5. Qazi, Y., Maddula, S., and Ambati, B. K. (2009) Mediators of ocular angiogenesis. *J Genet* **88**, 495-515
6. Daruich, A., Matet, A., Moulin, A., Kowalczuk, L., Nicolas, M., Sellam, A., Rothschild, P. R., Omri, S., Gélizé, E., Jonet, L., Delaunay, K., De Kozak, Y., Berdugo, M., Zhao, M., Crisanti, P., and Behar-Cohen, F. (2018) Mechanisms of macular edema: Beyond the surface. *Prog Retin Eye Res* **63**, 20-68
7. Nicholas, M. P., and Mysore, N. (2021) Corneal neovascularization. *Exp Eye Res* **202**, 108363
8. Roshandel, D., Eslani, M., Baradaran-Rafii, A., Cheung, A. Y., Kurji, K., Jabbehdari, S., Maiz, A., Jalali, S., Djalilian, A. R., and Holland, E. J. (2018) Current and emerging therapies for corneal neovascularization. *Ocul Surf* **16**, 398-414
9. Rubio, R. G., and Adamis, A. P. (2016) Ocular Angiogenesis: Vascular Endothelial Growth Factor and Other Factors. *Dev Ophthalmol* **55**, 28-37
10. Lin, F. L., Wang, P. Y., Chuang, Y. F., Wang, J. H., Wong, V. H. Y., Bui, B. V., and Liu, G. S. (2020) Gene Therapy Intervention in Neovascular Eye Disease: A Recent Update. *Mol Ther* **28**, 2120-2138
11. Amador, C., Shah, R., Ghiam, S., Kramerov, A. A., and Ljubimov, A. V. (2022) Gene Therapy in the Anterior Eye Segment. *Curr Gene Ther* **22**, 104-131
12. Jiménez-Gómez, Y., Alba-Molina, D., Blanco-Blanco, M., Pérez-Fajardo, L., Reyes-Ortega, F., Ortega-Llamas, L., Villalba-González, M., Fernández-Choquet de Isla, I., Pugliese, F., Stoikow, I., and González-Andrades, M. (2022) Novel Treatments for Age-Related Macular Degeneration: A Review of Clinical Advances in Sustained Drug Delivery Systems. *Pharmaceutics* **14**
13. Maddula, S., Davis, D. K., Maddula, S., Burrow, M. K., and Ambati, B. K. (2011) Horizons in therapy for corneal angiogenesis. *Ophthalmology* **118**, 591-599
14. Campochiaro, P. A. (2015) Molecular pathogenesis of retinal and choroidal vascular diseases. *Progress in Retinal and Eye Research* **49**, 67-81
15. Sonmez, K., Drenser, K. A., Capone, A., Jr., and Trese, M. T. (2008) Vitreous levels of stromal cell-derived factor 1 and vascular endothelial growth factor in patients with retinopathy of prematurity. *Ophthalmology* **115**, 1065-1070.e1061
16. Sato, T., Kusaka, S., Shimojo, H., and Fujikado, T. (2009) Simultaneous analyses of vitreous levels of 27 cytokines in eyes with retinopathy of prematurity. *Ophthalmology* **116**, 2165-2169
17. Ma, J., Mehta, M., Lam, G., Cyr, D., Ng, T. F., Hirose, T., Tawansy, K. A., Taylor, A. W., and Lashkari, K. (2014) Influence of subretinal fluid in advanced stage retinopathy of prematurity on proangiogenic response and cell proliferation. *Mol Vis* **20**, 881-893

18. Aiello, L. P., Avery, R. L., Arrigg, P. G., Keyt, B. A., Jampel, H. D., Shah, S. T., Pasquale, L. R., Thieme, H., Iwamoto, M. A., Park, J. E., and et al. (1994) Vascular endothelial growth factor in ocular fluid of patients with diabetic retinopathy and other retinal disorders. *N Engl J Med* **331**, 1480-1487
19. Selim, K. M., Sahan, D., Muhittin, T., Osman, C., and Mustafa, O. (2010) Increased levels of vascular endothelial growth factor in the aqueous humor of patients with diabetic retinopathy. *Indian J Ophthalmol* **58**, 375-379
20. Nawaz, I. M., Rezzola, S., Cancarini, A., Russo, A., Costagliola, C., Semeraro, F., and Presta, M. (2019) Human vitreous in proliferative diabetic retinopathy: Characterization and translational implications. *Prog Retin Eye Res* **72**, 100756
21. Wells, J. A., Murthy, R., Chibber, R., Nunn, A., Molinatti, P. A., Kohner, E. M., and Gregor, Z. J. (1996) Levels of vascular endothelial growth factor are elevated in the vitreous of patients with subretinal neovascularisation. *Br J Ophthalmol* **80**, 363-366
22. Funk, M., Karl, D., Georgopoulos, M., Benesch, T., Sacu, S., Polak, K., Zlabinger, G. J., and Schmidt-Erfurth, U. (2009) Neovascular age-related macular degeneration: intraocular cytokines and growth factors and the influence of therapy with ranibizumab. *Ophthalmology* **116**, 2393-2399
23. Sawada, O., Miyake, T., Kakinoki, M., Sawada, T., Kawamura, H., and Ohji, M. (2010) Aqueous vascular endothelial growth factor after intravitreal injection of pegaptanib or ranibizumab in patients with age-related macular degeneration. *Retina* **30**, 1034-1038
24. Bednarz, J., Weich, H. A., Rodokanaki-von Schrenck, A., and Engelmann, K. (1995) Expression of genes coding growth factors and growth factor receptors in differentiated and dedifferentiated human corneal endothelial cells. *Cornea* **14**, 372-381
25. Philipp, W., Speicher, L., and Humpel, C. (2000) Expression of vascular endothelial growth factor and its receptors in inflamed and vascularized human corneas. *Invest Ophthalmol Vis Sci* **41**, 2514-2522
26. Stahl, A., Krohne, T. U., Eter, N., Oberacher-Velten, I., Guthoff, R., Meltendorf, S., Ehrt, O., Aisenbrey, S., Roider, J., Gerding, H., Jandeck, C., Smith, L. E. H., and Walz, J. M. (2018) Comparing Alternative Ranibizumab Dosages for Safety and Efficacy in Retinopathy of Prematurity: A Randomized Clinical Trial. *JAMA Pediatr* **172**, 278-286
27. Wallace, D. K., Dean, T. W., Hartnett, M. E., Kong, L., Smith, L. E., Hubbard, G. B., McGregor, M. L., Jordan, C. O., Mantagos, I. S., Bell, E. F., and Kraker, R. T. (2018) A Dosing Study of Bevacizumab for Retinopathy of Prematurity: Late Recurrences and Additional Treatments. *Ophthalmology* **125**, 1961-1966
28. Stahl, A., Bründer, M. C., Lagrèze, W. A., Molnár, F. E., Barth, T., Eter, N., Guthoff, R., Krohne, T. U., and Pfeil, J. M. (2022) Ranibizumab in retinopathy of prematurity - one-year follow-up of ophthalmic outcomes and two-year follow-up of neurodevelopmental outcomes from the CARE-ROP study. *Acta Ophthalmol* **100**, e91-e99
29. Elman, M. J., Aiello, L. P., Beck, R. W., Bressler, N. M., Bressler, S. B., Edwards, A. R., Ferris, F. L., 3rd, Friedman, S. M., Glassman, A. R., Miller, K. M., Scott, I. U., Stockdale, C. R., and Sun, J. K. (2010) Randomized trial evaluating ranibizumab plus prompt or deferred laser or triamcinolone plus prompt laser for diabetic macular edema. *Ophthalmology* **117**, 1064-1077.e1035
30. Wells, J. A., Glassman, A. R., Ayala, A. R., Jampol, L. M., Aiello, L. P., Antoszyk, A. N., Arnold-Bush, B., Baker, C. W., Bressler, N. M., Browning, D. J., Elman, M. J., Ferris, F. L., Friedman, S. M., Melia, M., Pieramici, D. J., Sun, J. K., and Beck, R. W. (2015) Aflibercept, bevacizumab, or ranibizumab for diabetic macular edema. *N Engl J Med* **372**, 1193-1203
31. Solomon, S. D., Chew, E., Duh, E. J., Sobrin, L., Sun, J. K., VanderBeek, B. L., Wykoff, C. C., and Gardner, T. W. (2017) Diabetic Retinopathy: A Position Statement by the American Diabetes Association. *Diabetes Care* **40**, 412-418

32. Heier, J. S., Brown, D. M., Chong, V., Korobelnik, J. F., Kaiser, P. K., Nguyen, Q. D., Kirchhof, B., Ho, A., Ogura, Y., Yancopoulos, G. D., Stahl, N., Vitti, R., Berliner, A. J., Soo, Y., Anderesi, M., Groetzbach, G., Sommerauer, B., Sandbrink, R., Simader, C., and Schmidt-Erfurth, U. (2012) Intravitreal aflibercept (VEGF trap-eye) in wet age-related macular degeneration. *Ophthalmology* 119, 2537-2548
33. Martin, D. F., Maguire, M. G., Fine, S. L., Ying, G. S., Jaffe, G. J., Grunwald, J. E., Toth, C., Redford, M., and Ferris, F. L., 3rd. (2012) Ranibizumab and bevacizumab for treatment of neovascular age-related macular degeneration: two-year results. *Ophthalmology* 119, 1388-1398
34. Ho, A. C., Busbee, B. G., Regillo, C. D., Wieland, M. R., Van Everen, S. A., Li, Z., Rubio, R. G., and Lai, P. (2014) Twenty-four-month efficacy and safety of 0.5 mg or 2.0 mg ranibizumab in patients with subfoveal neovascular age-related macular degeneration. *Ophthalmology* 121, 2181-2192
35. Dastjerdi, M. H., Sadrai, Z., Saban, D. R., Zhang, Q., and Dana, R. (2011) Corneal penetration of topical and subconjunctival bevacizumab. *Invest Ophthalmol Vis Sci* 52, 8718-8723
36. Kim, Y. C., Grossniklaus, H. E., Edelhauser, H. F., and Prausnitz, M. R. (2014) Intrastromal delivery of bevacizumab using microneedles to treat corneal neovascularization. *Invest Ophthalmol Vis Sci* 55, 7376-7386
37. Liarakos, V. S., Papaconstantinou, D., Vergados, I., Douvali, M., and Theodossiadis, P. G. (2014) The effect of subconjunctival ranibizumab on corneal and anterior segment neovascularization: study on an animal model. *Eur J Ophthalmol* 24, 299-308
38. Snyder, L. L., Garcia-Gonzalez, J. M., Shapiro, M. J., and Blair, M. P. (2016) Very Late Reactivation of Retinopathy of Prematurity After Monotherapy With Intravitreal Bevacizumab. *Ophthalmic Surg Lasers Imaging Retina* 47, 280-283
39. Yang, S., Zhao, J., and Sun, X. (2016) Resistance to anti-VEGF therapy in neovascular age-related macular degeneration: a comprehensive review. *Drug Des Devel Ther* 10, 1857-1867
40. Hajrasouliha, A. R., Garcia-Gonzales, J. M., Shapiro, M. J., Yoon, H., and Blair, M. P. (2017) Reactivation of Retinopathy of Prematurity Three Years After Treatment With Bevacizumab. *Ophthalmic Surg Lasers Imaging Retina* 48, 255-259
41. Mettu, P. S., Allingham, M. J., and Cousins, S. W. (2021) Incomplete response to Anti-VEGF therapy in neovascular AMD: Exploring disease mechanisms and therapeutic opportunities. *Prog Retin Eye Res* 82, 100906
42. Rofagha, S., Bhisitkul, R. B., Boyer, D. S., Sadda, S. R., and Zhang, K. (2013) Seven-year outcomes in ranibizumab-treated patients in ANCHOR, MARINA, and HORIZON: a multicenter cohort study (SEVEN-UP). *Ophthalmology* 120, 2292-2299
43. Bracha, P., Moore, N. A., Ciulla, T. A., WuDunn, D., and Cantor, L. B. (2018) The acute and chronic effects of intravitreal anti-vascular endothelial growth factor injections on intraocular pressure: A review. *Surv Ophthalmol* 63, 281-295
44. Falavarjani, K. G., and Nguyen, Q. D. (2013) Adverse events and complications associated with intravitreal injection of anti-VEGF agents: a review of literature. *Eye (Lond)* 27, 787-794
45. Manousaridis, K., and Talks, J. (2012) Macular ischaemia: a contraindication for anti-VEGF treatment in retinal vascular disease? *Br J Ophthalmol* 96, 179-184
46. Arevalo, J. F., Maia, M., Flynn, H. W., Jr., Saravia, M., Avery, R. L., Wu, L., Eid Farah, M., Pieramici, D. J., Berrocal, M. H., and Sanchez, J. G. (2008) Tractional retinal detachment following intravitreal bevacizumab (Avastin) in patients with severe proliferative diabetic retinopathy. *Br J Ophthalmol* 92, 213-216
47. Avery, R. L., and Gordon, G. M. (2016) Systemic Safety of Prolonged Monthly Anti-Vascular Endothelial Growth Factor Therapy for Diabetic Macular Edema: A Systematic Review and Meta-analysis. *JAMA Ophthalmol* 134, 21-29

48. Kwon, J. W., Jee, D., and La, T. Y. (2018) The association between myocardial infarction and intravitreal bevacizumab injection. *Medicine (Baltimore)* **97**, e0198
49. Low, A., Faridi, A., Bhavsar, K. V., Cockerham, G. C., Freeman, M., Fu, R., Paynter, R., Kondo, K., and Kansagara, D. (2019) Comparative effectiveness and harms of intravitreal antivascular endothelial growth factor agents for three retinal conditions: a systematic review and meta-analysis. *Br J Ophthalmol* **103**, 442-451
50. Avery, R. L., Castellarin, A. A., Steinle, N. C., Dhoot, D. S., Pieramici, D. J., See, R., Couvillion, S., Nasir, M. A., Rabena, M. D., Maia, M., Van Everen, S., Le, K., and Hanley, W. D. (2017) SYSTEMIC PHARMACOKINETICS AND PHARMACODYNAMICS OF INTRAVITREAL AFLIBERCEPT, BEVACIZUMAB, AND RANIBIZUMAB. *Retina* **37**, 1847-1858
51. Yu, C. Q., Zhang, M., Matis, K. I., Kim, C., and Rosenblatt, M. I. (2008) Vascular endothelial growth factor mediates corneal nerve repair. *Invest Ophthalmol Vis Sci* **49**, 3870-3878
52. Saint-Geniez, M., Kurihara, T., Sekiyama, E., Maldonado, A. E., and D'Amore, P. A. (2009) An essential role for RPE-derived soluble VEGF in the maintenance of the choriocapillaris. *Proc Natl Acad Sci U S A* **106**, 18751-18756
53. Brar, V. S., Sharma, R. K., Murthy, R. K., and Chalam, K. V. (2010) Bevacizumab neutralizes the protective effect of vascular endothelial growth factor on retinal ganglion cells. *Mol Vis* **16**, 1848-1853
54. Kurihara, T., Westenskow, P. D., Bravo, S., Aguilar, E., and Friedlander, M. (2012) Targeted deletion of Vegfa in adult mice induces vision loss. *J Clin Invest* **122**, 4213-4217
55. Usui, Y., Westenskow, P. D., Kurihara, T., Aguilar, E., Sakimoto, S., Paris, L. P., Wittgrove, C., Feitelberg, D., Friedlander, M. S., Moreno, S. K., Dorrell, M. I., and Friedlander, M. (2015) Neurovascular crosstalk between interneurons and capillaries is required for vision. *J Clin Invest* **125**, 2335-2346
56. Smith, L. E., Wesolowski, E., McLellan, A., Kostyk, S. K., D'Amato, R., Sullivan, R., and D'Amore, P. A. (1994) Oxygen-induced retinopathy in the mouse. *Invest Ophthalmol Vis Sci* **35**, 101-111
57. Scott, A., and Fruttiger, M. (2010) Oxygen-induced retinopathy: a model for vascular pathology in the retina. *Eye* **24**, 416-421
58. Rübsam, A., Parikh, S., and Fort, P. (2018) Role of Inflammation in Diabetic Retinopathy. *International Journal of Molecular Sciences* **19**, 942
59. Zeng, X. X., Ng, Y. K., and Ling, E. A. (2000) Neuronal and microglial response in the retina of streptozotocin-induced diabetic rats. *Vis Neurosci* **17**, 463-471
60. Krady, J. K., Basu, A., Allen, C. M., Xu, Y., LaNoue, K. F., Gardner, T. W., and Levison, S. W. (2005) Minocycline reduces proinflammatory cytokine expression, microglial activation, and caspase-3 activation in a rodent model of diabetic retinopathy. *Diabetes* **54**, 1559-1565
61. Ibrahim, A. S., El-Remessy, A. B., Matragoon, S., Zhang, W., Patel, Y., Khan, S., Al-Gayyar, M. M., El-Shishtawy, M. M., and Liou, G. I. (2011) Retinal microglial activation and inflammation induced by amadori-glycated albumin in a rat model of diabetes. *Diabetes* **60**, 1122-1133
62. Jo, D. H., Yun, J.-H., Cho, C. S., Kim, J. H., Kim, J. H., and Cho, C.-H. (2019) Interaction between microglia and retinal pigment epithelial cells determines the integrity of outer blood-retinal barrier in diabetic retinopathy. *Glia* **67**, 321-331
63. Zeng, H. Y., Green, W. R., and Tso, M. O. (2008) Microglial activation in human diabetic retinopathy. *Arch Ophthalmol* **126**, 227-232
64. Colijn, J. M., Buitendijk, G. H. S., Prokofyeva, E., Alves, D., Cachulo, M. L., Khawaja, A. P., Cougnard-Gregoire, A., Merle, B. M. J., Korb, C., Erke, M. G., Bron, A., Anastasopoulos, E., Meester-Smoor, M. A., Segato, T., Piermarocchi, S., de Jong, P., Vingerling, J. R., Topouzis, F., Creuzot-Garcher, C., Bertelsen, G., Pfeiffer, N., Fletcher, A. E., Foster, P. J., Silva, R., Korobelnik, J. F., Delcourt, C., and Klaver, C. C. W. (2017) Prevalence of Age-Related Macular Degeneration in

Europe: The Past and the Future. *Ophthalmology* 124, 1753-1763
65. Garcia-Garcia, J., Usategui-Martin, R., Sanabria, M. R., Fernandez-Perez, E., Telleria, J. J., and Coco-Martin, R. M. (2022) Pathophysiology of Age-Related Macular Degeneration. Implications for Treatment. *Ophthalmic Res*
66. (2021) Age-related macular degeneration. *Nature Reviews Disease Primers* 7, 32
67. Bron, A. J., de Paiva, C. S., Chauhan, S. K., Bonini, S., Gabison, E. E., Jain, S., Knop, E., Markoulli, M., Ogawa, Y., Perez, V., Uchino, Y., Yokoi, N., Zoukhri, D., and Sullivan, D. A. (2017) TFOS DEWS II pathophysiology report. *Ocul Surf* 15, 438-510
68. Feizi, S., Azari, A. A., and Safapour, S. (2017) Therapeutic approaches for corneal neovascularization. *Eye Vis (Lond)* 4, 28
69. Goyal, S., Chauhan, S. K., El Annan, J., Nallasamy, N., Zhang, Q., and Dana, R. (2010) Evidence of corneal lymphangiogenesis in dry eye disease: a potential link to adaptive immunity? *Arch Ophthalmol* 128, 819-824
70. Pflugfelder, S. C., and de Paiva, C. S. (2017) The Pathophysiology of Dry Eye Disease: What We Know and Future Directions for Research. *Ophthalmology* 124, S4-s13
71. Barabino, S., Chen, Y., Chauhan, S., and Dana, R. (2012) Ocular surface immunity: homeostatic mechanisms and their disruption in dry eye disease. *Prog Retin Eye Res* 31, 271-285
72. Lasagni Vitar, R. M., Rama, P., and Ferrari, G. (2022) The two-faced effects of nerves and neuropeptides in corneal diseases. *Prog Retin Eye Res* 86, 100974
73. Stern, M. E., Gao, J., Siemasko, K. F., Beuerman, R. W., and Pflugfelder, S. C. (2004) The role of the lacrimal functional unit in the pathophysiology of dry eye. *Exp Eye Res* 78, 409-416
74. Troger, J., Kieselbach, G., Teuchner, B., Kralinger, M., Nguyen, Q. A., Haas, G., Yayan, J., Göttinger, W., and Schmid, E. (2007) Peptidergic nerves in the eye, their source and potential pathophysiological relevance. *Brain Res Rev* 53, 39-62
75. Baudouin, C., Irkeç, M., Messmer, E. M., Benítez-Del-Castillo, J. M., Bonini, S., Figueiredo, F. C., Geerling, G., Labetoulle, M., Lemp, M., Rolando, M., Van Setten, G., and Aragona, P. (2018) Clinical impact of inflammation in dry eye disease: proceedings of the ODISSEY group meeting. *Acta Ophthalmol* 96, 111-119
76. Słoniecka, M., Le Roux, S., Zhou, Q., and Danielson, P. (2016) Substance P Enhances Keratocyte Migration and Neutrophil Recruitment through Interleukin-8. *Mol Pharmacol* 89, 215-225
77. Suvas, S. (2017) Role of Substance P Neuropeptide in Inflammation, Wound Healing, and Tissue Homeostasis. *J Immunol* 199, 1543-1552
78. Bignami, F., Giacomini, C., Lorusso, A., Aramini, A., Rama, P., and Ferrari, G. (2014) NK1 receptor antagonists as a new treatment for corneal neovascularization. *Invest Ophthalmol Vis Sci* 55, 6783-6794
79. Barbariga, M., Fonteyne, P., Ostadreza, M., Bignami, F., Rama, P., and Ferrari, G. (2018) Substance P Modulation of Human and Murine Corneal Neovascularization. *Invest Ophthalmol Vis Sci* 59, 1305-1312
80. Cavallaro, G., Filippi, L., Bagnoli, P., La Marca, G., Cristofori, G., Raffaeli, G., Padrini, L., Araimo, G., Fumagalli, M., Groppo, M., Dal Monte, M., Osnaghi, S., Fiorini, P., and Mosca, F. (2014) The pathophysiology of retinopathy of prematurity: an update of previous and recent knowledge. *Acta Ophthalmol* 92, 2-20
81. Chen, J., and Smith, L. E. (2007) Retinopathy of prematurity. *Angiogenesis* 10, 133-140
82. Hartnett, M. E., and Penn, J. S. (2012) Mechanisms and management of retinopathy of prematurity. *N Engl J Med* 367, 2515-2526
83. Hellström, A., Smith, L. E., and Dammann, O. (2013) Retinopathy of prematurity.

Lancet 382, 1445-1457
84. Hellström, A., Engström, E., Hård, A. L., Albertsson-Wikland, K., Carlsson, B., Niklasson, A., Löfqvist, C., Svensson, E., Holm, S., Ewald, U., Holmström, G., and Smith, L. E. (2003) Postnatal serum insulin-like growth factor I deficiency is associated with retinopathy of prematurity and other complications of premature birth. *Pediatrics* 112, 1016-1020
85. Pierce, E. A., Avery, R. L., Foley, E. D., Aiello, L. P., and Smith, L. E. (1995) Vascular endothelial growth factor/vascular permeability factor expression in a mouse model of retinal neovascularization. *Proc Natl Acad Sci U S A* 92, 905-909
86. Morita, M., Ohneda, O., Yamashita, T., Takahashi, S., Suzuki, N., Nakajima, O., Kawauchi, S., Ema, M., Shibahara, S., Udono, T., Tomita, K., Tamai, M., Sogawa, K., Yamamoto, M., and Fujii-Kuriyama, Y. (2003) HLF/HIF-2alpha is a key factor in retinopathy of prematurity in association with erythropoietin. *Embo j* 22, 1134-1146
87. Chiang, M. F., Quinn, G. E., Fielder, A. R., Ostmo, S. R., Paul Chan, R. V., Berrocal, A., Binenbaum, G., Blair, M., Peter Campbell, J., Capone, A., Jr., Chen, Y., Dai, S., Ells, A., Fleck, B. W., Good, W. V., Elizabeth Hartnett, M., Holmstrom, G., Kusaka, S., Kychenthal, A., Lepore, D., Lorenz, B., Martinez-Castellanos, M. A., Özdek, Ş., Ademola-Popoola, D., Reynolds, J. D., Shah, P. K., Shapiro, M., Stahl, A., Toth, C., Vinekar, A., Visser, L., Wallace, D. K., Wu, W. C., Zhao, P., and Zin, A. (2021) International Classification of Retinopathy of Prematurity, Third Edition. *Ophthalmology* 128, e51-e68
88. Palmer, E. A., Hardy, R. J., Dobson, V., Phelps, D. L., Quinn, G. E., Summers, C. G., Krom, C. P., and Tung, B. (2005) 15-year outcomes following threshold retinopathy of prematurity: final results from the multicenter trial of cryotherapy for retinopathy of prematurity. *Arch Ophthalmol* 123, 311-318
89. Tasman, W. (1988) Multicenter trial of cryotherapy for retinopathy of prematurity. *Arch Ophthalmol* 106, 463-464
90. (2003) Revised indications for the treatment of retinopathy of prematurity: results of the early treatment for retinopathy of prematurity randomized trial. *Arch Ophthalmol* 121, 1684-1694
91. Good, W. V. (2004) Final results of the Early Treatment for Retinopathy of Prematurity (ETROP) randomized trial. *Trans Am Ophthalmol Soc* 102, 233-248; discussion 248-250
92. Chan-Ling, T., Gole, G. A., Quinn, G. E., Adamson, S. J., and Darlow, B. A. (2018) Pathophysiology, screening and treatment of ROP: A multi-disciplinary perspective. *Prog Retin Eye Res* 62, 77-119
93. Davitt, B. V., Dobson, V., Quinn, G. E., Hardy, R. J., Tung, B., and Good, W. V. (2009) Astigmatism in the Early Treatment for Retinopathy Of Prematurity Study: findings to 3 years of age. *Ophthalmology* 116, 332-339
94. Deng, L., and Gwiazda, J. E. (2012) Anisometropia in children from infancy to 15 years. *Invest Ophthalmol Vis Sci* 53, 3782-3787
95. Holmström, M., el Azazi, M., and Kugelberg, U. (1998) Ophthalmological long-term follow up of preterm infants: a population based, prospective study of the refraction and its development. *Br J Ophthalmol* 82, 1265-1271
96. Saunders, K. J., McCulloch, D. L., Shepherd, A. J., and Wilkinson, A. G. (2002) Emmetropisation following preterm birth. *Br J Ophthalmol* 86, 1035-1040
97. Mintz-Hittner, H. A., Kennedy, K. A., and Chuang, A. Z. (2011) Efficacy of intravitreal bevacizumab for stage 3+ retinopathy of prematurity. *N Engl J Med* 364, 603-615
98. Feng, F., Cheng, Y., and Liu, Q. H. (2014) Bevacizumab treatment reduces retinal neovascularization in a mouse model of retinopathy of prematurity. *Int J Ophthalmol* 7, 608-613
99. Hartnett, M. E., Martiniuk, D., Byfield, G., Geisen, P., Zeng, G., and Bautch, V. L. (2008) Neutralizing VEGF decreases tortuosity and alters endothelial cell

division orientation in arterioles and veins in a rat model of ROP: relevance to plus disease. *Invest Ophthalmol Vis Sci* **49**, 3107-3114
100. Heiduschka, P., Plagemann, T., Li, L., Alex, A. F., and Eter, N. (2019) Different effects of various anti-angiogenic treatments in an experimental mouse model of retinopathy of prematurity. *Clin Exp Ophthalmol* **47**, 79-87
101. Sankar, M. J., Sankar, J., and Chandra, P. (2018) Anti-vascular endothelial growth factor (VEGF) drugs for treatment of retinopathy of prematurity. *Cochrane Database Syst Rev* **1**, Cd009734
102. Mintz-Hittner, H. A., Geloneck, M. M., and Chuang, A. Z. (2016) Clinical Management of Recurrent Retinopathy of Prematurity after Intravitreal Bevacizumab Monotherapy. *Ophthalmology* **123**, 1845-1855
103. Hu, J., Blair, M. P., Shapiro, M. J., Lichtenstein, S. J., Galasso, J. M., and Kapur, R. (2012) Reactivation of retinopathy of prematurity after bevacizumab injection. *Arch Ophthalmol* **130**, 1000-1006
104. Lindahl, P., Johansson, B. R., Levéen, P., and Betsholtz, C. (1997) Pericyte loss and microaneurysm formation in PDGF-B-deficient mice. *Science* **277**, 242-245
105. Hellström, M., Kalén, M., Lindahl, P., Abramsson, A., and Betsholtz, C. (1999) Role of PDGF-B and PDGFR-beta in recruitment of vascular smooth muscle cells and pericytes during embryonic blood vessel formation in the mouse. *Development* **126**, 3047-3055
106. Raica, M., and Cimpean, A. M. (2010) Platelet-Derived Growth Factor (PDGF)/PDGF Receptors (PDGFR) Axis as Target for Antitumor and Antiangiogenic Therapy. *Pharmaceuticals (Basel)* **3**, 572-599
107. Huang, H. (2020) Pericyte-Endothelial Interactions in the Retinal Microvasculature. *Int J Mol Sci* **21**
108. Drago, J. Z., Modi, S., and Chandarlapaty, S. (2021) Unlocking the potential of antibody–drug conjugates for cancer therapy. *Nature Reviews Clinical Oncology* **18**, 327-344
109. Kim, S., Kim, H., Jo, D. H., Kim, J. H., Kim, S. R., Kang, D., Hwang, D., and Chung, J. (2019) Bispecific anti-mPDGFRβ x cotinine scFv-C(κ)-scFv fusion protein and cotinine-duocarmycin can form antibody-drug conjugate-like complexes that exert cytotoxicity against mPDGFRβ expressing cells. *Methods* **154**, 125-135
110. Connor, K. M., Krah, N. M., Dennison, R. J., Aderman, C. M., Chen, J., Guerin, K. I., Sapieha, P., Stahl, A., Willett, K. L., and Smith, L. E. (2009) Quantification of oxygen-induced retinopathy in the mouse: a model of vessel loss, vessel regrowth and pathological angiogenesis. *Nat Protoc* **4**, 1565-1573
111. Vähätupa, M., Jääskeläinen, N., Cerrada-Gimenez, M., Thapa, R., Järvinen, T., Kalesnykas, G., and Uusitalo-Järvinen, H. (2020) Oxygen-Induced Retinopathy Model for Ischemic Retinal Diseases in Rodents. *J Vis Exp*
112. Shweiki, D., Itin, A., Soffer, D., and Keshet, E. (1992) Vascular endothelial growth factor induced by hypoxia may mediate hypoxia-initiated angiogenesis. *Nature* **359**, 843-845
113. Adamis, A. P., Miller, J. W., Bernal, M. T., D'Amico, D. J., Folkman, J., Yeo, T. K., and Yeo, K. T. (1994) Increased vascular endothelial growth factor levels in the vitreous of eyes with proliferative diabetic retinopathy. *Am J Ophthalmol* **118**, 445-450
114. Ferrara, N. (2016) VEGF and Intraocular Neovascularization: From Discovery to Therapy. *Transl Vis Sci Technol* **5**, 10
115. Hansen, E. D., and Hartnett, M. E. (2019) A review of treatment for retinopathy of prematurity. *Expert Rev Ophthalmol* **14**, 73-87
116. Hartnett, M. E. (2020) Retinopathy of Prematurity: Evolving Treatment With Anti-Vascular Endothelial Growth Factor. *Am J Ophthalmol* **218**, 208-213
117. Levéen, P., Pekny, M., Gebre-Medhin, S., Swolin, B., Larsson, E., and Betsholtz, C. (1994) Mice deficient for PDGF B show renal, cardiovascular, and hematological abnormalities. *Genes Dev* **8**, 1875-1887

118. Armulik, A., Abramsson, A., and Betsholtz, C. (2005) Endothelial/pericyte interactions. *Circ Res* **97**, 512-523
119. Benjamin, L. E., Hemo, I., and Keshet, E. (1998) A plasticity window for blood vessel remodelling is defined by pericyte coverage of the preformed endothelial network and is regulated by PDGF-B and VEGF. *Development* **125**, 1591-1598
120. Vasudev, N. S., and Reynolds, A. R. (2014) Anti-angiogenic therapy for cancer: current progress, unresolved questions and future directions. *Angiogenesis* **17**, 471-494
121. Franco, M., Roswall, P., Cortez, E., Hanahan, D., and Pietras, K. (2011) Pericytes promote endothelial cell survival through induction of autocrine VEGF-A signaling and Bcl-w expression. *Blood* **118**, 2906-2917
122. Zhu, D., Chen, C., and Shi, W. (2015) Variations of Vascular Endothelial Growth Factor and Pigment Epithelial-derived Factor Are Related to Retinopathy of Prematurity in Human Babies. *West Indian Med J* **65**, 251-255
123. Hartmann, J. S., Thompson, H., Wang, H., Kanekar, S., Huang, W., Budd, S. J., and Hartnett, M. E. (2011) Expression of vascular endothelial growth factor and pigment epithelial-derived factor in a rat model of retinopathy of prematurity. *Mol Vis* **17**, 1577-1587
124. Dubrac, A., Künzel, S. E., Künzel, S. H., Li, J., Chandran, R. R., Martin, K., Greif, D. M., Adams, R. H., and Eichmann, A. (2018) NCK-dependent pericyte migration promotes pathological neovascularization in ischemic retinopathy. *Nat Commun* **9**, 3463
125. Mabry, R., Gilbertson, D. G., Frank, A., Vu, T., Ardourel, D., Ostrander, C., Stevens, B., Julien, S., Franke, S., Meengs, B., Brody, J., Presnell, S., Hamacher, N. B., Lantry, M., Wolf, A., Bukowski, T., Rosler, R., Yen, C., Anderson-Haley, M., Brasel, K., Pan, Q., Franklin, H., Thompson, P., Dodds, M., Underwood, S., Peterson, S., Sivakumar, P. V., and Snavely, M. (2010) A dual-targeting PDGFRbeta/VEGF-A molecule assembled from stable antibody fragments demonstrates anti-angiogenic activity in vitro and in vivo. *MAbs* **2**, 20-34
126. Strittmatter, K., Pomeroy, H., and Marneros, A. G. (2016) Targeting Platelet-Derived Growth Factor Receptor β(+) Scaffold Formation Inhibits Choroidal Neovascularization. *Am J Pathol* **186**, 1890-1899
127. Dunn, E. N., Hariprasad, S. M., and Sheth, V. S. (2017) An Overview of the Fovista and Rinucumab Trials and the Fate of Anti-PDGF Medications. *Ophthalmic Surg Lasers Imaging Retina* **48**, 100-104
128. Loganzo, F., Tan, X., Sung, M., Jin, G., Myers, J. S., Melamud, E., Wang, F., Diesl, V., Follettie, M. T., Musto, S., Lam, M. H., Hu, W., Charati, M. B., Khandke, K., Kim, K. S., Cinque, M., Lucas, J., Graziani, E., Maderna, A., O'Donnell, C. J., Arndt, K. T., and Gerber, H. P. (2015) Tumor cells chronically treated with a trastuzumab-maytansinoid antibody-drug conjugate develop varied resistance mechanisms but respond to alternate treatments. *Mol Cancer Ther* **14**, 952-963
129. García-Alonso, S., Ocaña, A., and Pandiella, A. (2018) Resistance to Antibody-Drug Conjugates. *Cancer Res* **78**, 2159-2165
130. Buecheler, J. W., Winzer, M., Tonillo, J., Weber, C., and Gieseler, H. (2018) Impact of Payload Hydrophobicity on the Stability of Antibody-Drug Conjugates. *Mol Pharm* **15**, 2656-2664
131. Lee, S., Elaskandrany, M., Lau, L. F., Lazzaro, D., Grant, M. B., and Chaqour, B. (2017) Interplay between CCN1 and Wnt5a in endothelial cells and pericytes determines the angiogenic outcome in a model of ischemic retinopathy. *Sci Rep* **7**, 1405
132. Choi, S. H., Chung, M., Park, S. W., Jeon, N. L., Kim, J. H., and Yu, Y. S. (2018) Relationship between Pericytes and Endothelial Cells in Retinal Neovascularization: A Histological and Immunofluorescent Study of Retinal Angiogenesis. *Korean J Ophthalmol* **32**, 70-76
133. Park, D. Y., Lee, J., Kim, J., Kim, K., Hong, S., Han, S., Kubota, Y., Augustin, H. G., Ding, L., Kim, J. W., Kim, H., He, Y., Adams, R. H., and Koh, G. Y. (2017)

Plastic roles of pericytes in the blood-retinal barrier. *Nat Commun* 8, 15296
134. Daruich, A., Matet, A., Moulin, A., Kowalczuk, L., Nicolas, M., Sellam, A., Rothschild, P.-R., Omri, S., Gélizé, E., Jonet, L., Delaunay, K., De Kozak, Y., Berdugo, M., Zhao, M., Crisanti, P., and Behar-Cohen, F. (2018) Mechanisms of macular edema: Beyond the surface. *Progress in Retinal and Eye Research* 63, 20-68
135. Rudraraju, M., Narayanan, S. P., and Somanath, P. R. (2020) Regulation of blood-retinal barrier cell-junctions in diabetic retinopathy. *Pharmacological Research* 161, 105115
136. Morcos, Y., Hosie, M. J., Bauer, H. C., and Chan-Ling, T. (2001) Immunolocalization of occludin and claudin-1 to tight junctions in intact CNS vessels of mammalian retina. *J Neurocytol* 30, 107-123
137. Nishikiori, N., Osanai, M., Chiba, H., Kojima, T., Mitamura, Y., Ohguro, H., and Sawada, N. (2007) Glial cell-derived cytokines attenuate the breakdown of vascular integrity in diabetic retinopathy. *Diabetes* 56, 1333-1340
138. Wang, J., Xu, X., Elliott, M. H., Zhu, M., and Le, Y. Z. (2010) Müller cell-derived VEGF is essential for diabetes-induced retinal inflammation and vascular leakage. *Diabetes* 59, 2297-2305
139. Klaassen, I., Van Noorden, C. J., and Schlingemann, R. O. (2013) Molecular basis of the inner blood-retinal barrier and its breakdown in diabetic macular edema and other pathological conditions. *Prog Retin Eye Res* 34, 19-48
140. Park, S. W., Yun, J. H., Kim, J. H., Kim, K. W., Cho, C. H., and Kim, J. H. (2014) Angiopoietin 2 induces pericyte apoptosis via α3β1 integrin signaling in diabetic retinopathy. *Diabetes* 63, 3057-3068
141. Yun, J. H., Park, S. W., Kim, J. H., Park, Y. J., Cho, C. H., and Kim, J. H. (2016) Angiopoietin 2 induces astrocyte apoptosis via αvβ5-integrin signaling in diabetic retinopathy. *Cell Death Dis* 7, e2101
142. Shereef, H., Comyn, O., Sivaprasad, S., Hykin, P., Cheung, G., Narendran, N., and Yang, Y. C. (2014) Differences in the topographic profiles of retinal thickening in eyes with and without serous macular detachment associated with diabetic macular oedema. *Br J Ophthalmol* 98, 182-187
143. Vujosevic, S., Torresin, T., Berton, M., Bini, S., Convento, E., and Midena, E. (2017) Diabetic Macular Edema With and Without Subfoveal Neuroretinal Detachment: Two Different Morphologic and Functional Entities. *Am J Ophthalmol* 181, 149-155
144. Xu, H.-Z., and Le, Y.-Z. (2011) Significance of Outer Blood–Retina Barrier Breakdown in Diabetes and Ischemia. *Investigative Opthalmology & Visual Science* 52, 2160
145. Xu, H.-Z., Song, Z., Fu, S., Zhu, M., and Le, Y.-Z. (2011) RPE barrier breakdown in diabetic retinopathy: seeing is believing. *Journal of Ocular Biology, Diseases, and Informatics* 4, 83-92
146. Omri, S., Behar-Cohen, F., Rothschild, P.-R., Gélizé, E., Jonet, L., Jeanny, J. C., Omri, B., and Crisanti, P. (2013) PKCζ Mediates Breakdown of Outer Blood-Retinal Barriers in Diabetic Retinopathy. *PLoS ONE* 8, e81600
147. Rothschild, P.-R., Salah, S., Berdugo, M., Gélizé, E., Delaunay, K., Naud, M.-C., Klein, C., Moulin, A., Savoldelli, M., Bergin, C., Jeanny, J.-C., Jonet, L., Arsenijevic, Y., Behar-Cohen, F., and Crisanti, P. (2017) ROCK-1 mediates diabetes-induced retinal pigment epithelial and endothelial cell blebbing: Contribution to diabetic retinopathy. *Scientific Reports* 7
148. Omri, S., Omri, B., Savoldelli, M., Jonet, L., Thillaye-Goldenberg, B., Thuret, G., Gain, P., Jeanny, J. C., Crisanti, P., and Behar-Cohen, F. (2010) The outer limiting membrane (OLM) revisited: clinical implications. *Clin Ophthalmol* 4, 183-195
149. Scarinci, F., Jampol, L. M., Linsenmeier, R. A., and Fawzi, A. A. (2015) Association of Diabetic Macular Nonperfusion With Outer Retinal Disruption on Optical Coherence Tomography. *JAMA Ophthalmol* 133, 1036-1044

150. Krady, J. K., Basu, A., Allen, C. M., Xu, Y., Lanoue, K. F., Gardner, T. W., and Levison, S. W. (2005) Minocycline Reduces Proinflammatory Cytokine Expression, Microglial Activation, and Caspase-3 Activation in a Rodent Model of Diabetic Retinopathy. *Diabetes* **54**, 1559-1565
151. Karlstetter, M., Scholz, R., Rutar, M., Wong, W. T., Provis, J. M., and Langmann, T. (2015) Retinal microglia: Just bystander or target for therapy? *Progress in Retinal and Eye Research* **45**, 30-57
152. Altmann, C., and Schmidt, M. (2018) The Role of Microglia in Diabetic Retinopathy: Inflammation, Microvasculature Defects and Neurodegeneration. *International Journal of Molecular Sciences* **19**, 110
153. Omri, S., Behar-Cohen, F., De Kozak, Y., Sennlaub, F., Mafra Verissimo, L., Jonet, L., Savoldelli, M., Omri, B., and Crisanti, P. (2011) Microglia/Macrophages Migrate through Retinal Epithelium Barrier by a Transcellular Route in Diabetic Retinopathy. *The American Journal of Pathology* **179**, 942-953
154. Arroba, A. I., Alcalde-Estevez, E., García-Ramírez, M., Cazzoni, D., De La Villa, P., Sánchez-Fernández, E. M., Mellet, C. O., García Fernández, J. M., Hernández, C., Simó, R., and Valverde, Á. M. (2016) Modulation of microglia polarization dynamics during diabetic retinopathy in db / db mice. *Biochimica et Biophysica Acta (BBA) - Molecular Basis of Disease* **1862**, 1663-1674
155. Baxter, E. W., Graham, A. E., Re, N. A., Carr, I. M., Robinson, J. I., Mackie, S. L., and Morgan, A. W. (2020) Standardized protocols for differentiation of THP-1 cells to macrophages with distinct M(IFNγ+LPS), M(IL-4) and M(IL-10) phenotypes. *Journal of Immunological Methods* **478**, 112721
156. Murray, P. J., Allen, J. E., Biswas, S. K., Fisher, E. A., Gilroy, D. W., Goerdt, S., Gordon, S., Hamilton, J. A., Ivashkiv, L. B., Lawrence, T., Locati, M., Mantovani, A., Martinez, F. O., Mege, J. L., Mosser, D. M., Natoli, G., Saeij, J. P., Schultze, J. L., Shirey, K. A., Sica, A., Suttles, J., Udalova, I., van Ginderachter, J. A., Vogel, S. N., and Wynn, T. A. (2014) Macrophage activation and polarization: nomenclature and experimental guidelines. *Immunity* **41**, 14-20
157. Geraldes, P., Hiraoka-Yamamoto, J., Matsumoto, M., Clermont, A., Leitges, M., Marette, A., Aiello, L. P., Kern, T. S., and King, G. L. (2009) Activation of PKC-delta and SHP-1 by hyperglycemia causes vascular cell apoptosis and diabetic retinopathy. *Nat Med* **15**, 1298-1306
158. Tien, T., Barrette, K. F., Chronopoulos, A., and Roy, S. (2013) Effects of high glucose-induced Cx43 downregulation on occludin and ZO-1 expression and tight junction barrier function in retinal endothelial cells. *Invest Ophthalmol Vis Sci* **54**, 6518-6525
159. Holtkamp, G. M., Kijlstra, A., Peek, R., and de Vos, A. F. (2001) Retinal pigment epithelium-immune system interactions: cytokine production and cytokine-induced changes. *Prog Retin Eye Res* **20**, 29-48
160. Ponnalagu, M., Subramani, M., Jayadev, C., Shetty, R., and Das, D. (2017) Retinal pigment epithelium-secretome: A diabetic retinopathy perspective. *Cytokine* **95**, 126-135
161. Karlstetter, M., Scholz, R., Rutar, M., Wong, W. T., Provis, J. M., and Langmann, T. (2015) Retinal microglia: just bystander or target for therapy? *Prog Retin Eye Res* **45**, 30-57
162. Shapouri-Moghaddam, A., Mohammadian, S., Vazini, H., Taghadosi, M., Esmaeili, S. A., Mardani, F., Seifi, B., Mohammadi, A., Afshari, J. T., and Sahebkar, A. (2018) Macrophage plasticity, polarization, and function in health and disease. *J Cell Physiol* **233**, 6425-6440
163. Sharma, A., Choi, J. S. Y., Stefanovic, N., Al-Sharea, A., Simpson, D. S., Mukhamedova, N., Jandeleit-Dahm, K., Murphy, A. J., Sviridov, D., Vince, J. E., Ritchie, R. H., and de Haan, J. B. (2021) Specific NLRP3 Inhibition Protects Against Diabetes-Associated Atherosclerosis. *Diabetes* **70**, 772-787
164. Rungger-Brändle, E., Dosso, A. A., and Leuenberger, P. M. (2000) Glial reactivity, an early feature of diabetic retinopathy. *Invest Ophthalmol Vis Sci* **41**,

1971-1980
165. Yang, L. P., Sun, H. L., Wu, L. M., Guo, X. J., Dou, H. L., Tso, M. O., Zhao, L., and Li, S. M. (2009) Baicalein reduces inflammatory process in a rodent model of diabetic retinopathy. *Invest Ophthalmol Vis Sci* 50, 2319-2327
166. Chanput, W., Mes, J. J., and Wichers, H. J. (2014) THP-1 cell line: an in vitro cell model for immune modulation approach. *Int Immunopharmacol* 23, 37-45
167. Shirasawa, M., Sonoda, S., Terasaki, H., Arimura, N., Otsuka, H., Yamashita, T., Uchino, E., Hisatomi, T., Ishibashi, T., and Sakamoto, T. (2013) TNF-α disrupts morphologic and functional barrier properties of polarized retinal pigment epithelium. *Experimental Eye Research* 110, 59-69
168. Liu, T., Zhang, L., Joo, D., and Sun, S.-C. (2017) NF-κB signaling in inflammation. *Signal Transduction and Targeted Therapy* 2, 17023
169. Schottelius, A. J. G., Mayo, M. W., Sartor, R. B., and Baldwin, A. S. (1999) Interleukin-10 Signaling Blocks Inhibitor of κB Kinase Activity and Nuclear Factor κB DNA Binding. *Journal of Biological Chemistry* 274, 31868-31874
170. Gaucher, D., Sebah, C., Erginay, A., Haouchine, B., Tadayoni, R., Gaudric, A., and Massin, P. (2008) Optical coherence tomography features during the evolution of serous retinal detachment in patients with diabetic macular edema. *Am J Ophthalmol* 145, 289-296
171. Weinberger, D., Fink-Cohen, S., Gaton, D. D., Priel, E., and Yassur, Y. (1995) Non-retinovascular leakage in diabetic maculopathy. *Br J Ophthalmol* 79, 728-731
172. Xu, H. Z., Song, Z., Fu, S., Zhu, M., and Le, Y. Z. (2011) RPE barrier breakdown in diabetic retinopathy: seeing is believing. *J Ocul Biol Dis Infor* 4, 83-92
173. Zeng, H.-Y. (2008) Microglial Activation in Human Diabetic Retinopathy. *Archives of Ophthalmology* 126, 227
174. Nentwich, M. M., and Ulbig, M. W. (2015) Diabetic retinopathy - ocular complications of diabetes mellitus. *World J Diabetes* 6, 489-499
175. Seo, E. J., Choi, J. A., Koh, J. Y., and Yoon, Y. H. (2020) Aflibercept ameliorates retinal pericyte loss and restores perfusion in streptozotocin-induced diabetic mice. *BMJ Open Diabetes Res Care* 8
176. Monickaraj, F., McGuire, P., and Das, A. (2018) Cathepsin D plays a role in endothelial-pericyte interactions during alteration of the blood-retinal barrier in diabetic retinopathy. *Faseb j* 32, 2539-2548
177. Strauss, O. (2005) The retinal pigment epithelium in visual function. *Physiol Rev* 85, 845-881
178. Tarchick, M. J., Bassiri, P., Rohwer, R. M., and Samuels, I. S. (2016) Early Functional and Morphologic Abnormalities in the Diabetic Nyxnob Mouse Retina. *Invest Ophthalmol Vis Sci* 57, 3496-3508
179. Boynton, G. E., Stem, M. S., Kwark, L., Jackson, G. R., Farsiu, S., and Gardner, T. W. (2015) Multimodal characterization of proliferative diabetic retinopathy reveals alterations in outer retinal function and structure. *Ophthalmology* 122, 957-967
180. Cho, N. C., Poulsen, G. L., Ver Hoeve, J. N., and Nork, T. M. (2000) Selective loss of S-cones in diabetic retinopathy. *Arch Ophthalmol* 118, 1393-1400
181. Bavinger, J. C., Dunbar, G. E., Stem, M. S., Blachley, T. S., Kwark, L., Farsiu, S., Jackson, G. R., and Gardner, T. W. (2016) The Effects of Diabetic Retinopathy and Pan-Retinal Photocoagulation on Photoreceptor Cell Function as Assessed by Dark Adaptometry. *Invest Ophthalmol Vis Sci* 57, 208-217
182. Kim, D. Y., Kang, M. K., Lee, E. J., Kim, Y. H., Oh, H., Kim, S. I., Oh, S. Y., Na, W., and Kang, Y. H. (2020) Eucalyptol Inhibits Amyloid-β-Induced Barrier Dysfunction in Glucose-Exposed Retinal Pigment Epithelial Cells and Diabetic Eyes. *Antioxidants (Basel)* 9
183. Whitcup, S. M., Nussenblatt, R. B., Lightman, S. L., and Hollander, D. A. (2013) Inflammation in retinal disease. *Int J Inflam* 2013, 724648
184. Zech, J. C., Pouvreau, I., Cotinet, A., Goureau, O., Le Varlet, B., and de Kozak, Y.

(1998) Effect of cytokines and nitric oxide on tight junctions in cultured rat retinal pigment epithelium. *Invest Ophthalmol Vis Sci* 39, 1600-1608
185. Shirasawa, M., Sonoda, S., Terasaki, H., Arimura, N., Otsuka, H., Yamashita, T., Uchino, E., Hisatomi, T., Ishibashi, T., and Sakamoto, T. (2013) TNF-α disrupts morphologic and functional barrier properties of polarized retinal pigment epithelium. *Exp Eye Res* 110, 59-69
186. Cachafeiro, M., Bemelmans, A. P., Samardzija, M., Afanasieva, T., Pournaras, J. A., Grimm, C., Kostic, C., Philippe, S., Wenzel, A., and Arsenijevic, Y. (2013) Hyperactivation of retina by light in mice leads to photoreceptor cell death mediated by VEGF and retinal pigment epithelium permeability. *Cell Death Dis* 4, e781
187. Vinores, S. A., Derevjanik, N. L., Ozaki, H., Okamoto, N., and Campochiaro, P. A. (1999) Cellular mechanisms of blood-retinal barrier dysfunction in macular edema. *Doc Ophthalmol* 97, 217-228
188. Cao, L., Wang, H., and Wang, F. (2013) Amyloid-β-induced matrix metalloproteinase-9 secretion is associated with retinal pigment epithelial barrier disruption. *Int J Mol Med* 31, 1105-1112
189. Li, H., Yoneda, M., Takeyama, M., Sugita, I., Tsunekawa, H., Yamada, H., Watanabe, D., Mukai, T., Yamamura, M., Iwaki, M., and Zako, M. (2010) Effect of infliximab on tumor necrosis factor-alpha-induced alterations in retinal microvascular endothelial cells and retinal pigment epithelial cells. *J Ocul Pharmacol Ther* 26, 549-556
190. Citi, S., Guerrera, D., Spadaro, D., and Shah, J. (2014) Epithelial junctions and Rho family GTPases: the zonular signalosome. *Small GTPases* 5, 1-15
191. Godfrey, W. A. (1987) Characterization of the choroidal mast cell. *Trans Am Ophthalmol Soc* 85, 557-599
192. Apte, R. S., Chen, D. S., and Ferrara, N. (2019) VEGF in Signaling and Disease: Beyond Discovery and Development. *Cell* 176, 1248-1264
193. Bhutto, I. A., McLeod, D. S., Hasegawa, T., Kim, S. Y., Merges, C., Tong, P., and Lutty, G. A. (2006) Pigment epithelium-derived factor (PEDF) and vascular endothelial growth factor (VEGF) in aged human choroid and eyes with age-related macular degeneration. *Exp Eye Res* 82, 99-110
194. Jager, R. D., Mieler, W. F., and Miller, J. W. (2008) Age-related macular degeneration. *N Engl J Med* 358, 2606-2617
195. Miller, J. W., Le Couter, J., Strauss, E. C., and Ferrara, N. (2013) Vascular endothelial growth factor a in intraocular vascular disease. *Ophthalmology* 120, 106-114
196. Gemenetzi, M., Lotery, A. J., and Patel, P. J. (2017) Risk of geographic atrophy in age-related macular degeneration patients treated with intravitreal anti-VEGF agents. *Eye (Lond)* 31, 1-9
197. Munk, M. R., Ceklic, L., Ebneter, A., Huf, W., Wolf, S., and Zinkernagel, M. S. (2016) Macular atrophy in patients with long-term anti-VEGF treatment for neovascular age-related macular degeneration. *Acta Ophthalmol* 94, e757-e764
198. Peden, M. C., Suñer, I. J., Hammer, M. E., and Grizzard, W. S. (2015) Long-term outcomes in eyes receiving fixed-interval dosing of anti-vascular endothelial growth factor agents for wet age-related macular degeneration. *Ophthalmology* 122, 803-808
199. Li, X., Pontén, A., Aase, K., Karlsson, L., Abramsson, A., Uutela, M., Bäckström, G., Hellström, M., Boström, H., Li, H., Soriano, P., Betsholtz, C., Heldin, C. H., Alitalo, K., Ostman, A., and Eriksson, U. (2000) PDGF-C is a new protease-activated ligand for the PDGF alpha-receptor. *Nat Cell Biol* 2, 302-309
200. Campochiaro, P. A., Hackett, S. F., Vinores, S. A., Freund, J., Csaky, C., LaRochelle, W., Henderer, J., Johnson, M., Rodriguez, I. R., Friedman, Z., and et al. (1994) Platelet-derived growth factor is an autocrine growth stimulator in retinal pigmented epithelial cells. *J Cell Sci* 107 (Pt 9), 2459-2469
201. Kazlauskas, A. (2017) PDGFs and their receptors. *Gene* 614, 1-7

202. Lu, W., and Li, X. (2018) PDGFs and their receptors in vascular stem/progenitor cells: Functions and therapeutic potential in retinal vasculopathy. *Mol Aspects Med* 62, 22-32
203. Gaengel, K., Genové, G., Armulik, A., and Betsholtz, C. (2009) Endothelial-mural cell signaling in vascular development and angiogenesis. *Arterioscler Thromb Vasc Biol* 29, 630-638
204. Erber, R., Thurnher, A., Katsen, A. D., Groth, G., Kerger, H., Hammes, H. P., Menger, M. D., Ullrich, A., and Vajkoczy, P. (2004) Combined inhibition of VEGF and PDGF signaling enforces tumor vessel regression by interfering with pericyte-mediated endothelial cell survival mechanisms. *Faseb j* 18, 338-340
205. Bergers, G., and Hanahan, D. (2008) Modes of resistance to anti-angiogenic therapy. *Nat Rev Cancer* 8, 592-603
206. Chen, Z., Xu, X. H., and Hu, J. (2016) Role of pericytes in angiogenesis: focus on cancer angiogenesis and anti-angiogenic therapy. *Neoplasma* 63, 173-182
207. He, L., and Marneros, A. G. (2013) Macrophages are essential for the early wound healing response and the formation of a fibrovascular scar. *Am J Pathol* 182, 2407-2417
208. André, H., Tunik, S., Aronsson, M., and Kvanta, A. (2015) Hypoxia-Inducible Factor-1α Is Associated With Sprouting Angiogenesis in the Murine Laser-Induced Choroidal Neovascularization Model. *Invest Ophthalmol Vis Sci* 56, 6591-6604
209. Davuluri, G., Espina, V., Petricoin, E. F., 3rd, Ross, M., Deng, J., Liotta, L. A., and Glaser, B. M. (2009) Activated VEGF receptor shed into the vitreous in eyes with wet AMD: a new class of biomarkers in the vitreous with potential for predicting the treatment timing and monitoring response. *Arch Ophthalmol* 127, 613-621
210. Pongsachareonnont, P., Mak, M. Y. K., Hurst, C. P., and Lam, W. C. (2018) Neovascular age-related macular degeneration: intraocular inflammatory cytokines in the poor responder to ranibizumab treatment. *Clin Ophthalmol* 12, 1877-1885
211. Pachydaki, S. I., Jakobiec, F. A., Bhat, P., Sobrin, L., Michaud, N. A., Seshan, S. V., and D'Amico, D. J. (2012) Surgical management and ultrastructural study of choroidal neovascularization in punctate inner choroidopathy after bevacizumab. *J Ophthalmic Inflamm Infect* 2, 29-37
212. Lambert, V., Lecomte, J., Hansen, S., Blacher, S., Gonzalez, M. L., Struman, I., Sounni, N. E., Rozet, E., de Tullio, P., Foidart, J. M., Rakic, J. M., and Noel, A. (2013) Laser-induced choroidal neovascularization model to study age-related macular degeneration in mice. *Nat Protoc* 8, 2197-2211
213. Shah, R. S., Soetikno, B. T., Lajko, M., and Fawzi, A. A. (2015) A Mouse Model for Laser-induced Choroidal Neovascularization. *J Vis Exp*, e53502
214. Dugel, P. U., Koh, A., Ogura, Y., Jaffe, G. J., Schmidt-Erfurth, U., Brown, D. M., Gomes, A. V., Warburton, J., Weichselberger, A., and Holz, F. G. (2020) HAWK and HARRIER: Phase 3, Multicenter, Randomized, Double-Masked Trials of Brolucizumab for Neovascular Age-Related Macular Degeneration. *Ophthalmology* 127, 72-84
215. Khanani, A. M., Zarbin, M. A., Barakat, M. R., Albini, T. A., Kaiser, P. K., B, G., Agashivala, N., Yu, J. S., Wykoff, C. C., and MacCumber, M. W. (2022) Safety Outcomes of Brolucizumab in Neovascular Age-Related Macular Degeneration: Results From the IRIS Registry and Komodo Healthcare Map. *JAMA Ophthalmol* 140, 20-28
216. Ding, K., Shen, J., Hafiz, Z., Hackett, S. F., Silva, R. L. E., Khan, M., Lorenc, V. E., Chen, D., Chadha, R., Zhang, M., Van Everen, S., Buss, N., Fiscella, M., Danos, O., and Campochiaro, P. A. (2019) AAV8-vectored suprachoroidal gene transfer produces widespread ocular transgene expression. *J Clin Invest* 129, 4901-4911
217. Hussain, R. M., Shaukat, B. A., Ciulla, L. M., Berrocal, A. M., and Sridhar, J. (2021) Vascular Endothelial Growth Factor Antagonists: Promising Players in

the Treatment of Neovascular Age-Related Macular Degeneration. *Drug Des Devel Ther* 15, 2653-2665
218. Khanani, A. M., Thomas, M. J., Aziz, A. A., Weng, C. Y., Danzig, C. J., Yiu, G., Kiss, S., Waheed, N. K., and Kaiser, P. K. (2022) Review of gene therapies for age-related macular degeneration. *Eye (Lond)* 36, 303-311
219. Cox, J. T., Eliott, D., and Sobrin, L. (2021) Inflammatory Complications of Intravitreal Anti-VEGF Injections. *J Clin Med* 10
220. Cao, R., Bråkenhielm, E., Li, X., Pietras, K., Widenfalk, J., Ostman, A., Eriksson, U., and Cao, Y. (2002) Angiogenesis stimulated by PDGF-CC, a novel member in the PDGF family, involves activation of PDGFR-alphaalpha and -alphabeta receptors. *Faseb j* 16, 1575-1583
221. Hou, X., Kumar, A., Lee, C., Wang, B., Arjunan, P., Dong, L., Maminishkis, A., Tang, Z., Li, Y., Zhang, F., Zhang, S. Z., Wardega, P., Chakrabarty, S., Liu, B., Wu, Z., Colosi, P., Fariss, R. N., Lennartsson, J., Nussenblatt, R., Gutkind, J. S., Cao, Y., and Li, X. (2010) PDGF-CC blockade inhibits pathological angiogenesis by acting on multiple cellular and molecular targets. *Proc Natl Acad Sci U S A* 107, 12216-12221
222. Zheng, L., Zhao, C., Du, Y., Lin, X., Jiang, Y., Lee, C., Tian, G., Mi, J., Li, X., Chen, Q., Ye, Z., Huang, L., Wang, S., Ren, X., Xing, L., Chen, W., Huang, D., Gao, Z., Zhang, S., Lu, W., Tang, Z., Wang, B., Ju, R., and Li, X. (2016) PDGF-CC underlies resistance to VEGF-A inhibition and combinatorial targeting of both suppresses pathological angiogenesis more efficiently. *Oncotarget* 7, 77902-77915
223. Dahlgren, D., and Lennernäs, H. (2020) Antibody-Drug Conjugates and Targeted Treatment Strategies for Hepatocellular Carcinoma: A Drug-Delivery Perspective. *Molecules* 25
224. Lehar, S. M., Pillow, T., Xu, M., Staben, L., Kajihara, K. K., Vandlen, R., DePalatis, L., Raab, H., Hazenbos, W. L., Morisaki, J. H., Kim, J., Park, S., Darwish, M., Lee, B. C., Hernandez, H., Loyet, K. M., Lupardus, P., Fong, R., Yan, D., Chalouni, C., Luis, E., Khalfin, Y., Plise, E., Cheong, J., Lyssikatos, J. P., Strandh, M., Koefoed, K., Andersen, P. S., Flygare, J. A., Wah Tan, M., Brown, E. J., and Mariathasan, S. (2015) Novel antibody-antibiotic conjugate eliminates intracellular S. aureus. *Nature* 527, 323-328
225. Brandish, P. E., Palmieri, A., Antonenko, S., Beaumont, M., Benso, L., Cancilla, M., Cheng, M., Fayadat-Dilman, L., Feng, G., Figueroa, I., Firdos, J., Garbaccio, R., Garvin-Queen, L., Gately, D., Geda, P., Haines, C., Hseih, S., Hodges, D., Kern, J., Knudsen, N., Kwasnjuk, K., Liang, L., Ma, H., Manibusan, A., Miller, P. L., Moy, L. Y., Qu, Y., Shah, S., Shin, J. S., Stivers, P., Sun, Y., Tomazela, D., Woo, H. C., Zaller, D., Zhang, S., Zhang, Y., and Zielstorff, M. (2018) Development of Anti-CD74 Antibody-Drug Conjugates to Target Glucocorticoids to Immune Cells. *Bioconjug Chem* 29, 2357-2369
226. Heo, K., Min, S. W., Sung, H. J., Kim, H. G., Kim, H. J., Kim, Y. H., Choi, B. K., Han, S., Chung, S., Lee, E. S., Chung, J., and Kim, I. H. (2016) An aptamer-antibody complex (oligobody) as a novel delivery platform for targeted cancer therapies. *J Control Release* 229, 1-9
227. Bakri, S. J., Snyder, M. R., Reid, J. M., Pulido, J. S., Ezzat, M. K., and Singh, R. J. (2007) Pharmacokinetics of intravitreal ranibizumab (Lucentis). *Ophthalmology* 114, 2179-2182
228. Kim, H., Yoon, S., and Chung, J. (2014) In vitro and in vivo application of anti-cotinine antibody and cotinine-conjugated compounds. *BMB Rep* 47, 130-134
229. Riah, O., Dousset, J. C., Courriere, P., Stigliani, J. L., Baziard-Mouysset, G., and Belahsen, Y. (1999) Evidence that nicotine acetylcholine receptors are not the main targets of cotinine toxicity. *Toxicol Lett* 109, 21-29
230. Panda-Jonas, S., Jonas, J. B., and Jakobczyk-Zmija, M. (1996) Retinal pigment epithelial cell count, distribution, and correlations in normal human eyes. *Am J Ophthalmol* 121, 181-189

231. Bhatia, S. K., Rashid, A., Chrenek, M. A., Zhang, Q., Bruce, B. B., Klein, M., Boatright, J. H., Jiang, Y., Grossniklaus, H. E., and Nickerson, J. M. (2016) Analysis of RPE morphometry in human eyes. *Mol Vis* 22, 898-916
232. Bruban, J., Glotin, A. L., Dinet, V., Chalour, N., Sennlaub, F., Jonet, L., An, N., Faussat, A. M., and Mascarelli, F. (2009) Amyloid-beta(1-42) alters structure and function of retinal pigmented epithelial cells. *Aging Cell* 8, 162-177
233. Müller, C., Charniga, C., Temple, S., and Finnemann, S. C. (2018) Quantified F-Actin Morphology Is Predictive of Phagocytic Capacity of Stem Cell-Derived Retinal Pigment Epithelium. *Stem Cell Reports* 10, 1075-1087
234. Chen, M., Rajapakse, D., Fraczek, M., Luo, C., Forrester, J. V., and Xu, H. (2016) Retinal pigment epithelial cell multinucleation in the aging eye - a mechanism to repair damage and maintain homoeostasis. *Aging Cell* 15, 436-445
235. Tarau, I. S., Berlin, A., Curcio, C. A., and Ach, T. (2019) The Cytoskeleton of the Retinal Pigment Epithelium: from Normal Aging to Age-Related Macular Degeneration. *Int J Mol Sci* 20
236. Shu, D. Y., Butcher, E., and Saint-Geniez, M. (2020) EMT and EndMT: Emerging Roles in Age-Related Macular Degeneration. *Int J Mol Sci* 21
237. Zhou, M., Geathers, J. S., Grillo, S. L., Weber, S. R., Wang, W., Zhao, Y., and Sundstrom, J. M. (2020) Role of Epithelial-Mesenchymal Transition in Retinal Pigment Epithelium Dysfunction. *Front Cell Dev Biol* 8, 501
238. Kaarniranta, K., Uusitalo, H., Blasiak, J., Felszeghy, S., Kannan, R., Kauppinen, A., Salminen, A., Sinha, D., and Ferrington, D. (2020) Mechanisms of mitochondrial dysfunction and their impact on age-related macular degeneration. *Prog Retin Eye Res* 79, 100858
239. Radeke, M. J., Radeke, C. M., Shih, Y. H., Hu, J., Bok, D., Johnson, L. V., and Coffey, P. J. (2015) Restoration of mesenchymal retinal pigmented epithelial cells by TGFβ pathway inhibitors: implications for age-related macular degeneration. *Genome Med* 7, 58
240. Santos, F., Moreira, C., Nóbrega-Pereira, S., and Bernardes de Jesus, B. (2019) New Insights into the Role of Epithelial-Mesenchymal Transition during Aging. *Int J Mol Sci* 20
241. Papageorgis, P. (2017) Complex Interplay Between Aging and Cancer: Role of TGF-β Signaling. *Crit Rev Oncog* 22, 313-321
242. Tominaga, K., and Suzuki, H. I. (2019) TGF-β Signaling in Cellular Senescence and Aging-Related Pathology. *Int J Mol Sci* 20
243. Kliffen, M., Sharma, H. S., Mooy, C. M., Kerkvliet, S., and de Jong, P. T. (1997) Increased expression of angiogenic growth factors in age-related maculopathy. *Br J Ophthalmol* 81, 154-162
244. Bai, Y., Liang, S., Yu, W., Zhao, M., Huang, L., Zhao, M., and Li, X. (2014) Semaphorin 3A blocks the formation of pathologic choroidal neovascularization induced by transforming growth factor beta. *Mol Vis* 20, 1258-1270
245. Tosi, G. M., Caldi, E., Neri, G., Nuti, E., Marigliani, D., Baiocchi, S., Traversi, C., Cevenini, G., Tarantello, A., Fusco, F., Nardi, F., Orlandini, M., and Galvagni, F. (2017) HTRA1 and TGF-β1 Concentrations in the Aqueous Humor of Patients With Neovascular Age-Related Macular Degeneration. *Invest Ophthalmol Vis Sci* 58, 162-167
246. Ohlmann, A., Scholz, M., Koch, M., and Tamm, E. R. (2016) Epithelial-mesenchymal transition of the retinal pigment epithelium causes choriocapillaris atrophy. *Histochem Cell Biol* 146, 769-780
247. Choi, K., Lee, K., Ryu, S. W., Im, M., Kook, K. H., and Choi, C. (2012) Pirfenidone inhibits transforming growth factor-β1-induced fibrogenesis by blocking nuclear translocation of Smads in human retinal pigment epithelial cell line ARPE-19. *Mol Vis* 18, 1010-1020
248. Kimura, K., Orita, T., Liu, Y., Yang, Y., Tokuda, K., Kurakazu, T., Noda, T., Yanai, R., Morishige, N., Takeda, A., Ishibashi, T., and Sonoda, K. H. (2015) Attenuation of EMT in RPE cells and subretinal fibrosis by an RAR-γ agonist. *J Mol Med*

(Berl) 93, 749-758
249. Matoba, R., Morizane, Y., Shiode, Y., Hirano, M., Doi, S., Toshima, S., Araki, R., Hosogi, M., Yonezawa, T., and Shiraga, F. (2017) Suppressive effect of AMP-activated protein kinase on the epithelial-mesenchymal transition in retinal pigment epithelial cells. *PLoS One* 12, e0181481
250. Yang, J., Li, J., Wang, Q., Xing, Y., Tan, Z., and Kang, Q. (2018) Novel NADPH oxidase inhibitor VAS2870 suppresses TGF-β-dependent epithelial-to-mesenchymal transition in retinal pigment epithelial cells. *Int J Mol Med* 42, 123-130
251. Wu, D., Kanda, A., Liu, Y., Kase, S., Noda, K., and Ishida, S. (2019) Galectin-1 promotes choroidal neovascularization and subretinal fibrosis mediated via epithelial-mesenchymal transition. *Faseb j* 33, 2498-2513
252. Antikainen, H., Driscoll, M., Haspel, G., and Dobrowolski, R. (2017) TOR-mediated regulation of metabolism in aging. *Aging Cell* 16, 1219-1233
253. Teixeira, G., Szyndralewiez, C., Molango, S., Carnesecchi, S., Heitz, F., Wiesel, P., and Wood, J. M. (2017) Therapeutic potential of NADPH oxidase 1/4 inhibitors. *Br J Pharmacol* 174, 1647-1669
254. Bonilha, V. L. (2008) Age and disease-related structural changes in the retinal pigment epithelium. *Clin Ophthalmol* 2, 413-424
255. Hyttinen, J. M. T., Kannan, R., Felszeghy, S., Niittykoski, M., Salminen, A., and Kaarniranta, K. (2019) The Regulation of NFE2L2 (NRF2) Signalling and Epithelial-to-Mesenchymal Transition in Age-Related Macular Degeneration Pathology. *Int J Mol Sci* 20
256. Handa, J. T. (2012) How does the macula protect itself from oxidative stress? *Mol Aspects Med* 33, 418-435
257. Kim, S. J., Kim, Y. S., Kim, J. H., Jang, H. Y., Ly, D. D., Das, R., and Park, K. S. (2020) Activation of ERK1/2-mTORC1-NOX4 mediates TGF-β1-induced epithelial-mesenchymal transition and fibrosis in retinal pigment epithelial cells. *Biochem Biophys Res Commun* 529, 747-752
258. Yu, B., Xu, P., Zhao, Z., Cai, J., Sternberg, P., and Chen, Y. (2014) Subcellular distribution and activity of mechanistic target of rapamycin in aged retinal pigment epithelium. *Invest Ophthalmol Vis Sci* 55, 8638-8650
259. Ghosh, S., Shang, P., Terasaki, H., Stepicheva, N., Hose, S., Yazdankhah, M., Weiss, J., Sakamoto, T., Bhutto, I. A., Xia, S., Zigler, J. S., Jr., Kannan, R., Qian, J., Handa, J. T., and Sinha, D. (2018) A Role for βA3/A1-Crystallin in Type 2 EMT of RPE Cells Occurring in Dry Age-Related Macular Degeneration. *Invest Ophthalmol Vis Sci* 59, Amd104-amd113
260. Chen, K. H., Hsu, H. H., Lee, C. C., Yen, T. H., Ko, Y. C., Yang, C. W., and Hung, C. C. (2014) The AMPK agonist AICAR inhibits TGF-β1 induced activation of kidney myofibroblasts. *PLoS One* 9, e106554
261. Stone, J. D., Holt, A. W., Vuncannon, J. R., Brault, J. J., and Tulis, D. A. (2015) AMP-activated protein kinase inhibits transforming growth factor-β-mediated vascular smooth muscle cell growth: implications for a Smad-3-dependent mechanism. *Am J Physiol Heart Circ Physiol* 309, H1251-1259
262. Li, N. S., Zou, J. R., Lin, H., Ke, R., He, X. L., Xiao, L., Huang, D., Luo, L., Lv, N., and Luo, Z. (2016) LKB1/AMPK inhibits TGF-β1 production and the TGF-β signaling pathway in breast cancer cells. *Tumour Biol* 37, 8249-8258
263. El Annan, J., Chauhan, S. K., Ecoiffier, T., Zhang, Q., Saban, D. R., and Dana, R. (2009) Characterization of effector T cells in dry eye disease. *Invest Ophthalmol Vis Sci* 50, 3802-3807
264. Stevenson, W., Chauhan, S. K., and Dana, R. (2012) Dry eye disease: an immune-mediated ocular surface disorder. *Arch Ophthalmol* 130, 90-100
265. Sabatino, F., Di Zazzo, A., De Simone, L., and Bonini, S. (2017) The Intriguing Role of Neuropeptides at the Ocular Surface. *Ocul Surf* 15, 2-14
266. Liu, L., Dana, R., and Yin, J. (2020) Sensory neurons directly promote angiogenesis in response to inflammation via substance P signaling. *Faseb j* 34,

6229-6243
267. Yu, M., Lee, S. M., Lee, H., Amouzegar, A., Nakao, T., Chen, Y., and Dana, R. (2020) Neurokinin-1 Receptor Antagonism Ameliorates Dry Eye Disease by Inhibiting Antigen-Presenting Cell Maturation and T Helper 17 Cell Activation. *Am J Pathol* **190**, 125-133
268. Ellenberg, D., Azar, D. T., Hallak, J. A., Tobaigy, F., Han, K. Y., Jain, S., Zhou, Z., and Chang, J. H. (2010) Novel aspects of corneal angiogenic and lymphangiogenic privilege. *Prog Retin Eye Res* **29**, 208-248
269. Chen, Y., Chauhan, S. K., Lee, H. S., Stevenson, W., Schaumburg, C. S., Sadrai, Z., Saban, D. R., Kodati, S., Stern, M. E., and Dana, R. (2013) Effect of desiccating environmental stress versus systemic muscarinic AChR blockade on dry eye immunopathogenesis. *Invest Ophthalmol Vis Sci* **54**, 2457-2464
270. Albuquerque, R. J., Hayashi, T., Cho, W. G., Kleinman, M. E., Dridi, S., Takeda, A., Baffi, J. Z., Yamada, K., Kaneko, H., Green, M. G., Chappell, J., Wilting, J., Weich, H. A., Yamagami, S., Amano, S., Mizuki, N., Alexander, J. S., Peterson, M. L., Brekken, R. A., Hirashima, M., Capoor, S., Usui, T., Ambati, B. K., and Ambati, J. (2009) Alternatively spliced vascular endothelial growth factor receptor-2 is an essential endogenous inhibitor of lymphatic vessel growth. *Nat Med* **15**, 1023-1030
271. Yücel, Y. H., Johnston, M. G., Ly, T., Patel, M., Drake, B., Gümüş, E., Fraenkl, S. A., Moore, S., Tobbia, D., Armstrong, D., Horvath, E., and Gupta, N. (2009) Identification of lymphatics in the ciliary body of the human eye: a novel "uveolymphatic" outflow pathway. *Exp Eye Res* **89**, 810-819
272. Heindl, L. M., Hofmann-Rummelt, C., Adler, W., Holbach, L. M., Naumann, G. O., Kruse, F. E., and Cursiefen, C. (2010) Tumor-associated lymphangiogenesis in the development of conjunctival squamous cell carcinoma. *Ophthalmology* **117**, 649-658
273. Wuest, T. R., and Carr, D. J. (2010) VEGF-A expression by HSV-1-infected cells drives corneal lymphangiogenesis. *J Exp Med* **207**, 101-115
274. Mantyh, P. W. (2002) Neurobiology of substance P and the NK1 receptor. *J Clin Psychiatry* **63 Suppl 11**, 6-10
275. Steinhoff, M. S., von Mentzer, B., Geppetti, P., Pothoulakis, C., and Bunnett, N. W. (2014) Tachykinins and their receptors: contributions to physiological control and the mechanisms of disease. *Physiol Rev* **94**, 265-301
276. Mashaghi, A., Marmalidou, A., Tehrani, M., Grace, P. M., Pothoulakis, C., and Dana, R. (2016) Neuropeptide substance P and the immune response. *Cell Mol Life Sci* **73**, 4249-4264
277. Di Zazzo, A., Coassin, M., Varacalli, G., Galvagno, E., De Vincentis, A., and Bonini, S. (2019) Neurotrophic keratopathy: Pros and cons of current treatments. *Ocul Surf* **17**, 619-623
278. Taketani, Y., Marmalidou, A., Dohlman, T. H., Singh, R. B., Amouzegar, A., Chauhan, S. K., Chen, Y., and Dana, R. (2020) Restoration of Regulatory T-Cell Function in Dry Eye Disease by Antagonizing Substance P/Neurokinin-1 Receptor. *Am J Pathol* **190**, 1859-1866
279. Tammela, T., and Alitalo, K. (2010) Lymphangiogenesis: Molecular mechanisms and future promise. *Cell* **140**, 460-476
280. Mohammadi, F., Javid, H., Afshari, A. R., Mashkani, B., and Hashemy, S. I. (2020) Substance P accelerates the progression of human esophageal squamous cell carcinoma via MMP-2, MMP-9, VEGF-A, and VEGFR1 overexpression. *Molecular Biology Reports* **47**, 4263-4272

국문 초록

서론: 혈관의 비정상적인 성장을 보이는 신생혈관은 시력을 위협하는 안구 질환의 주요 특징으로 미숙아망막병증, 당뇨병성 망막병증, 신생혈관성 나이관련 황반변성 및 각막 신생혈관 관련 질환이 포함된다. 혈관내피세포성장인자가 안구 혈관신생을 유발하는 주요 혈관신생 촉진 인자이고 항혈관내피세포성장인자 치료가 안구 신생혈관에 대한 표준 치료법이지만, 이의 적용은 안구와 전신적 부작용으로 인해 여전히 한계점이 있다. 본 연구에서는 대표적인 시력을 위협하는 안질환 생쥐모델의 질환 표현형에 대해 안구내 약물 전달을 통한 치료 효과를 연구하고자 하였다.

방법: 1) 마우스 혈소판유래성장인자 수용체 베타를 표적으로 하는 항체-약물접합체를 이용하여, 생체 외 실험으로 마우스뇌혈관주위세포의 유세포분석, 세포독성실험, 공초점현미경실험을 시행하고, 산소 유도 망막병증 및 레이저 유도 맥락막 신생혈관 마우스 모델을 이용하여 항체-약물 복합체의 내재화 및 세포독성효과, 그리고 망막 및 맥락막 신생혈관의 억제 효과를 평가하였다. 2) 면역세포화학법, 실시간 중합효소연쇄반응, 웨스턴 블롯 분석, 유세포분석, 상피간투과성시험, 상피전기저항측정, 효소결합면역흡착검사를 통해 공동배양조건에서 대식세포 분극화 조절에 따른 망막색소상피세포의 구조적 및 기능적 안전성에 대한 추가적 영향을 미치는지 연구하였다. 면역형광염색, 형광표지된 덱스트란 혈관투과검사 및 실시간 중합효소연쇄반응검사를 통해 스트렙토조토신 유도 당뇨 마우스 모델에서 M2 대식세포 분극화가 외측 혈액망막장벽 손상 및 혈관 누출을 억제할 수 있는지를 평가하였다. 3) 면역세포화학법, 면역화학염색, 웨스턴 블롯 분석, 활성산소 측정 실험을 통해 망막색소상피세포와 유리체강내 형질전환 성장인자 베타1 처리 마우스 모델에서 AICAR와 GKT137831의 형질전환 성장인자 베타1에 의해 유도된 망막색소상피세포의 형태학적 변화 및 상피-중간엽전이에 대한 예방 효과를 평가하였다. 4) 면역세포화학법, 혈관신생분석 및 웨스턴 블롯 분석을 통해 인간 피부 림프관내피세포의 림프관신생과 substance P/neurokinin-1 수용체 시스템과의 관련성을 평가하였다. 면역

조직화학법, 각막 혈광염색, 페놀 레드 검사 및 실시간 중합효소연쇄반응을 통해 각막 림프관 신생에서의 Substance P 신호 전달 차단의 효과를 평가했다.

결과: 1) 마우스 혈소판유래성장인자 수용체 베타를 표적으로 하는 항체-약물접합체는 마우스뇌혈관주위세포에 효과적으로 내재화 되어 세포독성을 나타냈다. 항체-약물접합체 사용을 통한 혈소판유래성장인자 수용체 베타를 과다발현하는 혈관주위세포의 특이적 제거는 산소 유도 망막병증 및 레이저 유도 맥락막 신생혈관 마우스 모델에서의 병적 망막 및 맥락막 신생혈관을 유의하게 억제하였다. 2) 대식세포 분극화의 변화는 고혈당 조건에서의 망막색소상피세포의 구조적 및 기능적 안정성에 추가적으로 영향을 주었다. 유리체강내 인터루킨-10 주사는 M2 미세아교세포/대식세포 분극을 유도하였고, 초기 스트렙토조토신 유도 당뇨 마우스 모델에서의 외측 혈액망막장벽 손상 및 혈관 누출을 억제하였다. 3) AICAR 또는 GKT137831 처리에 따른 mTORC1 또는 NOX4 신호 전달 경로의 억제는 생체 외 및 생체 내 망막색소상피세포의 상피-중간엽전이를 약화시키고 구조적 안정성을 개선시켰다. 4) Neurokinin-1 수용체 길항제인 L733,060 또는 neurokinin-1 수용체 표적 siRNA를 사용한 substance P 신호전달의 차단은 인간 피부 림프관내피세포에서의 substance P에 의해 자극된 림프신생혈관 및 혈관내피성장인자 수용체 3의 발현을 억제하였다. Neurokinin-1 수용체 길항제는 또한 생체 내 실험에서 각막의 림프신생혈관을 억제하고 안구건조증의 임상 양상을 완화시켰다. Neurokinin-1 수용체 길항제는 안구건조증의 각막 및 결막 조직에서의 혈관내피성장인자-C, 혈관내피성장인자-D, 및 혈관내피성장인자 수용체 3을 포함한 림프혈관신생 인자들을 효과적으로 억제하였다.

결론: 항체-약물접합체, 저분자화합물, 단백질과 같은 치료 양식의 안구내 주사는 효과적으로 망막, 맥락막 및 각막에서의 병적인 신생혈관 및 혈관이상을 효과적으로 억제하였다. 이러한 약물들의 잠재적인 안구 독성을 최소화하기 위한 면밀한 독성 연구와 교란 요인들을 배제하기 위한 추가 연구를 통해 시력을 위협하는 안질환에 대한 치료제의 적용을 촉진시킬 수 있을 것으로 기대한다.

* 본 학위논문의 일부는 Communications medicine 학술지 (1), FASEB J 학술지 (2), Ocular surface 학술지 (3)에 출판된 내용에 기반하여 작성됨.

주요어: 맥락막 신생혈관, 각막 신생혈관, 망막 신생혈관, 상피-중간엽 전이, 안구내 주사, 외측 혈액망막장벽

학번: 2018-38536